2.15 The Physical Analyses of Muddy Sedimentation Processes

JC Winterwerp, Deltares & Delft University of Technology, Delft, The Netherlands

Abstract

This chapter summarizes sedimentation processes in estuaries and coastal areas. We focus on fine, cohesive sediments and processes in the vertical and follow a hypothetical tidal cycle. These fines can form flocs, induced by turbulent mixing and stresses, which may settle as individual particles, or may be subject to hindered settling when concentrations increase. When a network (gel) is formed, the water–sediment mixture is referred to as fluid mud. In general, fluid mud is in a transient state, consolidating in quiet water. The bed formed from deposition and/or consolidation can be eroded by flow-induced stresses, which have a stochastic nature when the flow is turbulent.

2.15.1 Introduction

This chapter focuses on the physical aspects of sedimentation processes for fine sediments in estuaries and coastal areas, with emphasis on cohesive sediments. Although the treatment is largely physical, it is recognized that biology has an important role to play in many aspects of fine-sediment behavior. For example, flocculation is modified by the presence of sticky organic material, which is often referred to as extracellular polymer substances (EPSs – mainly polysaccharides), although some other substances are important as well. These substances are secreted by microphytobenthos (algae) and bacteria. Currently, biological effects can only be taken into account from a predictive, modeling viewpoint by modifying the various parameters that arise in the physical descriptions presented here. The reader is referred to, for example, Le Hir et al. (2007) for an overview. The first part of this chapter presents a classification of fine sediments and summarizes relevant processes in the water column and sediment bed, whereas the last part discusses the formation and behavior of fluid mud.

Estuarine and coastal systems are very shallow in general: horizontal scales (length and width) exceed the water depth by many orders of magnitude, as shown in Figure 1. The sedimentary features in such systems are therefore largely governed by exchange processes at the water–bed interface. Yet, in spite of this shallowness, these exchange processes are often significantly affected by three-dimensional structures in the water column and within the sediment bed. This chapter, therefore, focuses on the processes at the water–bed interface, said three-dimensional structures, and their effect on sedimentation processes, with emphasis on the fine, cohesive fraction of the sediments.

It should further be acknowledged that sediments in estuarine and coastal systems generally consist of mixtures of clays, silts, sand, organic material (alive or dead), often a lot of (pore) water, and sometimes gas (methane and carbon dioxide). The composition of these mixtures may vary in space and time (seasonal effects!), and biology may affect the properties of these mixtures greatly – the latter being treated extensively in Chapter 2.14.

This chapter is further confined by its focus on the shorter timescales (i.e., a spring–neap cycle at most). We treat sedimentation processes as a function of local (hydrodynamic) forcing, the history of that forcing and the accompanied deformations, and the availability of sediments. The important feedback between sedimentation processes and bed geometry, the discipline of geomorphology, is treated in Volume 3, whereas the underlying net transport rates, for instance, as a function of tidal asymmetry, gravitation circulation, etc., are treated in Chapter 2.17.

The sedimentation processes discussed in this chapter cannot be understood properly without a thorough understanding of the driving hydrodynamics in the estuary and/or coastal system. In particular, we refer frequently to the dynamics and properties of (tidal) flow; waves; current–wave interaction; stratification and density currents induced by temperature, salinity, and/or suspended sediment; turbulence and mixing; and the structure of the (turbulent) boundary layer. These dynamics are discussed elsewhere in this treatise (See Section 2.15.4, 2.15.5 and 2.15.7). However, hydrodynamic properties may alter when the suspension evolves from a dilute water–sediment mixture, via a high-concentrated water–sediment mixture, to a soil. A description of these changes requires some background on the so-called non-Newtonian behavior and soil mechanical theory – these are provided within this chapter, when relevant.

In our treatise on sedimentation processes, we follow a hypothetical tidal cycle, possibly modulated by episodic events, describing sediment behavior in the water column,

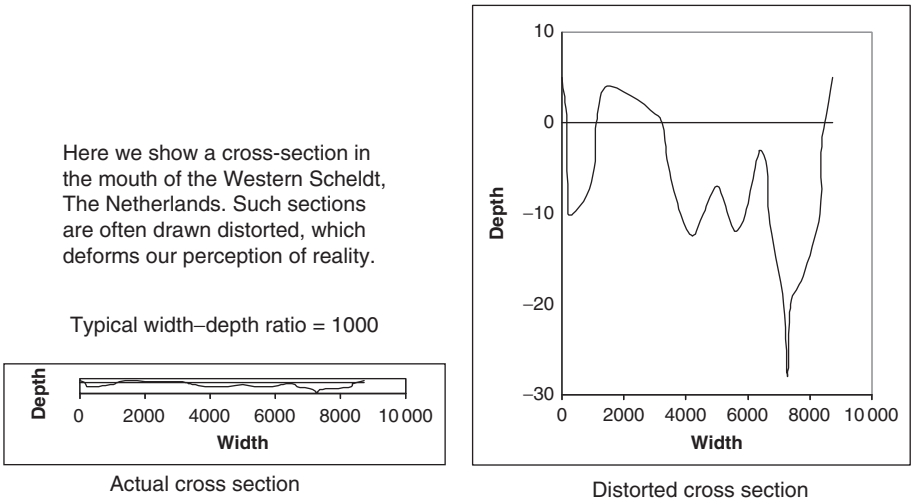

Figure 1 Diagram of typical estuarine cross section, drawn in distorted and actual form.

within the bed, and at the water–bed interface. As this chapter focuses on sedimentation processes, we start our cycle in the water column, though we appreciate that most sediment is found in the sediment bed.

In Figure 2 and Table 1, we summarize the various definitions on sediment concentration used in this chapter. We distinguish between mass and volume concentration, mass and volume fractions, and use a number of soil mechanical parameters, such as water content. Furthermore, we use the following superscripts to distinguish between the various mineral constituents: cl, clay; si, silt; sa, sand; and m, mud, in which the mineral content of mud consists of a mixture of clay and silt. Note that more generally, mud is defined as a mixture of minerals (clays and silt, some fine sand), organic matter (alive or dead), a lot of water, and sometimes gas. In addition, we use the following subscripts: s, solids; w, water; f, floc; p, primary particle; 0, neutral conditions; ref, reference conditions; and e, equilibrium conditions.

In this chapter, we discuss formulations for gross effects: deposition D denotes gross flux of sediment onto the bed from the overlying suspension and erosion E the gross flux of sediment from the bed into the overlying suspension

The net effect, that is, $D - E$, is referred to as:

- bed level changes (neutral);
- sedimentation, siltation, accretion, aggradation ($D > E$); and
- scour, degradation ($E > D$).

Some of these definitions are fairly arbitrary; other authors use other definitions. However, when consistently used, this should not be a problem. In this chapter, we present formulas

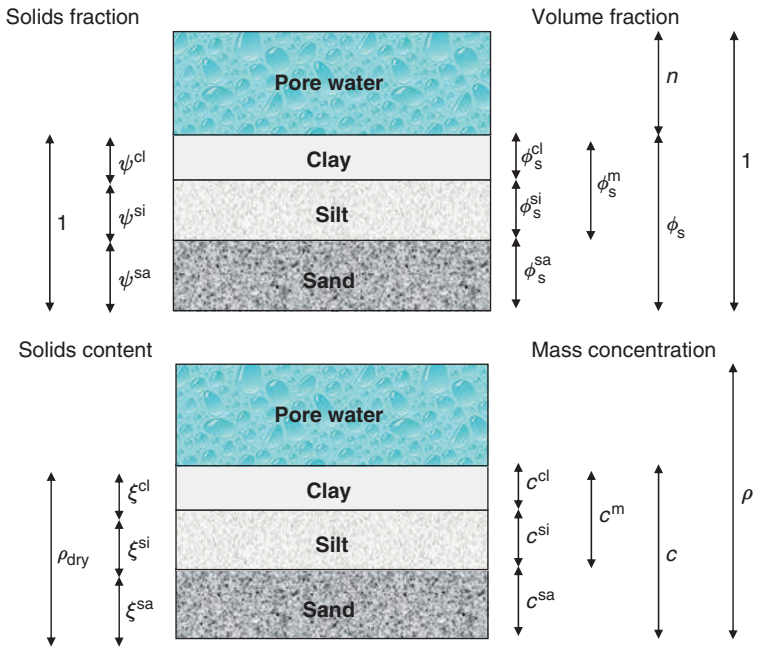

Figure 2 Various definitions used in this chapter (Winterwerp and Van Kesteren, 2004).

Table 1 Some definitions used in this chapter

c	Mass concentration	Mass of solids/total wet volume
e	Void ratio	Volume of pores/volume of solids
n	Porosity	Volume of pores/total wet volume
ϕ_f	Volume concentration of flocs	Volume flocs/total wet volume
ϕ_s	Volume concentration of solids	Volume solids/total wet volume
ρ	Bulk density	Mass wet sediment/total wet volume
ρ_{dry}	Dry bed density	$\equiv$ c = Mass of solids/total wet volume
ρ_s	Specific density solids	Mass of solids/volume of solids
ρ_w	Specific water density	Mass of water/volume of water
ξ^i	Solids content	Mass solid i/total mass solids
ψ^i	Solids fraction	Volume solid i/total solids volume
W	Water content	Mass of water/total mass of solids

for both E and D as positive parameters. This implies that positive/negative signs have to be added in the balance equations where E and D are used.

We use a similar approach for floc forming:

- aggregation = growth of floc size as a result of coalescence of flocs,
- breakup = decrease in floc size as a result of breaking of flocs into smaller entities,
- flocculation = net effect of the simultaneous processes of aggregation and breakup, and
- coagulation = irreversible formation of primary particles.

We define coagulation as the process of formation of primary particles, that is, the building stones of the cohesive sediment flocs. For the ambient conditions at hand, this is an irreversible process: the stresses occurring in the water column (and near the bed!) are too small for breaking up these primary particles. Note that these primary particles may contain many (hundreds) clay particles and organic material, and their specific density may be smaller than the sediment's specific density. Deflocculation in the laboratory by treatment with hydroperoxide and/or ultrasonic stirring can break up these primary particles.

Flocculation, aggregation, and breakup are reversible processes within this concept, reversible given the stresses occurring in the environment.

We start this chapter with a brief, general classification of transport modes, as can be found in most textbooks on sediment transport. Then we discuss the settling of sediment particles in general, and of cohesive sediment flocs in particular, treating flocs as self-similar entities. In that section, also the sedimentation flux is assessed, both in case of monodisperse particles and in case of a distribution in floc size. These results are applicable to single particles settling in still water. When the sediment concentration increases, hindered settling, and, ultimately, consolidation start to play a role. In Section 2.15.4, we discuss the process of hindered settling, using Kynch's characteristics approach. We also re-derive Gibson's consolidation equation in the convenient form of an advection–diffusion equation, again assuming self-similarity of the floc (e.g., bed) structure. Next, in Section 2.15.5, we relate mechanical bed properties to soil mechanical bulk parameters, which are easily measured. Here, we derive a sediment stability diagram, which allows prediction of the behavior of the bed (i.e., either as granular or as cohesive material), based on the soil's sand content and its bulk density. This scheme is used in Section 2.15.6 to derive an erosion formula, accounting for the stochastic nature of the eroding agent (i.e., turbulent flow), distinguishing between floc and surface erosion.

Finally, in Section 2.15.7, we discuss the formation and behavior of fluid mud. We argue that the properties of fluid mud are poorly defined, because these are governed by the history of the sediment–water mixture. In this section, we show how sediment-induced buoyancy effects affect the transport capacity of sediment-laden flow, and how waves are damped over fluid mud layers through viscous dissipation.

Because of limitations in the space available for this chapter, we have refrained from extensive literature discussions – the reference list is therefore a bit biased toward work of the author of this chapter. However, such discussions are found in, for example, Winterwerp and Van Kesteren (2004). A recent literature summary on the occurrences and behavior of fluid mud can be found in McAnally et al. (2007a, 2007b).

2.15.2 Classification of Transport Modes

This section discusses the various modes of sediment transport in estuaries and coastal areas, as introduced in all classical textbooks on sediment transport. We should realize that these modes may change along a river system, or within a coastal area. For instance, fine cohesive sediments will be classified as wash load in most parts of the upper river. Further downstream, these fines may become part of the riverbed, whereas in the estuarine region, these fines may form mobile fluid mud layers, characterized by a form of bed load transport (**Figure 3**).

In this chapter, we focus on estuaries and coastal regions, where tidal effects are dominant, and also the effects of salinity intrusion, wind-driven flow, and waves in particular may be important. Moreover, we deal with fine sediments, often of a cohesive nature. In this section, we discuss when such fine sediments have cohesive behavior.

In general, we can distinguish a number of net sources of (fine) sediment in our region of interest:

1. Fine sediments are carried by the river – these may originate from terrestic erosion in the river's catchment area, and/or erosion of the riverbed and/or riverbank (meandering/breaching).
2. Fine sediments may be supplied from marine origin – the source of these marine sediments may be formed by erosion of coastal areas well away from our area of interest (as in East

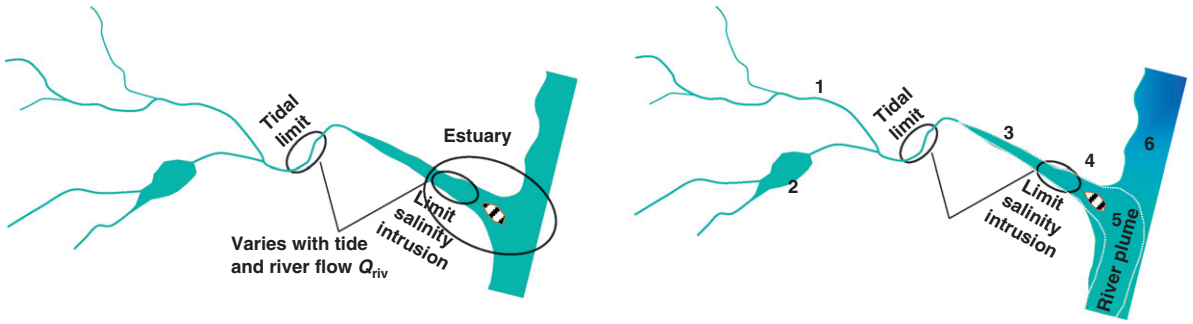

Figure 3 Some relevant features along a river flowing into a coastal sea. For definition of 1–6 see **Table 2**.

Table 2 Characteristic processes along a river flowing into a sea

1. River	Hydrograph
2. Lake/reservoir	Wind, waves, temp. stratification
3. Tidal river	Tide, hydrograph, flow direction
4. Estuary	Tide, river flow, salinity stratification
5. ROFI	Tide, wind, Coriolis, S&T stratification, waves
6. Coastal area	Waves, tide, wind

ROFI, region of freshwater influence.

Anglia, UK, from erosion of the northerly Holderness cliffs) or from erosion of the seabed. Note that the mobilized sediments may have riverine origin as well; the deposits may have been formed in earlier geological eras, for instance.

3. Fine sediments may also be re-mobilized from within the area of interest (autochthonous sediments) from earlier deposits – these may concern sediment deposits from, for example, glacier times, but may as well be much more recent, deposited in preceding years, various seasons, etc.

Assessment of sources and sinks of fine sediments is one of the major challenges of scientists and engineers studying particular sites. General rules do not exist, as sources and sinks are very site specific, and have therefore to be determined for each site (**Figure 4**).

We note that cohesive sediment consists of mixtures of clay, silt, some fine sands, organic material (dead or alive), a lot of water, and sometimes (within the bed) gas. The composition of these mixtures may change in space and time (seasonal effects!).

Figure 5 shows a classification of sediment in the form of grain size. Note that different classifications are used at various places in the world. Mud or cohesive sediment is characterized by grain size <63 μm (in most countries). Beds with mixtures of sediment depict cohesive properties when the clay content exceeds 5–10%, depending on the clay minerals and organic material in the mixture (Winterwerp and Van Kesteren, 2004). As silt and clay particles occur at an almost constant ratio at a specific estuarine or coastal site, sediment mixtures with a mud content of around 30–40% exhibit cohesive properties. For more background information, the reader is referred to Winterwerp and Van Kesteren (2004) – we elaborate a bit more on these mixtures in Section 2.15.6.

Note that, next to differences in definitions, considerable differences in particle-size distribution are found using different measuring techniques. The particle-size distributions (of deflocculated material) in **Figure 6** have been measured at a few laboratories in the Netherlands (following standardized procedures) with a Coulter counter and with a sedigraph. Even the distributions measured with Coulter counter, but at different laboratories, differ considerably.

This is one reason to use the sand content in defining the composition of sediment mixtures, as explained elsewhere in this chapter. **Figure 7** sketches the various modes of sediment transport in the water column.

We distinguish between sediments found in the bed and those which are not found in the bed – the latter is referred to as

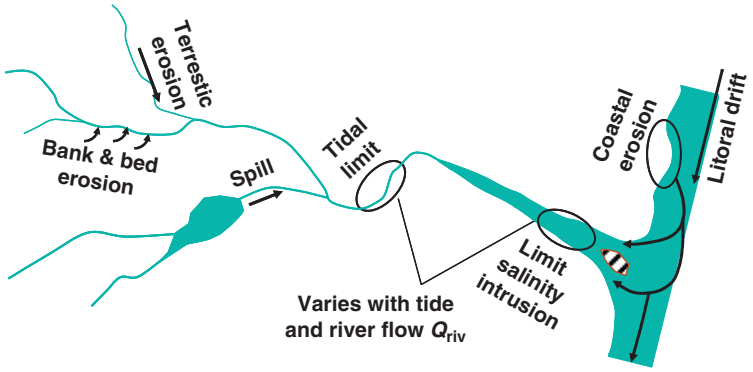

Figure 4 Sources of fine sediments in riverine system.

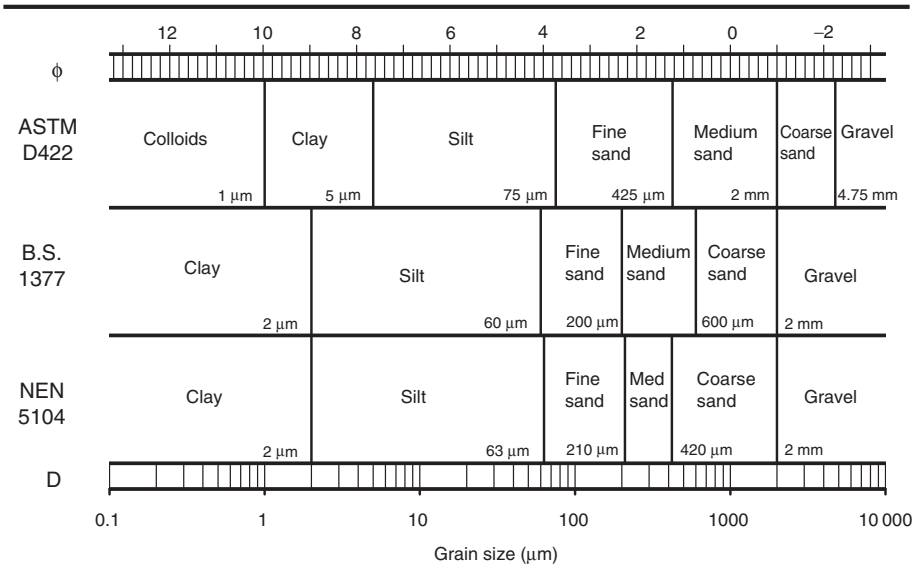

Figure 5 Sediment classification based on grain size according to various standards; $\phi = -^{2}\log D$ (D in mm).

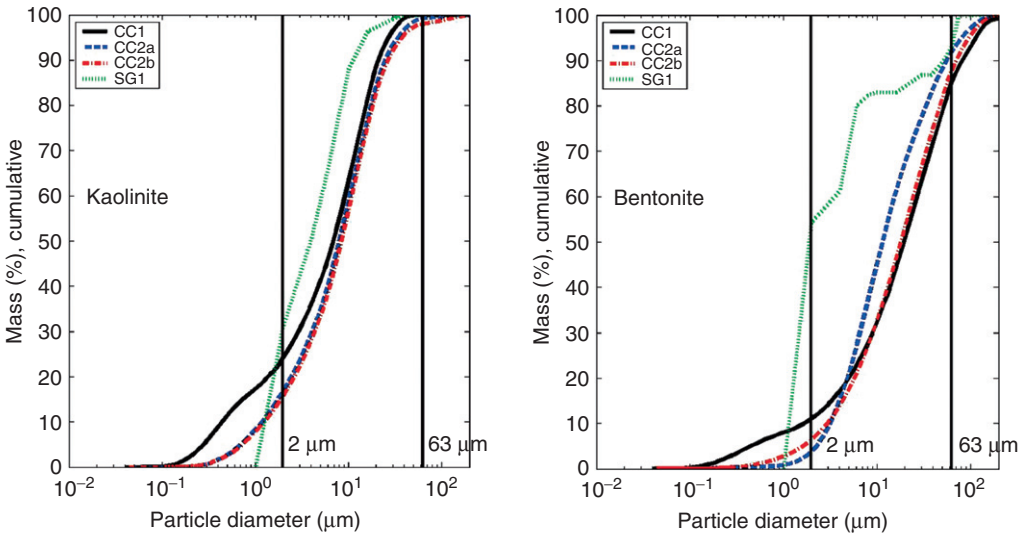

Figure 6 Grain size distributions of dry samples of kaolinite and bentonite at various laboratories, using the same instrument (Coulter counter), and different instruments (Coulter counter and sedigraph). CC, Coulter counter; SG, sedigraph. (After Jacobs, 2011)

wash load. Bed material, sediments encountered within the bed locally, may be transported in the form of bed load and suspended load, and often both transport modes occur.

Bed load transport is confined to a thin layer near the bed, a few grain diameters in thickness (Einstein, 1950; Van Rijn, 1993). Within this thin layer, particles make small jumps, known as saltations, induced by the hydrodynamic forces on the particles. Bed load is the transport mode generating bedforms, such as ripples and dunes. At larger flow velocities, the majority of the sediment is transported in the form of suspended load.

In this chapter, we are mainly concerned with the suspended transport mode. Sediment particles are kept in suspension by turbulent mixing – turbulence is therefore a prerequisite for suspended load – against the effects of gravity, that is, settling. This balance yields vertical gradients in suspended sediment concentration, which increase with the size and effective density of the particles: very fine particles (wash load) are characterized by an almost uniform distribution over the water depth. In the horizontal direction, particles are carried by the main water flow, though sediment-induced density currents may occur as well. We will elaborate on the settling and mixing of fine sediments as well as sediment-induced density currents in the next sections of this chapter.

In suspensions of fine, cohesive sediment, bed load is virtually absent. Only in the case of fluid mud, near-bed sediment transport may occur, but not in the form of saltations. In addition,

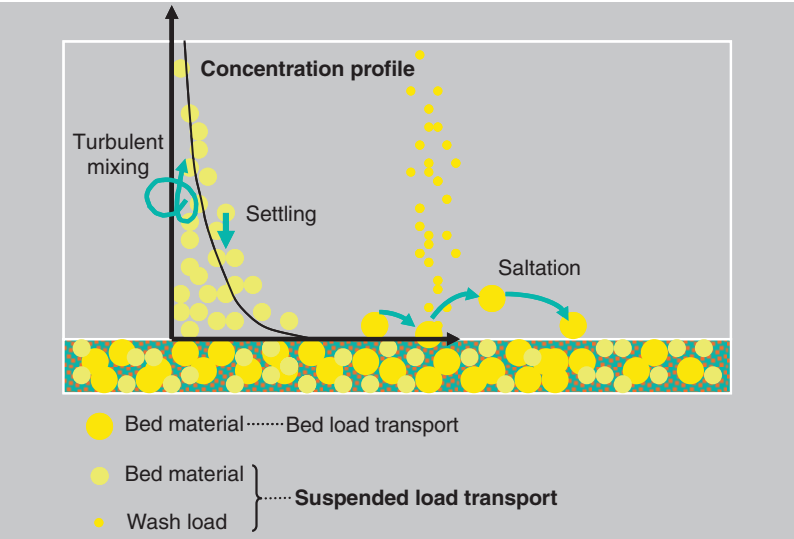

Figure 7 Classical picture on sediment transport, distinguishing between wash load, bed material load; suspended load transport and bed load transport. Note that the same sediment may behave differently (fall in other classes) in different parts of the river (e.g., **Figure 3**).

when cohesives are clustered in large entities (mud balls), originating from mass erosion, a kind of bed load may occur.

The onset of motion of granular sediments is governed by the size of the grains. Shields presented a diagram, depicting initiation of motion on sedimentary beds composed of sand (granular skeleton – e.g., Section 2.15.5). His diagram was based on numerous flume experiments. Later, his work was extended – here we present the work of Van Rijn (1993), for example, **Figure 8**, showing a gradual transition from a stable bed to massive sediment movements.

In **Figure 9** we present the combined effect of currents and waves. The residual bed shear stress by currents and waves $\tau_{c,w}$ is obtained from a linear superposition of the magnitudes of the bed shear stresses induced by currents (τ_c) and by waves (τ_w), that is, $\tau_{c,w} = \tau_c + \tau_w$. Note that in other studies vector addition of stresses or near-bed velocities is advocated.

2.15.3 Settling and Deposition from Suspension

This section focuses on the settling velocity of single particles in still water. Particles of inert sediments, for example, sand, follow Stokes' law, with some modifications when the particle Reynolds number exceeds unity. However, cohesive sediment forms flocs. These flocs have settling velocities exceeding those of their components (clay, silt particles, organic matter, etc.) by orders of

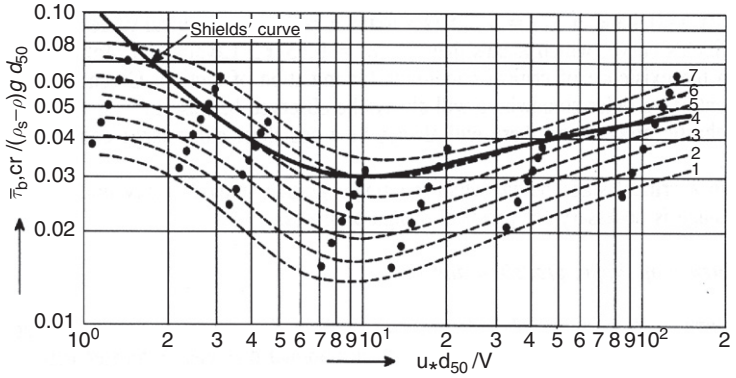

- Measured

1 Occasional particle movement at some locations
2 Frequent particle movement at some locations
3 Frequent particle movement at many locations
4 Frequent particle movement at nearly all locations
5 Frequent particle movement at all locations
6 Permanent particle movement at all locations
7 General transport (initiation of ripples)

$$D_* = \left(\frac{(\rho_s/\rho - 1)g}{\nu^2} \right)^{1/3} D_{50}$$

$$\theta = \frac{\tau_b}{(\rho_s - \rho) g D_{50}}$$

Figure 8 Initiation of motion of fine grained particles. (After Van Rijn, 1993)

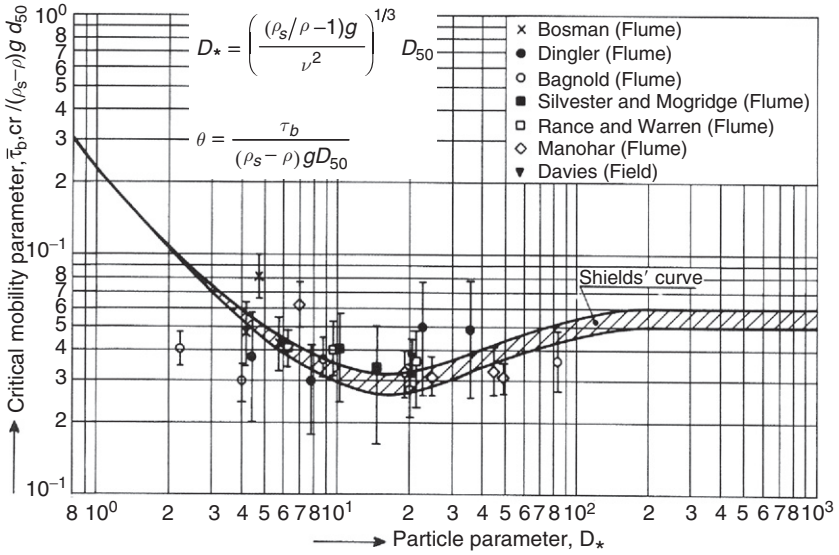

Figure 9 Initiation of motion due to currents and waves. (After Van Rijn, 1993)

magnitude. In this section, we elaborate on floc formation of cohesive sediments.

We note that flocs of cohesive sediment contain clay and silt particles, sometimes some fine sand particles as well, organic material, and a lot of water. Within the organic matter (EPSs, TEP, etc.), polymers are the major active element, inducing effective bonds within the flocs.

Cohesive sediment flocs are small ecosystems by themselves with bacteria, viruses, and, sometimes, algae encapsulated. Droppo et al. (2005) gave an excellent overview on these complicated small systems, with some spectacular photographs.

Figure 10 depicts the settling velocity of single grains in still water. Conditions at which Stokes' law is valid, and modifications read:

- Stokes' regime, that is, $Re_p = W_s D/\nu < 1$,
- particles are not really spherical, and
- for larger particles, drag coefficient needs to be modified – see, for instance, Van Rijn for parametrizations.

Figure 11 shows settling velocities of granular material (sand) for a variety of shape factors and water temperatures. The shape factor SF is defined as

$$F_g = \alpha \frac{\pi}{6} D^3 g\Delta\rho,$$

$$F_d = \beta c_D \frac{1}{2}\rho_w W_s^2 \frac{\pi}{4} D^2,$$

$$c_D = \frac{24}{Re_\rho};\ Re_\rho = \frac{W_s D}{\nu} \le 1\text{: Stokes' regime,}$$

$$W_s = \frac{(\rho_w - \rho_w)\, gD^2}{18\mu}$$ Famous Stokes' law for spherical particles

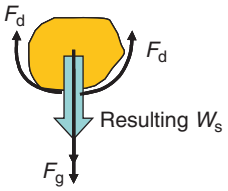

Figure 10 Stokes' settling velocity follows from force balance on falling particles.

$$SF = \frac{a}{\sqrt{bc}}$$

where a is the length of longest axis of ellipsoid enveloping the sand grain, b the length of shortest axis of ellipsoid enveloping the sand grain, and c the length of intermediate axis of ellipsoid enveloping the sand grain. Typically, for natural sediment, SF ≈ 0.7.

However, cohesive sediment particles are not massive, such as sand grains, but are open entities, often characterized by organic filaments, as shown in the photographs of Figure 12. These entities are known as flocs.

In the next part of this section, we show how these structures affect the settling velocity of cohesive sediment mud flocs.

Figure 13 summarizes data on floc density with respect to the density of water as a function of floc size (after Van Leussen (1994)). At very small floc size, excess floc density is only determined by the specific density of the sediment solids.

Typical floc sizes encountered in estuaries and coastal areas range between a few tens of micrometers to around 1 mm. This implies that water is the major component of flocs.

Figure 14 presents a conceptual picture showing the structure of cohesive sediment flocs from their smaller building stones, that is, the clay particles. When these flocs settle, forming the sediment bed, water is squeezed out by (self-weight) consolidation and creep processes. Note that upon consolidation, the bed still contains large amounts of water (see Section 2.15.5). This cartoon is by Partheniades (1986, 2010), one of the great early researchers on cohesive sediments.

In this chapter, we define flocculation as the result of aggregation and breakup processes. Aggregation is the result of collisions between particles and their subsequent coalescence, forming a floc. The collision efficiency describes the rate at which these collisions occur; the aggregation efficiency describes how many of these collisions result in the forming of flocs. These collisions are the result of

- turbulent diffusion related to turbulent shear;
- differential settling – larger, rapid settling flocs overtake smaller and slower flocs; and

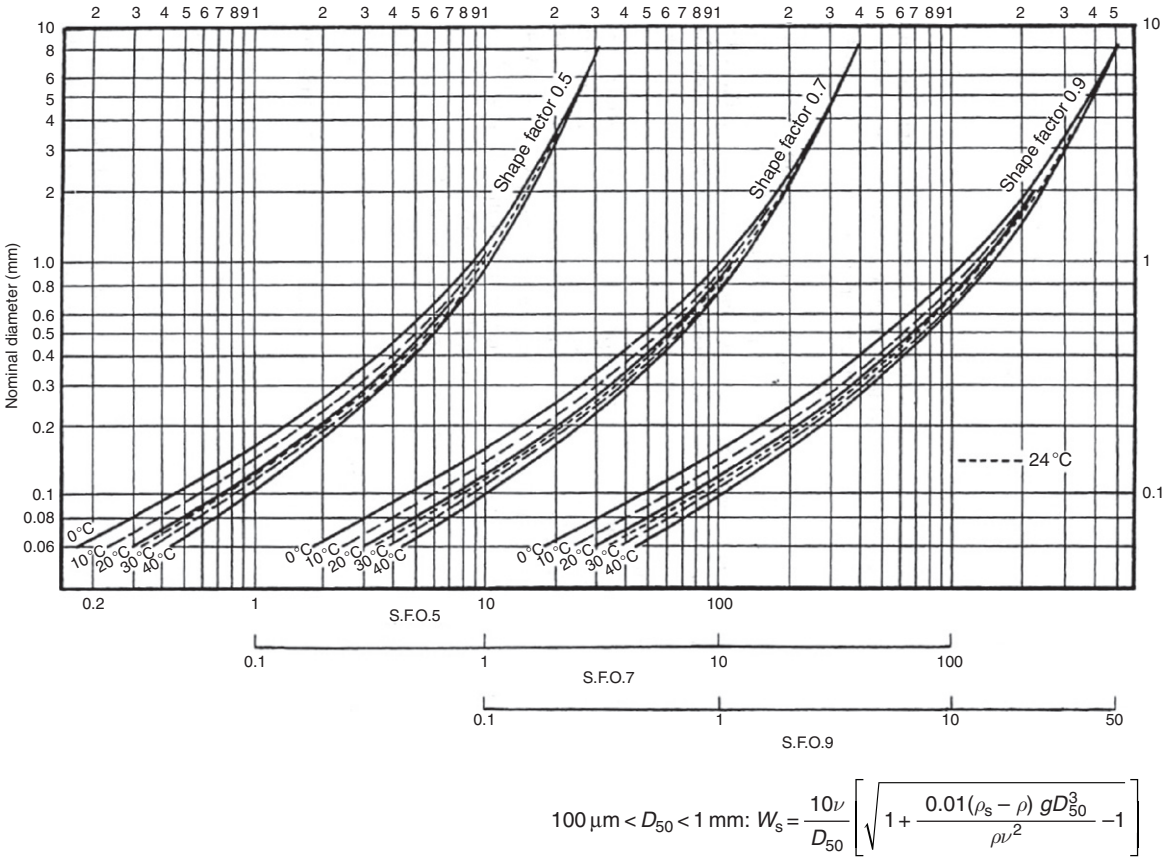

$$100\,\mu\text{m} < D_{50} < 1\text{ mm}: W_s = \frac{10\nu}{D_{50}}\left[\sqrt{1+\frac{0.01(\rho_s-\rho)\,gD_{50}^3}{\rho\nu^2}}-1\right]$$

Figure 11 As sand particles are not really spherical, the particle's shape factor differs from unity, and for larger grains, also the particle Reynolds number starts to play a role. From Raudkivi, 1990.

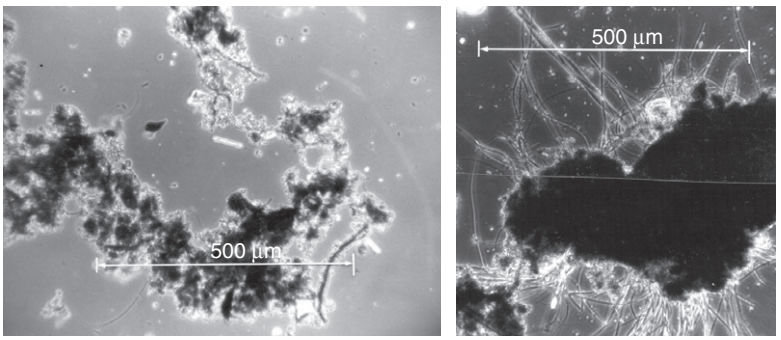

Figure 12 Cohesive sediments form flocs, which are much larger than the constituting particles, and are very porous in general. These freshwater flocs are from the Merwede River, the Netherlands, and are characterized by an abundance of organic filaments.

- Brownian motion – small-scale movements governed by temperature effects.

It has been shown (McCave, 1984; Stolzenbach and Elimelich, 1994) that in estuarine and coastal environments aggregation mainly occurs through turbulent shear. Therefore, the other aggregation mechanisms are further ignored.

Floc breakup is mainly the result of turbulent stresses, of which shear stresses are the more important ones (Van Leussen, 1994). Collisions between flocs most likely do not contribute too much to floc breakup, as small flocs are deflected around the larger ones when approaching, similar to the inefficiency of differential settling.

Numerous observations have shown that flocs cannot become much larger than the Kolmogorov microscale of turbulence; beyond this scale, turbulence-induced forces become so large that floc breakup dominates the flocculation process (more accurately, the moment induced by the stress with respect to floc size becomes too large). The shear stresses at this micro-scale are commonly identified with the symbol G (s^{-1}); for further details, the reader is referred to, for instance, Levich (1962).

There exist many data, from both field surveys and laboratory observations, suggesting that at low shear rates (G), floc size increases with G, whereas at larger shear rate, floc size decreases with G. This is illustrated in the diagram containing data from the

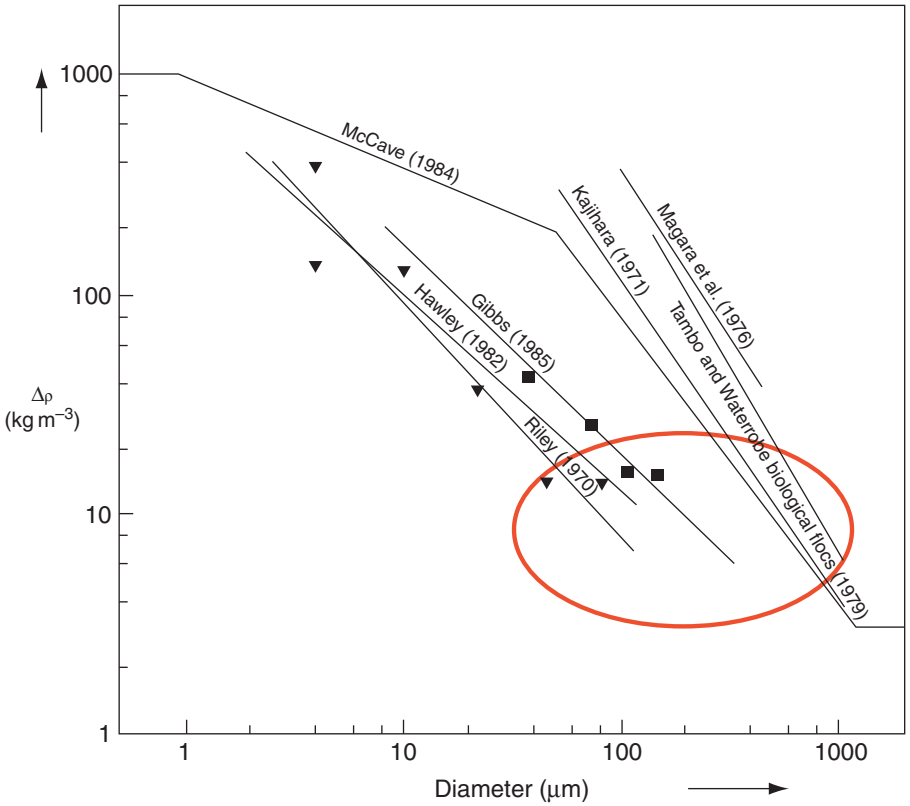

Figure 13 This diagram summarizes observations on excess densities of cohesive sediment flocs. In estuaries and coastal areas, flocs measure typically a few 100 μm, so attain excess densities around 10 kg m^{-3}. The ellipse indicates typical conditions in estuaries and coastal areas. (After Van Leussen, 1994)

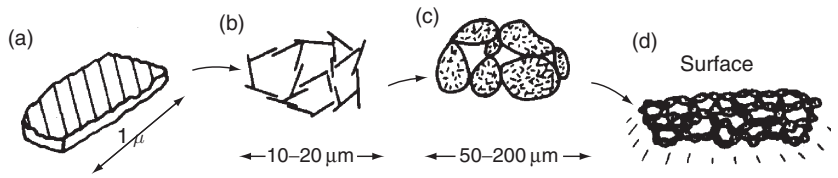

Figure 14 Conceptual picture of floc forming processes and floc squeezing in a consolidating bed. (a) Individual clay particle. (b) Individual floc. (c) Individual floc group. (d) Bed deposit. (After Partheniades, 2010)

Tamar estuary (Manning et al., 2004), showing that below a shear stress $\tau \sim 0.3$ Pa, floc size increases with τ, whereas beyond, an opposite trend is observed, for example, **Figure 15**.

These observations inspired Dyer (1989) to construct his famous conceptual diagram, that is, **Figure 16**, which contains the trend described above, and another observation, that is, that the floc size increases with suspended sediment concentration.

Next, we present a simple flocculation model, enhancing our understanding of the processes relevant for the forming of flocs of cohesive sediment. We limit ourselves to the influence of turbulence, and all physico-chemico-biological effects are parametrized through a number of coefficients, which have to be established from experiment.

Further details of this model are found in Winterwerp (1998), Winterwerp (2002), and Winterwerp and Van Kesteren (2004).

A convenient approach to account for the large amounts of water contained in flocs is the assumption of self-similarity, as shown in **Figure 17**. Self-similarity implies that the floc structure is repetitive at all scales of a floc. More quantitatively, self-similarity can be described with fractal dimensions, as shown below. More information on self-similarity is found in, for example, Vicsek (1992); Kranenburg (1994) was the first to apply the ideas of self-similarity to the structure of flocs of cohesive sediment.

Note that cohesive sediment flocs in general are not (fully) fractal, even if it is only because part of the floc population in the water column is formed through flocculation processes in that water column, whereas another fraction of that floc population may emerge from erosion of the bed, containing far denser flocs because these have been subject to (self-weight) consolidation.

The use of the fractal dimension n_f enables a unique relation between the volumetric and mass concentration of the sediment–water mixture, ϕ and c, respectively, of the cohesive sediment suspension as a function of floc size D_f, and the size of the primary particles (the floc's building stones) D_p. Also, the

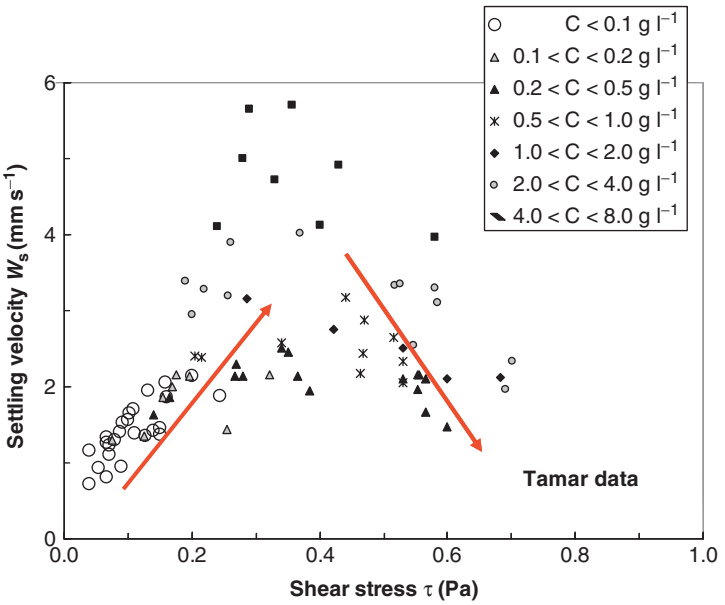

Figure 15 Measured variation in floc size as a function of shear stress (turbulence level). From Manning et al., 2004.

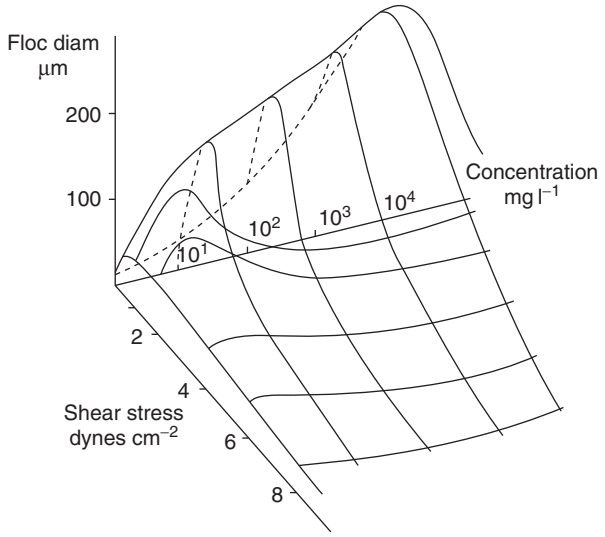

Figure 16 Dyer's (1989) conceptual picture of floc size as a function of shear stress (turbulence) and suspended sediment concentration.

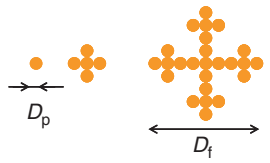

Self-similarity:
Mass ~ length n_f
n_f = fractal dimension:
$1 \leq n_f \geq 3$

This is a convenient way to quantify the porosity of the flocs

Figure 17 Schematic diagram of self-similar flocs.

floc's excess density $\Delta\rho_f$ can be expressed similarly, for example, eqns [1] and [2], in which eqn [1] yields a formal definition:

$$n_f = \lim_{L\uparrow\infty} \frac{\ln(N(L))}{\ln(L)} \qquad [1]$$

$$\Delta\rho_f = \rho_f - \rho_w = (\rho_s - \rho_w)\left[\frac{D_p}{D_f}\right]^{3-n_f} \qquad [2]$$

Note that primary particles do not necessarily consist of the clay minerals themselves. The primary particles are the smallest sediment entities encountered in a specific environment and can be described as coagulates of many clay particles (and possibly other components as well). From eqn [2] we find

$$\phi = \left(\frac{\rho_s - \rho_w}{\rho_f - \rho_w}\right)\frac{c}{\rho_s} = \frac{c}{\rho_s}\left[\frac{D}{D_p}\right]^{3-n_f} \qquad [3]$$

$$c_{gel} = \rho_s\left[\frac{D_p}{D}\right]^{3-n_f} \qquad [4]$$

A space-filling network is formed at a volumetric concentration $\phi = 1$. We refer to this state as a gel. Note that these are the conditions, for example, the space-filling network, we expect to occur in what is commonly known as 'fluid mud' (e.g., Section 2.15.7). Without any further analysis, we already infer that the mass concentration within the fluid mud, c_{gel}, is a function of the floc size D and structure n_f of the flocs that form this fluid mud. The fluid mud concentration, therefore, cannot be universally constant. Moreover, we will see that fluid mud is in a transient state, subject to further densification (consolidation) and/or remobilization by turbulent flow.

Only under very specific conditions, which always require input of external energy, fluid mud layers can be more or less stable. Such conditions are, for instance, found in the mouth of the Amazon River (e.g., Vinzon and Mehta, 2003) where large flow-induced stresses keep the mud layers fluid.

We will continue on the formation and properties of fluid mud layers in Section 2.15.7.

If we apply Stoke's law, that is, assume equilibrium between gravity and hydraulic drag in the Stokes' regime (i.e., the particles' Reynolds number $Re_p = w_s D/\nu < 1$), we obtain an

alternative expression for the settling velocity of fractal flocs; in particular, the effect of floc's porosity is found in the excess density of the flocs, as shown in eqn [2].

The coefficients α and β reflect the particles' shape, being unity for spherical particles:

$$w_s = \frac{\alpha}{18\beta}\frac{(\rho_s-\rho_w)g}{\mu}D_p^{3-n_f}\frac{D_f^{n_f-1}}{1+Re_p^{0.687}} \quad [5]$$

From a collection of data, we infer that the fractal dimension is around $n_f \approx 2$. In practice, we encounter fractal dimensions between 1.7 and 2.3 for flocs formed in the water column (**Figure 18**, e.g., Winterwerp and Van Kesteren, 2004), with lower values at higher organic contents. Note that within the bed, the fractal dimension can be much larger, that is, up to 2.6–2.8; this is discussed in Section 2.15.5.

As mentioned, the fractal dimension is not expected to be constant, as cohesive sediment flocs are not really self-similar (**Figure 19**). A simple extension was proposed by Maggi et al. (2007), relating the fractal dimension (or capacity dimension) to the floc size, bearing in mind that at primary particle size (in particular, when the particles consist of the original clay minerals) should approach the value of massive, Eulerian particles, that is, $n_f = 3$.

Next, we introduce a rate equation, relating the growth of floc size D_f to an aggregation and a breakup term. We deal with mean (or median) floc size only, for simplicity. The aggregation term follows from a description by Smoluchowski (1917) for turbulence-induced aggregation in which we introduced an efficiency term (collision and aggregation efficiency) k_A. The breakup term follows from dimensional analysis, introducing an efficiency term k_B, accounting for the strength of the flocs, etc. The various coefficients and exponents follow from empirical evidence that the equilibrium floc size D_e scales with the Kolmogorov microscale of turbulence λ_0, that the equilibrium settling velocity $W_{s,e}$ scales with the sediment mass concentration c, and that the fractal dimension takes a mean value $n_f = 2$. This model is given in eqns [6]–[9]:

$$D_e \propto \lambda_0\ ,\ W_{s,e} \propto c\ ,\ n_f = 2 \quad [6]$$

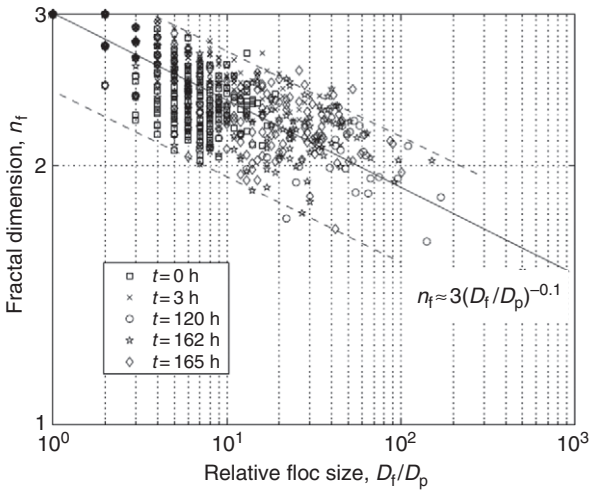

Figure 19 Recent data suggest that the fractal dimension is not constant, but decreases with floc size. (After Maggi et al., 2007)

$$\frac{dD}{dt} = k_A c G D^2 - k_B G^{3/2} D^2 (D - D_p) \quad [7]$$

$$G = \sqrt{\frac{\varepsilon}{\nu}} = \frac{\nu}{\lambda_0^2} \quad [8]$$

$$D_{f,e} = D_p + \frac{k_A c}{k_B\sqrt{G}} \quad [9]$$

where $D_{f,e}$ is the equilibrium floc size. The coefficients k_A and k_B have been obtained through calibration of the model against laboratory experiments in a full-scale settling column with cohesive sediments from the Ems estuary, carried out by Van Leussen (1994). Further background on this Lagrangian model can be found in Winterwerp (1998) and Winterwerp and Van Kesteren (2004).

From this calibration against laboratory experiments with mud from the Ems River (the Netherlands/Germany), we found the following values for the coefficients: $k_A = 14.6\ m^2\ kg^{-1}$ and

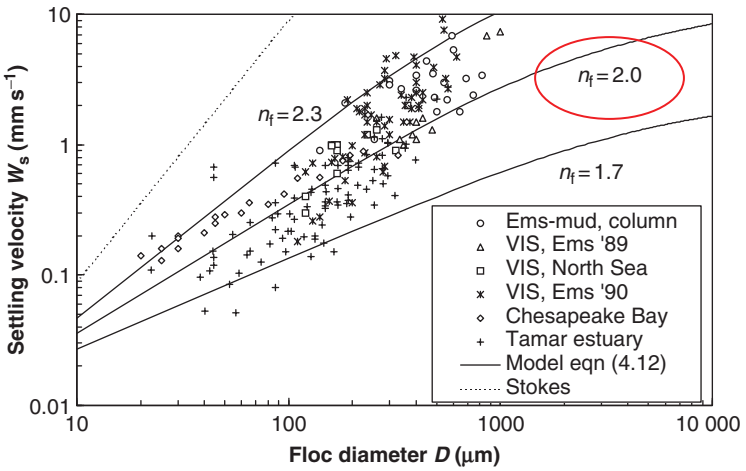

Figure 18 Settling velocity as a function of floc size; various data and relation based on fractal approach (eqn [5]). Note that Stokes' law greatly overpredicts W_s. (After Winterwerp, 1998)

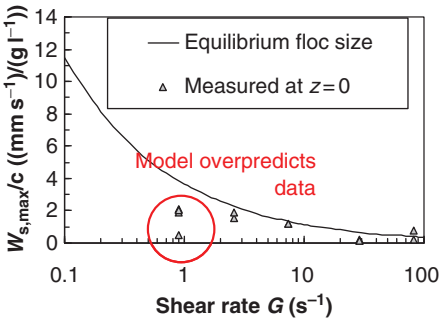

Figure 20 Settling velocities in settling column do not attain equilibrium values because of limited residence time (Winterwerp and Van Kesteren, 2004).

$k_B = 14.0 \times 10^3$ s^{½} m^{-2}. Note that these values may be different for other sediments, depending on clay mineralogy and organic matter. Moreover, k_A and k_B are dimensional coefficients, as they include of a number of other coefficients and parameters (e.g., Winterwerp, 1998).

From this flocculation model, the equilibrium floc size can be established, scaling with $G^{-0.5}$, for example, eqn [9]. As the settling velocity W_s scales with D_f for $n_f = 2$, also W_s scales with $G^{-0.5}$. To facilitate comparison with data at various mass concentrations, we have divided $W_{s,e}$ with c. We observe in Figure 20 that at larger G, the model describes the $w_{s,e}/c$ observations properly, but at smaller G, the model overpredicts the observations considerably. This picture is qualitatively similar to that proposed by Dyer.

Figure 21 shows the results of small-scale flocculation tests, carried out by Mietta et al. (2009) in a 10-cm large jar in which mixing and associated flocculation are induced by an impellor. Tests are carried out with polystyrene particles in a saltwater solution of density 1055 kg m^{-3}, and with silica particles in the same fluid. The equilibrium floc size of the neutral polystyrene particles follows the Kolmogorov microscale over the entire range of shear rates. However, the maximum floc size of the negatively buoyant silica particles only follows the Kolmogorov microscale for $G > 35$ s^{-1}. At smaller shear rates, turbulent mixing is too small to keep the silica particles in suspension, and small deposits of silica are observed on the bottom of the jar. Note that this threshold value of 35 s^{-1} is a function of the settling velocity of the particles and the mixing capacity of the experimental device (jar); hence, this threshold value is not a universal constant.

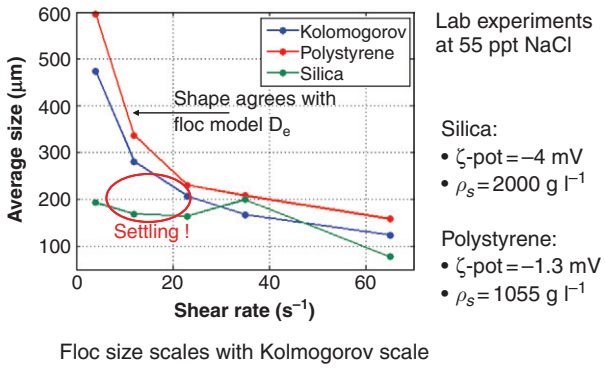

Figure 21 Floc sizes in mixing beaker do not attain equilibrium because of sedimentation, except for neutrally buoyant particles (Mietta et al., 2009).

From these observations, we infer that the large silica flocs formed at the lower shear rates will settle, and, therefore, do not have enough time to grow to their equilibrium size. In other words, we conjecture that the increase in floc size with G at low G, conceptualized by Dyer (1989), can be explained by comparing the flocculation time to achieve equilibrium with the residence time of the flocs in the floc-forming (turbulence) conditions.

The flocculation model (rate equation) implicitly yields the time to attain equilibrium, starting from flocs that are either much smaller or much larger than the equilibrium value. Equation [10] shows that the breakup time (i.e., initially flocs are larger than equilibrium values, as would occur in conditions of increasing shear) is generally much smaller than the aggregation time (i.e., initially flocs are smaller than equilibrium values, as would occur in conditions of decreasing shear). Hence, the flocculation time T_f scales with $(k_A c G D_0)^{-1}$, where D_0 is the initial floc size. If we substitute a variety of values for the various parameters, assuming $k_A = 14.6$ m^2 kg^{-1} (e.g., Winterwerp, 1998), we infer flocculation times varying from a few minutes to many days, depending on the relevant hydrosedimentological conditions:

$$\text{for } D_{f,e} \gg D_0 \quad T_f \approx T' D_{f,e}/D_0 \approx \frac{1}{k_A c G D_0}$$

$$\text{for } D_{f,e} \ll D_0 \quad T_f \approx 2T' \approx \frac{2k_B}{k_A^2 c^2 \sqrt{G}} \qquad [10]$$

$$\text{hence: } T_f \propto \left(\frac{U^3}{h}\right)^{-n} c^{-m} \text{ with } \tfrac{1}{4} \le n \le \tfrac{1}{2}, 1 \le m \le 2$$

We can account for the limited residence time of flocs in a floc-forming environment by computing the settling time of flocs from a certain height Z_0 (see Figure 22). The resulting integral equation can be solved analytically for $n_f = 2$, as shown in Winterwerp (1998). Its solution is given in eqn [11], and plotted in Figure 23.

$$w_{s,max} = \frac{w_{s,0}}{\left(\frac{D_{f,e} - D_0}{D_{f,e}}\right) e^{-Z_0/w_{s,e}T'} + \frac{D_0}{D_{f,e}}} \qquad [11]$$

Figure 23 shows that the maximal floc size seems to increase with shear rate at small shear rate. This is not caused by a dominance of flocculation processes at small G, but because the larger flocs settle out, before they can achieve equilibrium.

The importance of the relation between flocculation and residence time can be further illustrated in the water depth–shear velocity graph of Figure 24, in which lines have been drawn along which $T_f = T_r$; T_f is a function of the suspended sediment concentration c as well.

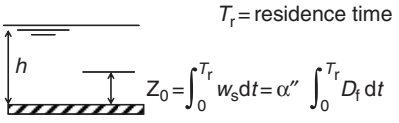

Figure 22 Sketch of reference level and residence time.

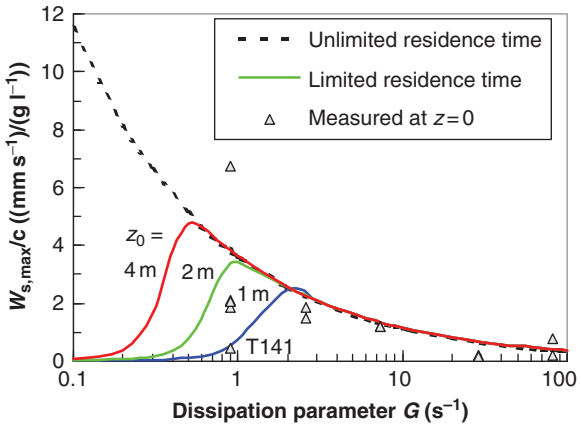

Figure 23 Computed effect of limited residence time on maximal settling velocity.

Let us analyze the conditions at $c = 50\,\mathrm{mg\,l^{-1}}$, a characteristic value found in many rivers in the world. At typical shear velocities of a few $\mathrm{cm\,s^{-1}}$, we can expect full (i.e., equilibrium) flocculation only in rivers with a depth exceeding a few tens of meters. This does not imply that the cohesive sediment does not form flocs, but that these flocs do not yield equilibrium values (i.e., they are not in equilibrium with the local hydrodynamic conditions). Instead, the flocs under such conditions are expected to attain values in equilibrium with the larger shear rates found in a river, that is, near the bed. We expect little variation in space (over the length of the river, and also not over depth and width) or time in floc size; the flocs have a long memory. In other words, floc size is more or less constant.

We have reformulated the above Lagrangian flocculation model into a fixed frame of reference (Eulerian description). This model has been implemented in a one-dimensional (vertical) model (1DV point model), which is basically a 3D model from which all horizontal gradients have been stripped, except for the pressure term. The following equations are resolved in this 1DV model (Winterwerp, 2002):

- momentum equation,
- k–ε turbulence model (including buoyancy effects),
- mass-balance equation,
- no waterbed exchange (all sediment in domain),
- equation of state,
- formulation for hindered settling,
- Eulerian flocculation equation, and
- parameters flocculation model from settling column experiments.

The effects of sediment concentration (gradients) on the water movement and turbulence production are accounted for through the equation of state. In the numerical experiments presented in this treatise, all sediment is kept within the computational domain, that is, no sedimentation or erosion takes place, unless stated otherwise. As mentioned, the parameters in the flocculation model (k_A and k_B) have been established from calibration against settling column experiments.

Figure 25 presents the results of computed variations of the settling velocity over the water depth and over the tidal cycle for Ems conditions, for example, Winterwerp (2002). At the higher concentrations in the Ems estuary, flocculation times decrease rapidly and we find large variations in W_s, as was observed, for instance, by Van Leussen (1994) in the Ems estuary (Figure 25), where settling velocities varied from 0.5 to about $3\,\mathrm{mm\,s^{-1}}$ over a tidal cycle.

Also a Eulerian version of the Lagrangian flocculation model, implemented in the 1DV model, as discussed above, predicts large variations in time and over the water depth for conditions similar to those in the Ems estuary, and at a mean mass concentration $c = 500\,\mathrm{mg\,l^{-1}}$.

The Lagrangian flocculation model can be solved analytically only when $2 \times n_f$ is integer. Therefore, an approximate analytical solution has been derived in Winterwerp et al. (2006), in which the effects of a limited residence time have been included, and a number of coefficients have been introduced, which appeared to be more or less constant for the cases

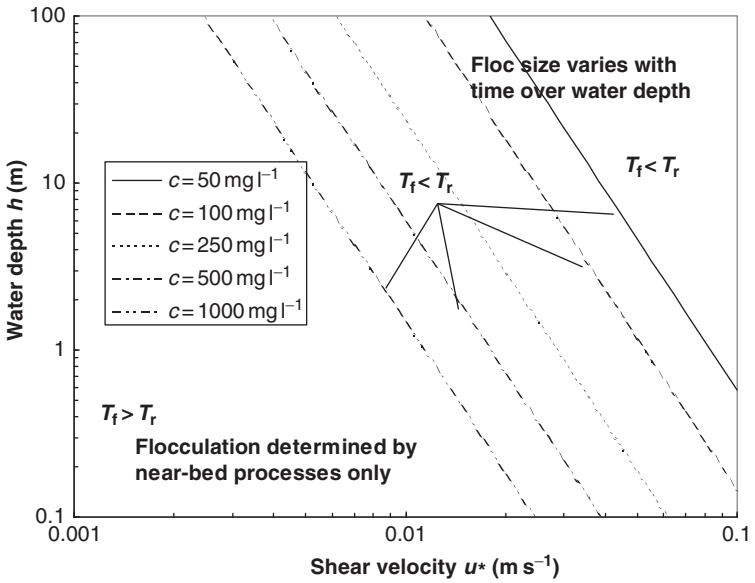

Figure 24 Phase diagram indicating when dynamic flocculation processes are important.

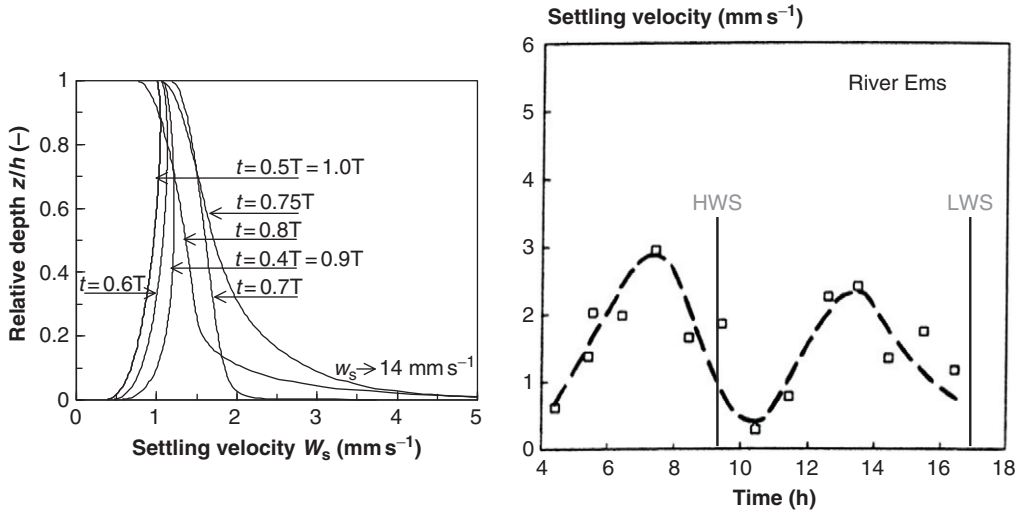

Figure 25 (Left) Computed variation of settling velocity over water depth and tidal cycle (for Ems conditions). (Right) Time-varying observations in the Ems estuary (e.g., Van Leussen, 1994; Winterwerp, 2002).

investigated (i.e., the Tamar River, the Lower Sea Scheldt, and the Gironde River), for example, eqn [12]:

$$W_{s,\max} = \left[k_4 \frac{c^{1/2q}}{\tau^{3/8}} - k_2 \left(k_4 \frac{c^{1/2q}}{\tau^{3/8}} - \alpha'' D_0 \right) \exp\left\{ -\frac{k_3 \tau^{9/8} h}{n_f} \right\} \right]^{n_f - 1} \quad [12]$$

A comparison of eqn [12] with data from the Tamar estuary is presented in **Figure 26**, showing a fair agreement.

We note that the above analysis relates to a mean or median floc size only. In reality, cohesive sediments form a spectrum of floc sizes, a so-called floc size distribution, sometimes with

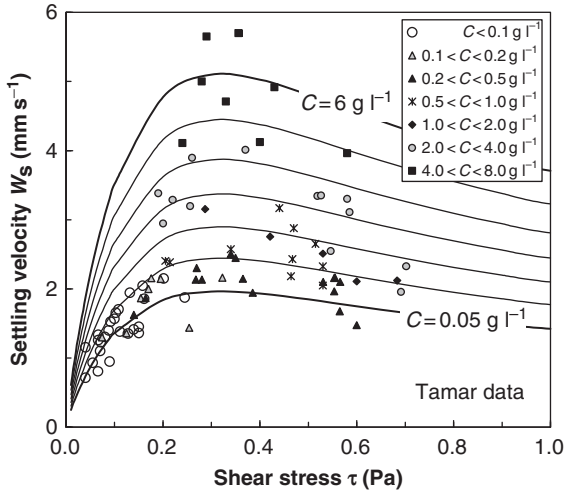

	n_f	k_2	k_3	k_4	n_0 (μm)	m	h (m)
Tamar	2.2	1	5	0.007	10	0.2	3
Scheldt	2.15	1	5	0.007	10	0.44	15
Gironde	2.25	1	5	0.007	10	0.2	10

Figure 26 Measured and computed (heuristic model) variation of settling velocity with shear stress – table yields parameter settings, where $q = (n_f - 1)/2m$; e.g., Winterwerp et al. (2006).

two distinct peaks, as shown in the results by Benson and French (2007) (presented in **Figure 27**).

Manning and Dyer (2002) distinguished between micro- and macroflocs, with a transition around 160 μm, as often the smaller microflocs are much denser (larger n_f) than the macroflocs. Although no definite explanations exist on the physical processes responsible for this bimodal behavior, it may be hypothesized that the microflocs stem for remobilization of fine sediments from the bed, whereas the larger macroflocs have resided within the water column for a longer period of time.

The efficiency of aggregation (hence flocculation) depends strongly on the chemical environment. In particular, at low pH, flocculation can be rapid. In marine waters, pH is typically ≈8, and salinity is the only varying parameter. The effects of chemistry are sketched in **Figure 28**. For more information, the reader is referred to Chassagne et al. (2009).

The literature contains a number of confusing analyses on the deposition rate of fine cohesive sediment. A parametrization by Ariathurai and Arulanandan (1978) of the results of Krone's flume experiments (Krone, 1962) is referred to as 'Krone's deposition' formula in honor of Ray Krone. This parametrization is based on the paradigm that in a system with a suspension of cohesive sediment over a bed of cohesive sediment, erosion, and deposition cannot occur simultaneously. This paradigm is based on experiments in a rotating annular flume done by Partheniades and his colleagues. However, it can be shown that Partheniades experiments and those by Krone can be also explained if this paradigm is not adopted. The experiments and arguments leading to this paradigm and the alternative explanation have been discussed in detail by Winterwerp (2007) and Winterwerp and Van Kesteren (2004).

Sanford and Halka (1993) and Winterwerp (2007) proposed that the sedimentation rate D equals the sediment flux at the bed:

$$D = w_{s,b} c_b \quad [13]$$

where $w_{s,b}$ is the effective settling velocity of flocs near the bed; effective implies accounting for flocculation, hindered settling, etc., and c_b is the near-bed-suspended sediment concentration.

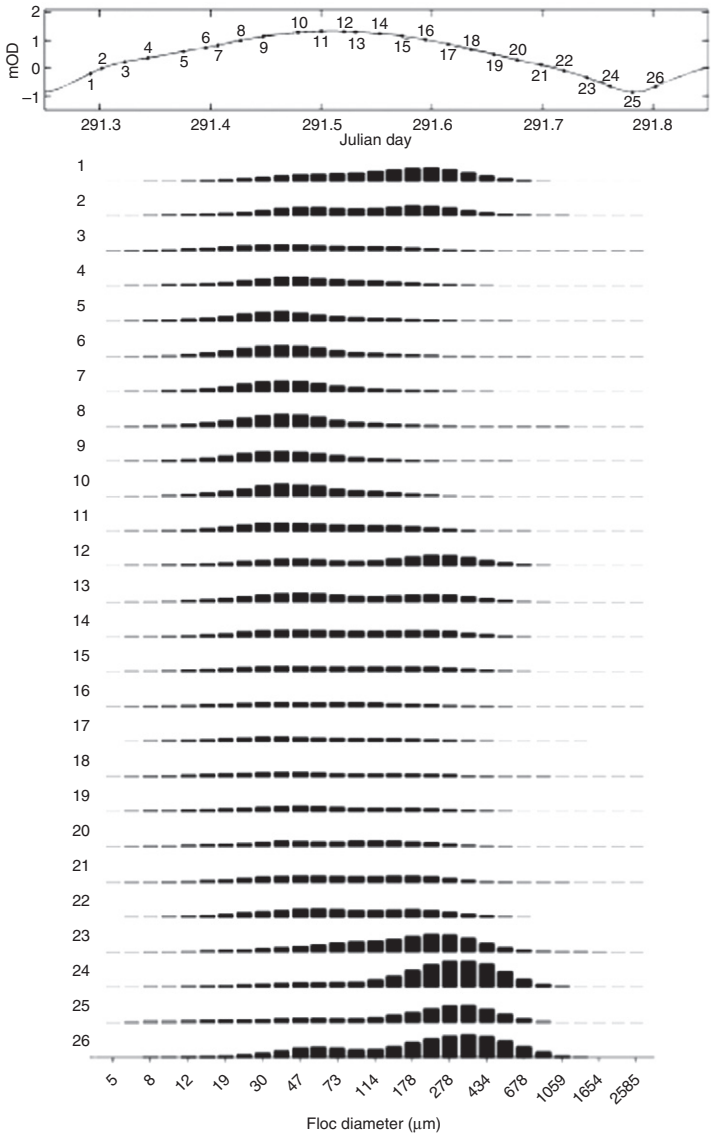

Figure 27 Measured variation in floc size over a tidal cycle by Benson and French (2007) – note the occurrence of bimodal distributions (note log scale).

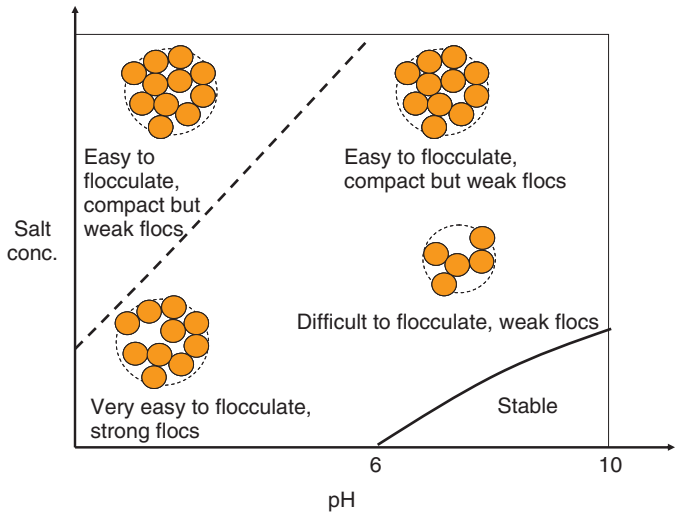

Figure 28 Diagram of flocculation kinetics as a function of chemical environment.

The gross deposition rate D ($\mathrm{kg\,m^{-2}\,s^{-1}}$) is identical to the gross deposition rate commonly used in the formulation for noncohesive sediments, and is therefore attractive to use. It is important to realize that the suspended sediment concentration is characterized by vertical gradients, and the settling velocity too in the case of sufficient small flocculation times. These vertical structures are resolved automatically in 3D models if an appropriate flocculation model is accounted for as well.

Another important implication is that in the case of a pronounced distribution in floc size, the gross deposition rate does not equal the product of the mean (median) settling velocity and the total suspended sediment concentration (near the bed), as the sediment mass is not proportionally distributed over the flocs:

$$D_{\mathrm{tot}} = \int_{c_\mathrm{b}} w_{\mathrm{s,b}}\, \mathrm{d}c_\mathrm{b} = \sum_n w_{\mathrm{s,b,i}} c_{\mathrm{b,i}} \qquad [14]$$

Currently, no universally valid formulations for floc size distribution have been developed. Therefore, we cannot derive a general law/rule computing the gross sediment flux to the bed in the case of pronounced distributions in floc size. However, let us elaborate on the settling velocity distribution sketched in Figure 29, with a median settling velocity $W_{s,50} = 0.5\,\mathrm{mm\,s^{-1}}$, typical for fine cohesive sediments in the marine environment. We have normalized the distribution to $100\,\mathrm{mg\,l^{-1}}$ total mass concentration. The settling flux $D_{50} (= W_{s,50} \times \bar{c})$ then would yield $50 \times 10^{-6}\,\mathrm{kg\,m^{-2}\,s^{-1}}$. However, if we would compute the settling flux correctly from an integration of $W_s \times c$ per fraction, we find $D_{\mathrm{tot}} = 64.3 \times 10^{-6}\,\mathrm{kg\,m^{-2}\,s^{-1}}$, that is, 25% larger than D_{50}. This, of course, is due to the bias to the larger particles, as explained earlier.

The so-called Krone formulation for deposition (e.g., Krone, 1993) reads as

$$D = w_\mathrm{s} c \left(\frac{\tau_\mathrm{d} - \tau_\mathrm{b}}{\tau_\mathrm{d}} \right) \text{ for } \tau_\mathrm{b} < \tau_\mathrm{d};\quad D = 0 \text{ for } \tau_\mathrm{b} > \tau_\mathrm{d} \qquad [15]$$

where τ_d is the critical shear stress for deposition. Typical values for τ_d would range from 0.01 to 0.5 Pa. Remarkably, in his original report, Krone (1993) presented a relation similar to the one above, but refers to a threshold for erosion. Note that we have omitted the subscripts $_\mathrm{b}$ in Krone's formulation, for reasons to become clear below.

Though Krone's formulation is not necessary to explain the observations by both Krone and Partheniades, the use of Krone's formulation may be useful in engineering studies, in particular in the case of depth-averaged modeling. In that case, the net settling of flocs is opposed by vertical turbulent mixing (the balance between these two effects yields the vertical suspended sediment concentration gradients commonly observed in the water column). As vertical mixing is not resolved in a depth-averaged model, Krone's formulation can be regarded as a useful parametrization of that effect. More generally, Krone's formulation is useful in all cases where the vertical structure in the water column is not properly resolved, in which case calibration of the sediment transport model may appear difficult with the use eqn [13].

There is an ongoing discussion on the correct values of the settling velocity of mud flocs. Measured settling velocities often exceed the values adopted in numerical models after calibration (where settling velocity is tuned to reproduce, e.g., observed siltation rates). Floc size distributions are measured, from which the settling velocity is determined using Stokes' law, accounting for the effective density of the flocs, or, vice versa, the floc size distribution is determined from settling velocity measurements. Some studies focus on water-quality issues, others on predicting dredging rates. These arguments mainly indicate that no universal recipes can be given to establish settling velocities. However, the reader can use the theory and observations discussed above to make a proper assessment of the values to be used in their own applications. Hence, it is important to realize that a unique settling velocity of cohesive sediment flocs does not exist:

- the settling velocity is characterized by a distribution, often bimodal – we have shown that the total sedimentation flux does not equal the product of the median settling velocity and total suspended sediment concentration;
- the settling velocity (distribution) varies because of flocculation and hindered settling (next section);
- as contaminants adhere to finer fractions, we are interested in these finer fractions for water-quality problems;

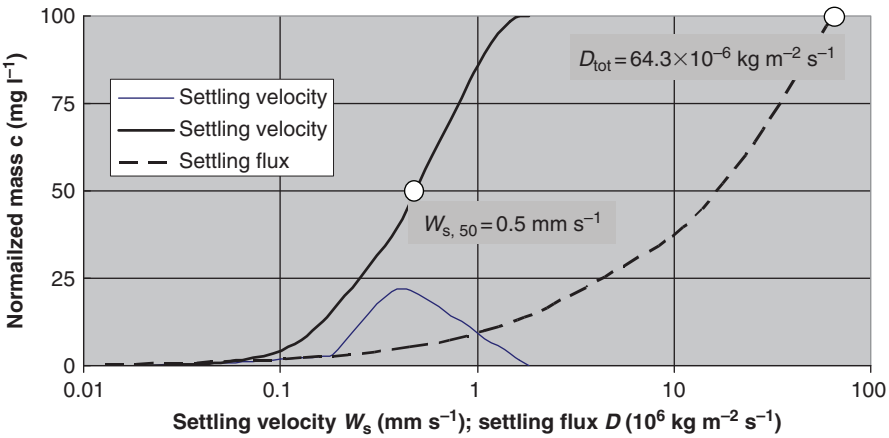

Figure 29 Example of settling flux computed from mean concentration and median settling velocity and from a proper integration of an assumed particle size distribution.

- for ecological problems, we are often interested in the organic components and the finer fraction as well – the first contributes to the food web, whereas the latter to the aquatic light climate;
- for siltation studies (dredging!), the courser fraction is of importance, as it determines the siltation volumes;
- as discussed in the previous pages, the kind of modeling (2D, 3D, and yes/no flocculation) also determines the settling velocity to be used; and
- finally, one should realize that the settling velocity in a numerical model is not an independent parameter – the performance of a model (agreement with observations) depends on all parameter settings (erosion, sometimes consolidation, settling, and deposition), input of sediments, and schematization of the physical domain and hydrodynamic forcing.

2.15.4 Hindered Settling and Consolidation

In Section 2.15.3 we discussed the settling velocity of individual particles and flocs in still water. When the suspended sediment concentration increases, particles/flocs start to hinder each other, while settling, for example, **Figure 30**. As a result, the settling velocity decreases, and a kind of traffic jam develops, forming an interface (lutocline) in the water column.

This lutocline is characterized by vertical density gradients, locally quite large, which may cause significant damping of vertical turbulent mixing, reducing sediment concentrations above the lutocline further. This feedback plays an important role in the formation of fluid mud, as explained in Section 2.15.7.

When the sediment concentration increases further, a spatial network develops, referred to as a gel. These are typically the conditions of fluid mud formation ($\phi = 1$; $c = c_{gel}$). C_{gel} follows from a flocculation model or is estimated from observations; typical values range from around 20 to 150 g l^{-1}.

Interaction, or mutual hindrance between settling flocs, is the result of a number of processes:

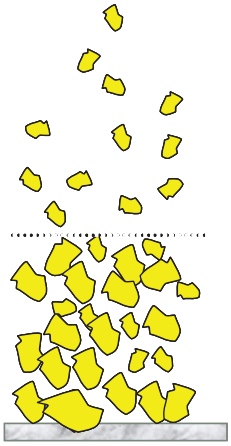

Figure 30 Cartoon of hindered settling of mud flocs, forming a lutocline where fast settling particles overtake slower ones.

1. return flow and wake formation,
2. nonlinear deformations of flow field,
3. particle–particle collisions,
4. particle–particle interactions (attractions),
5. augmented viscosity,
6. reduced gravity (buoyancy effects), and
7. cloud formation.

We focus on the processes 1, 5, and 6. A basic assumption in our analysis is that any particle in a high-concentrated suspension settles in the remainder of the suspension, which explains the effects of augmented density and viscosity.

Cloud formation is poorly understood. It plays a role in the behavior (settling) of clouds of fine sediment, as encountered, for instance, in the overflow of hopper dredgers.

Two of the three processes treated here are related to the volumetric concentration of the suspended sediment. In suspensions of cohesive sediment, this volumetric concentration is determined by the floc size. As discussed in Section 2.15.3, flocs are very open sediment structures, and yield large-volume concentration at relatively small mass concentration. In suspensions of noncohesive sediment (sand), hindered settling may play a role as well, but at far larger mass concentrations (sheet flow).

A well-known formula describing the effect of hindered settling was derived by Richardson and Zaki (1954) on dimensional grounds:

$$w_s = W_{s,r}(1-kc)^n \qquad [16]$$

The exponent n is basically a function of the particle Reynolds number, and attains values between 4 and 5 for fine suspended sediment. As this formula is difficult to extend to multifraction suspensions, Winterwerp (2002) developed another relation, accounting for the three processes mentioned above. Return flow, augmented density, and augmented viscosity are given by

$$w_{s,eff} = w_{s,r} - v_f = w_{s,r} - \phi_f w_{s,eff}/(1-\phi_f)^m \qquad [17]$$

$$\mu_{eff} = \mu_0(1 + 2.5\phi_f) \qquad [18]$$

$$\rho_s - \rho_{w,eff} = \rho_s - [\rho_s\phi_s + (1-\phi_s)\rho_{w,0}] \qquad [19]$$

Combination of the various effects yields

$$w_s = w_{s,r}\frac{(1-\phi)^m\left(1-\phi_p\right)}{1+2.5\phi} \qquad [20]$$

We have added an exponent m to the effect of return flow to account for nonlinear effects (see below). In the above formulas, $w_{s,r}$ is the relative settling velocity of single floc in still water, $w_{s,eff}$ the effective settling velocity of flocs as a result of hindered settling, ϕ_f the volumetric concentration of cohesive sediment based on floc size, ϕ_s the volumetric solids concentration (primary particles), μ_0 the viscosity of clear water, μ_{eff} the effective viscosity of sediment suspension, ρ_s the specific sediment density, and ρ_w the specific water density.

Observations on a decrease in settling velocity as a result of hindered settling can be captured reasonably with Winterwerp's formula, using the various gelling concentrations given in **Figure 31**. We discussed the large variations in c_{gel} (fluid mud concentrations) in Section 2.15.3. We note that

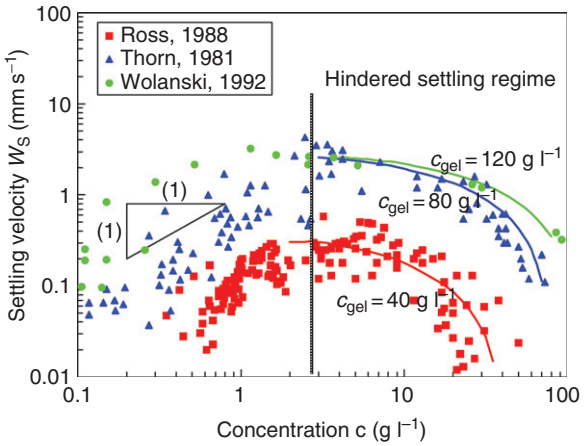

Figure 31 The hindered settling regime for flocs of cohesive sediment starts at relative small mass concentration (a few g l^{-1}) owing to the large water content of the flocs (Winterwerp, 2002).

hindered settling can become manifest at already low mass concentrations, which is the result of the large water content of the flocs.

Kynch (1952) analyzed the simple wave equation describing the process of hindered settling. The sketches in **Figure 32** are from Kranenburg (1992), who completed Kynch's analysis. The graphs on the left side of the slide depict settling of a sediment suspension, initially homogeneously mixed over a settling column. The graphs show the lowering of the sediment surface, and the evolution of the characteristics, describing the solution of the simple wave equation. Depending on the initial conditions, also a second interface lower in the column is developed (see upper graph), as elaborated below. This second interface can be regarded as the bed that moves upward from the bottom of the settling column.

On the right side of the graph, the development of interfaces is sketched at various times t_0, t_1, etc. Initially, the suspended sediment concentration over a large part of the column maintains its initial value c_0.

Note that **Figure 32** and the following analyses are valid for ideal conditions with monodispersed sediment (e.g., one grain size only). First, we describe the vertical sediment balance of a settling suspension in still water. For the time being, the function $f(\phi)$ is an arbitrary hindered settling function, and S is the settling flux.

$$S = w_s\phi \text{ and } w_s = w_{s,0}f(\phi) \text{ and } \frac{\partial\phi}{\partial t} + \frac{\partial S}{\partial z} = 0 \qquad [21]$$

Substitution yields

$$\frac{\partial\phi}{\partial t} + w_{s,0}F(\phi)\frac{\partial\phi}{\partial z} = 0 \text{ where } F(\phi)\frac{d}{d\phi}[\phi f(\phi)] \qquad [22]$$

From the behavior of the function $F(\phi)$, we can establish under which conditions a second interface in the lower part of the suspension is formed.

We observe that the function F has an inflection point at ϕ_{cr} if we use the hindered settling formula by Richardson and Zaki, or the hindered settling formula [20], when we use $m = 2$ for nonlinear effects. This implies that for $\phi < \phi_{cr}$, two interfaces in the settling sediment suspension are expected, whereas for $\phi > \phi_{cr}$, only a water–sediment interface is expected.

For $m = 1$, we always find two interfaces ($dF/d\phi$ always <0). This behavior is shown in **Figure 33**.

From sediment concentration measurements in a suspension settling in a settling column, the characteristic lines can be determined. **Figure 34** shows results by Dankers and Winterwerp (2007). Comparing with the idealized sketch by Kynch in **Figure 32**, we recognize the occurrence of a second interface in the left panel.

Note that in both experiments the same mud was used, the initial concentration in the right column though was higher than in the left.

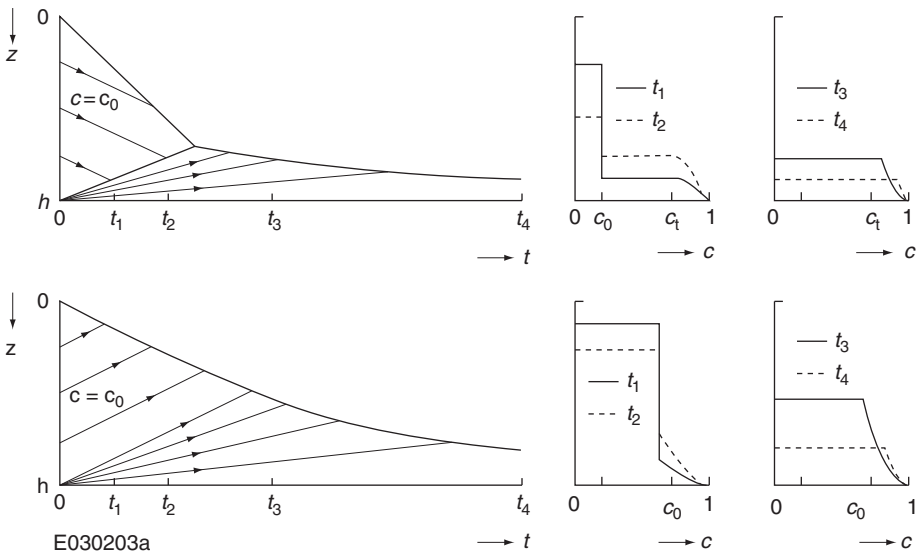

Figure 32 Sketches of the hindered settling process of a suspension in still water. The arrows in the left-hand-side figures depict the characteristics of the solution to the simple wave equation, and their direction in time-space. (Redrawn from Kranenburg, 1992)

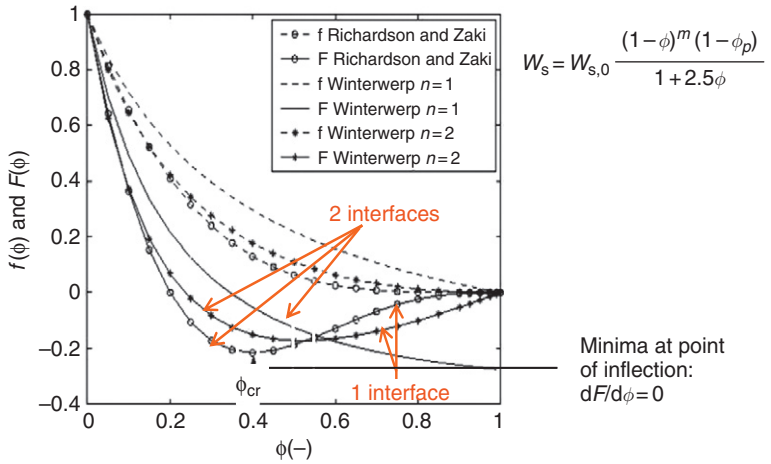

Figure 33 Behavior of the hindered settling functions *f* and *F* as a function of the various hindered settling formulas and related coefficients.

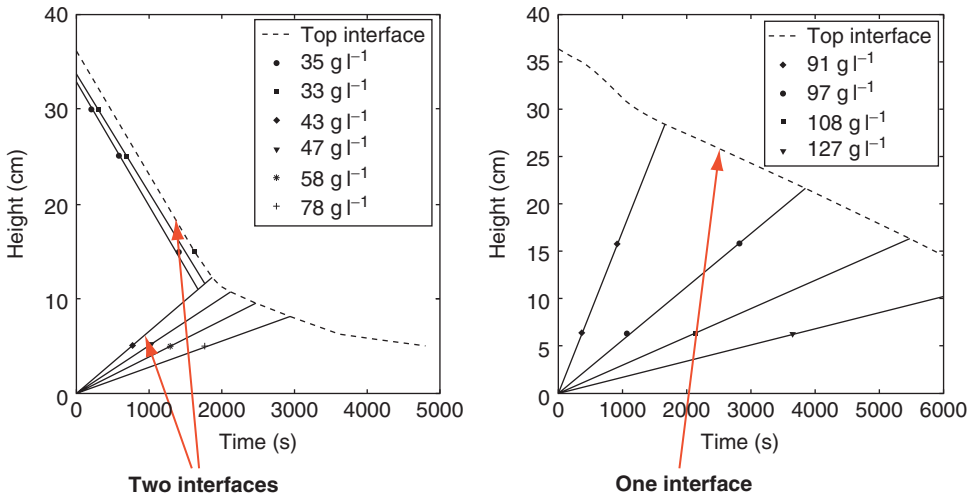

Figure 34 Results of hindered settling experiments in the laboratory – we have added lines of equal concentration, that is, the characteristics. (After Dankers and Winterwerp, 2007)

From these observations, we infer that the behavior of suspensions can change from developing two interfaces to one interface, when a certain threshold concentration is exceeded. This implies that m should be >1, for example, $m = 2$. This has been elaborated in detail by Dankers and Winterwerp (2007):

$$w_s = w_{s,r} \frac{(1-\phi)^m \left(1-\phi_p\right)}{1+2.5\phi} \qquad [23]$$

In Figure 35, we compare the two hindered settling formulas by Richardson-Zaki and Winterwerp ($m = 2$) with column data. We have implemented these formulas in the 1DV model of Winterwerp (2001). Both formulations give a fair description of the data, except at concentrations beyond $\phi = 0.6$–0.7. In this regime, consolidation starts, which is the subject of the remainder of this section.

Next, we derive an advection–diffusion equation describing consolidation of cohesive sediment; we propose a heuristic

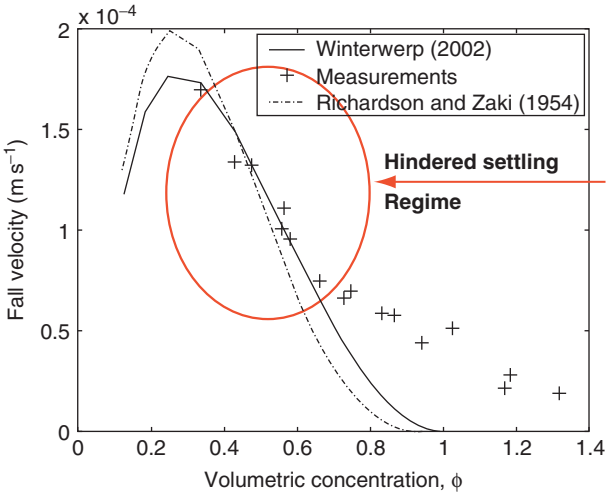

Figure 35 Results of hindered settling experiments and comparison with hindered settling formulas (after Dankers and Winterwerp, 2007). Note that for $\phi > \sim 0.6$, consolidation effects start to play a role.

formulation to model the transition from the hindered settling to consolidation regime:

- when the flocs start to form a space-filling network, stresses build up within the suspension,
- in that case we no longer refer to the process of hindered settling, but to the process of consolidation,
- consolidation, which is treated extensively in soil mechanics, is a discipline by itself – we only discuss those aspects relevant to understand erosion of the bed (Section 2.15.6) and the behavior of fluid mud (Section 2.15.7), and
- in this treatise, we treat self-weight consolidation only, as does occur commonly in nature.

Figure 36 shows the development with time of the density in a consolidation column. As we observe no distinct interface near the bottom of the column, we anticipate that the initial conditions are beyond the critical value ϕ_{cr}, discussed in the section on hindered settling. In fact, the initial conditions are already beyond the gelling value, thus beyond the hindered settling regime. The graph on the right-hand-side panel is by Toorman and Berlamont (1991).

Been and Sills (1981) sketched the development of the internal density structure of the consolidating bed, for example, Figures 37 and 38. They depict the development of the water–sediment interface, and also the development of a lower interface is sketched. Note that this lower interface not necessarily has to occur, as discussed above.

When a space-filling network is formed by the cohesive sediment flocs, the flocs below a certain reference plane have to carry the weight of the sediment above this plane. This implies that the sediment network has to increase in strength. In other words, the weight of sediment above that plane induces a stress within the bed, which expels pore water from the bed – remember the large water content of the flocs. As the stresses within the bed drive almost all processes within that bed, the concept of effective stress has been introduced in soil mechanics: $\sigma_v = u + \sigma'_v$. Here, σ'_v is the total stress (often the hydrostatic pressure as in Figure 39), u is the pore-water pressure; gradients in u induce pore-water flows within the bed; and σ'_v is the so-called effective stress. Note that the effective stress is not identical to the grain–grain stresses. During consolidation, the effective stress increases at the cost of the pore-water stress, for example, Figure 39. As the interface lowers, and the bed density increases at the same time, the total (hydrostatic) stress changes as well during consolidation – for didactic reasons, we have omitted the latter effect in Figure 39.

Figure 40 presents measured density profiles in a consolidation column (Been and Sills, 1981) and stresses within the

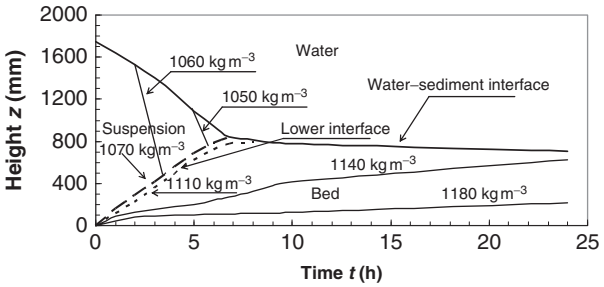

Figure 37 Schematic consolidation diagram. (after Been and Sills, 1981)

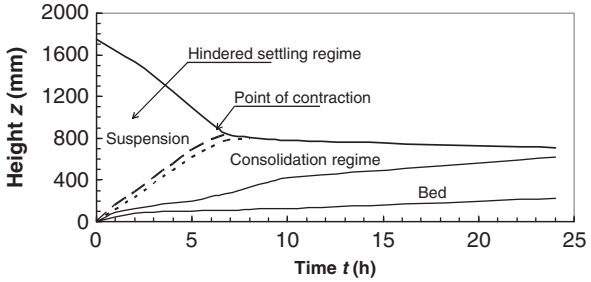

Figure 38 Same as **Figure 37**, with reference to common nomenclature.

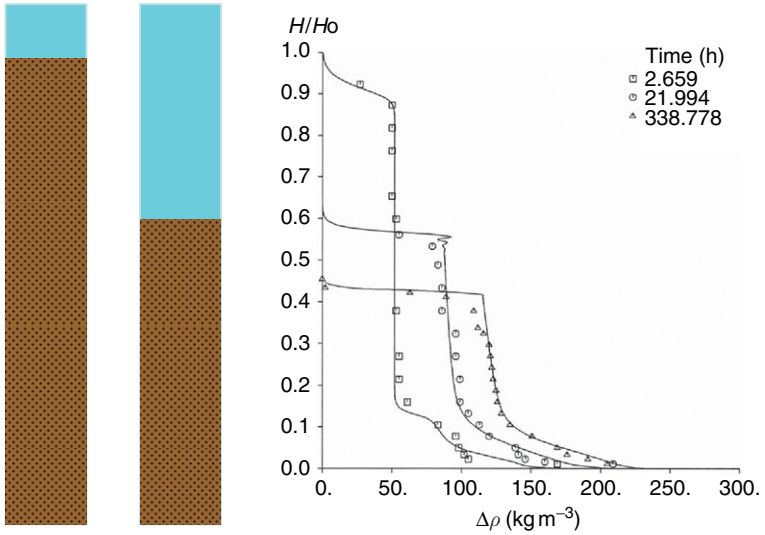

Figure 36 Sketch of consolidating mud–water mixture and measured density distributions. (after Toorman and Berlamont, 1991)

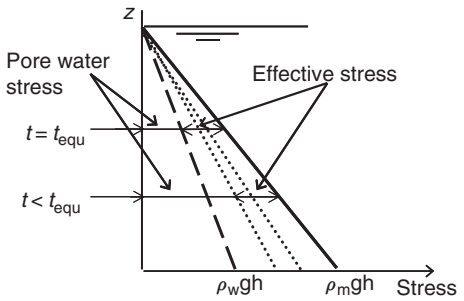

Figure 39 Sketch of effective stress concept.

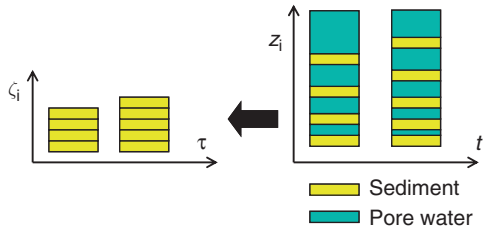

Figure 41 Schematic diagram of introduction of material coordinates.

bed. We have also sketched the equilibrium pore-pressure distribution; at this equilibrium, the sediment is carried by effective stresses only, and consolidation is complete.

The equilibrium pore-water pressure equals the hydrostatic pore-water pressure distribution $\left(=\int_z \rho g \, dz\right)$, where $z = 0$ at the water surface (of course, not at the sediment–water interface). Measuring the pore-water pressure determines the degree of consolidation. Assessing the effective stress requires measuring of the total stress as well.

The Gibson equation (Gibson et al., 1967) yields the classical description of the consolidation process. The vertical mass balance is written in terms of the void ratio e as a function of the sediment's permeability and effective stress. Permeability and effective stress are modeled with a power law or exponential function of the void ratio.

Moreover, the balance equation is rewritten in the so-called material coordinates, a transformation on the basis of the amount of solids at a specific depth in the consolidating sediment, for example, **Figure 41**. The advantage of this approach is that the mathematically/numerically difficult formulation for the interface, basically a step function in material properties (density), is circumvented. A disadvantage of this approach is that (1) it is not easy to account for erosion and/or deposition, so that the advantage of the material coordinates vanishes and (2) it is difficult to account for sediment mixtures (sand–mud mixtures). Therefore, another approach has been developed.

We analyze a (consolidating) soil, sediment–water suspension consisting of water and clay mainly, with some sand and silt particles. The bed structure behaves cohesive (see below), and consolidation is governed by expelling water from between the flocs and from the flocs themselves (see Merckelbach, 2000 for further details). We assume the cohesive sediment network is so strong that the sediment does not segregate, that is, sand grains settle at the same rate as the surrounding mud flocs. The mixture is composed of a clay–water skeleton (carrying the sediments), with sand and silt particles (Section 2.15.5) (**Figure 42**).

Again, we describe the cohesive sediment structure in the bed with a fractal approach, assuming self-similarity at all scales. Note that, contrary to the fractal description of flocs formed in the water column, the fractal dimension is now considerably larger, that is, $n_f = 2.6$–2.8, for example, Kranenburg (1994) and Winterwerp and Van Kesteren (2004). As a consequence, the material functions are given as a function of the solid's volume concentration of the cohesive (mud) fraction and the sand fraction. The basic assumption in this approach is that the pores, which govern permeability, and the contact surfaces between the particles, which govern the strength of the bed, scale with floc size. For further details, the reader is referred to Kranenburg (1994) and Merckelbach (2000):

$$k = K_k \left(\frac{\phi_s^m}{1-\phi_s^{sa}} \right)^{2/3-n_f} \qquad \sigma'_v = \sigma_{zz}^{sk} = K_p \left(\frac{\phi_s^m}{1-\phi_s^{sa}} \right)^{2/3-n_f} \qquad [24]$$

As $n_f \approx 2.6$–2.8, the exponent in the material function attains values between 5 and 10. This implies that the results of consolidation models are highly sensitive to small changes in sand and/or mud content. Note that this is not different in the classical Gibson equation. The coefficients of the material

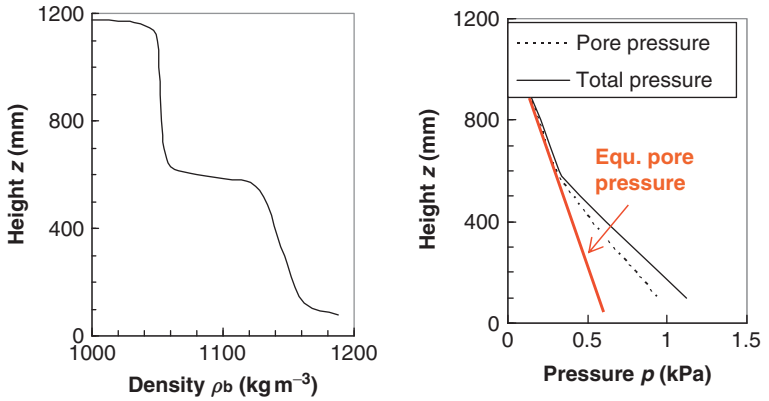

Figure 40 Measured density and stress distribution in a consolidating bed. (after Been and Sills, 1981)

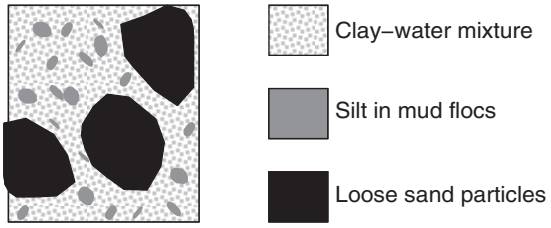

Figure 42 Schematic sediment composition. (from Merckelbach, 2000)

functions typically attain the following values: $K_k = (1 \rightarrow 400) \times 10^{-18}\,\mathrm{m\,s^{-1}}$ and $K_p = (3 \rightarrow 300) \times 10^{12}$ Pa, though other values have been found as well.

Next, we derive the consolidation equation step by step to show the various assumptions made. We assume mud only (one phase, i.e., no sand) in our derivation – the complete derivation is given in Winterwerp and Van Kesteren (2004). We use a Eulerian reference frame and establish the absolute vertical velocity of the solids v_s, of the pore-water fluid v_f, and the relative velocity v_{eff} of the solids with respect to the fluid movements.

The equations of continuity and the vertical mass balance are given in eqns [25] and [26]. In eqns [27] and [28], we introduce the concepts of effective stress and Darcy's law. Note that we derive the consolidation equation for the volumetric concentration of solids, not for the volumetric concentration of the flocs. This approach is chosen, as flocs are poorly defined within a (consolidating) bed. However, through our fractal approach we relate solid concentration to floc size, casu quo pore size:

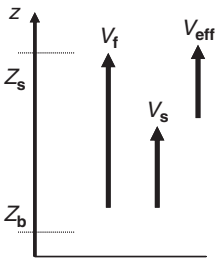

$$(v_f - v_s)\,(1-\phi_s) + v_s = 0 \qquad [25]$$

$$\partial\frac{\phi_s}{\partial t} + \frac{\partial}{\partial z}(v_s\phi_s) = 0 \qquad [26]$$

$$\begin{aligned} p_e &= g\rho_w(z - Z_s)\,\sigma_{zz} \\ &= p^w + \sigma'^{sk}_{zz}(\equiv u + \sigma'_v) \end{aligned} \qquad [27]$$

$$(v_f - v_s)\,(1-\phi_s) = -\frac{k}{g\rho_w}\frac{\partial p_e}{\partial z} \qquad [28]$$

Substitution into eqn [25] yields the vertical solid's velocity in an Eulerian reference frame:

$$v_s = \frac{k}{g\rho_w}\frac{\partial(p^w + gp_w(z - Z_s))}{\partial z} = k + \frac{k}{g\rho_w}\left(\frac{\partial\sigma_{zz}}{\partial z} - \frac{\partial\sigma'^{sk}_{zz}}{\partial z}\right) \qquad [29]$$

or:

$$v_s = \frac{k}{g\rho_w}\frac{\partial(p^w + g\rho_w(z - Z_s))}{\partial z} = k + \frac{k}{g\rho_w}\left(\frac{\partial\sigma_{zz}}{\partial z} - \frac{\partial\sigma'^{sk}_{zz}}{\partial z}\right) \qquad [30]$$

Substitution into the vertical mass balance yields an advection–diffusion equation describing 1D self-weight consolidation of a column of cohesive sediment, for example, eqn [31]. The (constant) diffusion coefficient Γ_c is identical to the consolidation coefficient c_v, well known from soil mechanical theory:

$$\begin{aligned} &\frac{\partial\phi_s^m}{\partial t} - \frac{\partial}{\partial z}\left(\frac{\rho_s - \rho_w}{\rho_w}k\phi_s^m\phi_s^m\right) - \Gamma_c\frac{\partial^2\phi_s^m}{\partial z^2} = 0 \\ &\text{where } \Gamma_c = \frac{2}{3 - n_f}\frac{K_k K_p}{g\rho_w} \end{aligned} \qquad [31]$$

In the initial phase of consolidation, the advective term dominates (i.e., the effects of permeability). In this phase of consolidation, the density profile attains a concave shape. Later, the diffusive term dominates (combining effects of permeability and effective stress), and the density profile attains a convex shape. Based on this second phase, we note that the consolidation time scales with the length scale squared, hence with the square of the thickness of the consolidating sediment layer. Note that this equation is highly nonlinear (in its advective part) as a result of the large exponents in the permeability term (eqn [24]). Again, this is the case not only for the current description but also for all consolidation equations.

We note further that if we omit the second (advection) term in the consolidation equation, we arrive at Terzaghi's (1943) consolidation equation, which is accurate for large consolidation times.

In Winterwerp and Van Kesteren (2004), this consolidation equation is extended to account for the effects of small amounts of sand in the sediment–water mixture. Then we obtain two coupled equations. The consolidation equation for the mud fraction is given here, eqn [32]. It is almost identical to the equation for mud alone, apart from a right-hand-side term. The equation for the sand fraction can be found in Winterwerp and Van Kesteren (2004):

$$\begin{aligned} &\frac{\partial\phi_s^m}{\partial t} - \frac{\partial}{\partial z}\left(\Xi_s^m\phi_s^m\right) - \frac{\partial}{\partial z}\left((D_s + \Gamma_T + \Gamma_c)\frac{\partial\phi_s^m}{\partial z}\right) \\ &\qquad = \frac{\partial}{\partial z}\left(\Gamma_c\frac{\phi_s^m}{1-\phi_s^{sa}}\frac{\partial\phi_s^{sa}}{\partial z}\right) \end{aligned} \qquad [32]$$

We have added the following terms as well by linear superposition:

1. the effects of molecular and turbulent diffusion – these will become very small in the consolidation phase, of course and
2. the effects of hindered settling in the term Ξ_s for the mud fraction, which reads as

$$\begin{aligned} X_s^m &= f_{hs}^m + \frac{f_c}{1 + \eta f_c}, \text{ with} \\ f_{hs}^m &= \frac{\left(1 - \phi^m - \phi_s^{sa}\right)\left(1 - \phi_s^m - \phi_s^{sa}\right)}{1 + 2.5\phi^m}W_{s,r}^m, \text{ and} \\ f_c &= \frac{\rho_s - \rho_w}{\rho_w}k\left(\phi_s^m + \phi_s^{sa}\right) \end{aligned} \qquad [33]$$

where the term with η (~10^3) accounts for a (heuristic) smooth transition between the phases of hindered settling and consolidation (e.g., Winterwerp and Van Kesteren, 2004).

We have implemented the various equations in the 1DV model described before. **Figure 43** shows a comparison of a simulation with this consolidation model and a series of experiments by Merckelbach (2000), showing a fair agreement (Winterwerp and Van Kesteren, 2004).

2.15.5 Bed Properties

In this chapter, we discuss bed properties and how these affect the erosion of the bed. Basically, we follow a soil mechanical approach.

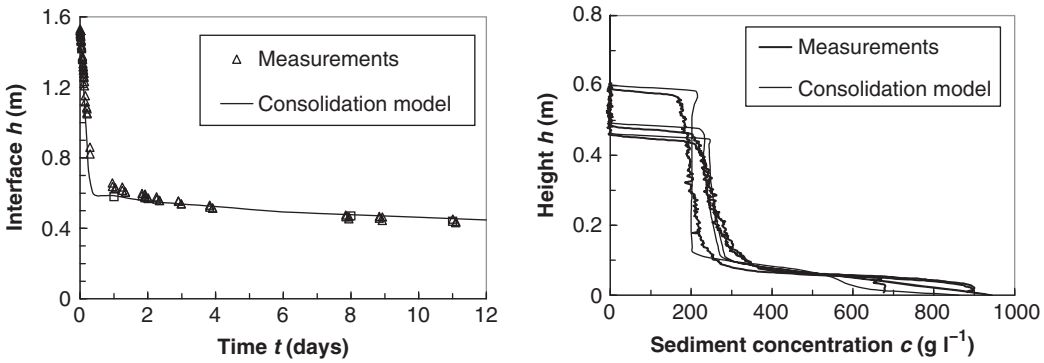

Figure 43 Comparison of measured and computed evolution in sediment–water interface and vertical density profiles.

The buildup of a bed from deposition and the bed properties emerging from this, as discussed in the preceding sections, can be described properly with the hydrodynamic equations commonly used in hydraulic engineering. We have derived extensions of the mass balance to account for hindered settling and consolidation. The mechanical response of the bed to stresses and/or straining can be described with rheological models implemented in the stress tensor of the momentum equation, as long as the bed is not yet too stiff (i.e., as long as the bed can still be described as a kind of fluid), that is, below or around the liquid limit (LL; see below).

When the bed should be treated as a (plastic) soil, that is, its strength is well beyond the LL, we can no longer use our classical hydrodynamic approach, as we have to keep track of the deformations within the bed. This basically requires another approach (soil mechanics), which is beyond the scope of this treatise. Our soil mechanical description of bed erosion as a function of shear stresses, induced by either currents or waves, should therefore be based on parametrization.

As will become clear in the next part of this section, the granular composition of a sediment bed determines to a large extent its soil mechanical behavior. The heuristic triangular sediment diagram of **Figure 44** yields a descriptive qualification of the mineral composition of sediment beds. This diagram is often used by sedimentologists to qualify soils. However, because of its qualitative nature, this diagram is less suitable in a modeling/engineering environment.

We have to realize that the common classification, as discussed previously, is based on particle size, for example, Section 2.15.2: minerals with size smaller than 2 μm are referred to as clays, minerals with size in between 2 and 64 μm are referred to as silt, etc. However, many clay minerals have sizes beyond these values, as shown in **Figure 45**. We will implicitly account for the cohesiveness of particles larger than 2 μm in the approach in the followings.

The minerals kaolinite, illite, montmorillonite, and chlorite are most common in natural soils. Kaolinite is abundant in cohesive sediments encountered in tropical environments, whereas illite is more common in temperate conditions.

Clay minerals are so-called phyllosilicates and consist largely of 2D silica tetrahedra with aluminum-hydroxide octahedra (gibbsite) or magnesium-hydroxide octahedra (brucite). These sheets of silica tetrahedra and gibbsite or brucite can be combined in various ways to form different clay minerals, for example, **Figure 46**.

Apart from their large specific surface, clay particles have an uneven electrical charge distribution; the clay faces are generally negatively charged. As a result, the behavior of clay particles is largely affected by the chemistry of the pore water (pH and dissolved salts; **Figure 28**). Clay particles can attract each other through van der Waals forces, and repulse each other through electrostatic forces. We will not elaborate on this in this chapter, but more information can be found in, for example, Verwey and Overbeek (1948) and Mitchell (1976). Winterwerp and Van Kesteren (2004) presented a brief summary of the relevant clay properties.

Flocculation is largely affected by the presence of organic material, which often is referred to as EPSs (mainly polysaccharides), although some other substances are important as well. These substances are secreted by microphytobenthos (algae) and bacteria.

There exists large literature on the effects of biology (organic matter) on the behavior of cohesive sediment. A concise summary from a modeling point of view is given by Le Hir et al. (2007).

Organic material attains its properties from organic polymers, for example, **Figure 47**.

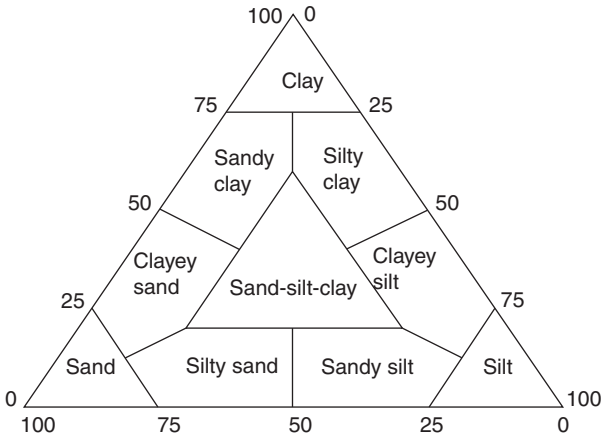

Figure 44 Heuristic sediment classification diagram used in sedimentology (Flemming, 2000).

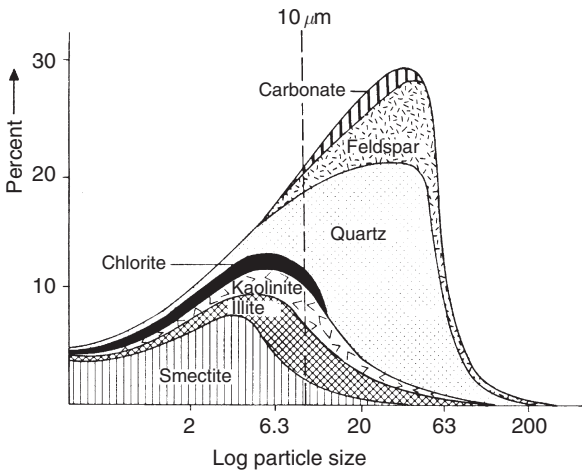

Figure 45 Mineralogical distribution of Mississippi sediment (Weaver, 1989).

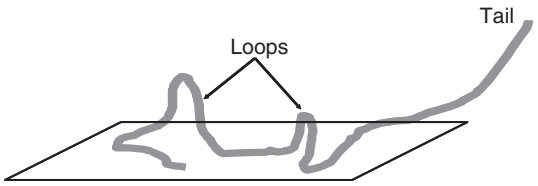

Figure 47 Sketch of polymer adhering to a clay particle.

These organic polymers are active because of van der Waals forces, bipolar forces, and/or hydrogen bonding (bipolarity). The main organic substances exist of hybrocarbons (cellulose), lipids, lignin; polysaccharides and proteins, which are flocculants; and humic acids that are deflocculants.

Bipolar forces are much stronger than the van der Waals forces and are quite effective, as the polymer–clay particle interaction is not affected by electrostatic repulsion because the polymer is overall electrically neutral.

The photographs in **Figures 48** and **12** clearly show an abundance of organic filaments – in particular, the left photograph of **Figure 12** shows a very open structure. Such flocs are typical for freshwater environments (lakes!) with large fractions of organic material. In estuaries and coastal zones, flocs are often more dense because of the large stresses occurring.

However, on a large timescale, that is, interannual, variations are often largely governed by the mineral components of the bed, in conjunction with large stresses during wintertime (waves and currents). We therefore seek to parametrize biological effects through coefficients and/or additional terms in our physical models of bed behavior.

Next to the large influence of biota on the physical/mechanical behavior of the bed, also the chemistry may play an important role. **Figure 49** depicts typical gradients of a series of chemical parameters in the upper part of the bed (after Fenchel and Riedl (1970)). These gradients are formed in a thin layer as a result of degradation of organic material, and the availability of oxygen. The thickness of this layer amounts to a few millimeters to a few centimeters, depending on the local grain size distribution and the effects of bed-disturbing organisms (bioturbation).

In an oxygenated environment Fe^{3+} is formed, which can form precipitates of Fe_2O_3 (rust), $Fe(OH)_3$ (bog-ore), and/or various forms of FeOOH. These Fe^{3+} compounds are expected to increase bed strength. In a reducing environment, Fe^{3+} reduces to Fe^{2+}, and bed strength is expected to decrease. This may imply softer sediments below a thin, cemented crust. The redox potential E_h yields a measure of the state of reduction of the organic material.

Next, we introduce a number of bulk parameters, as defined and commonly used in soil mechanics. These parameters are easily measured, and implicitly account for physical, chemical, and biological effects on the mechanical behavior of the sediment. Although they are highly heuristic, an enormous database has been built up over many decades, yielding fairly robust relations between these bulk parameters and primary mechanical parameters of the soil.

The so-called Atterberg limits depict the water content W (mass of water/mass of solids) at which the mixture behaves as

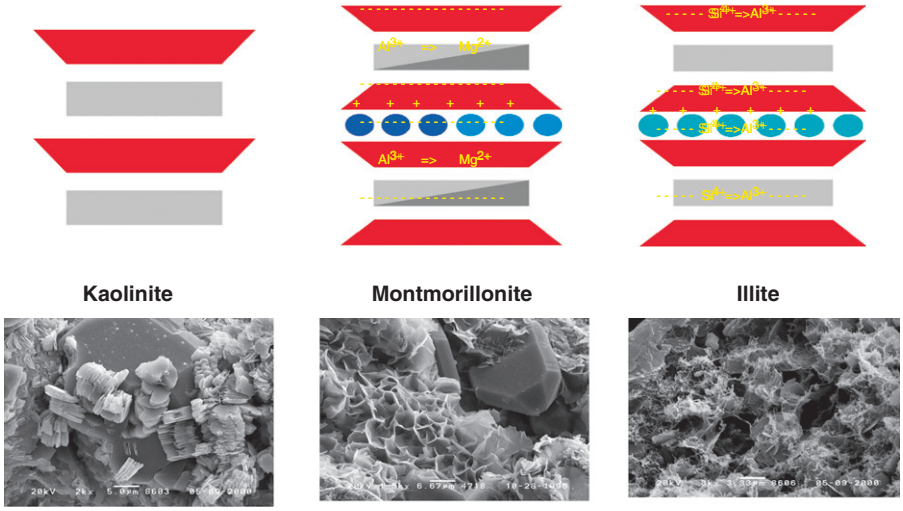

Figure 46 Photographs of clay minerals and sketches of their filamentous structure.

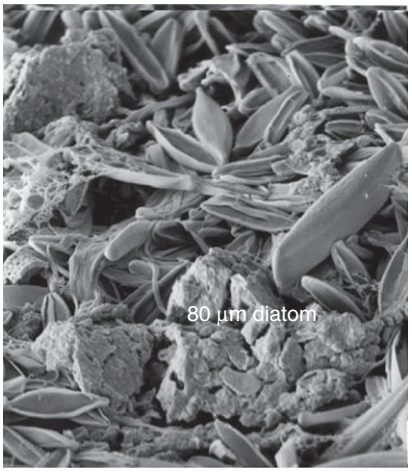

Figure 48 Photograph of sediment surface on mudflat. (after Paterson, 1997)

a fluid or as a soil. Below the LL the sediment–water mixture behaves as a fluid, whereas at higher sediment concentrations non-Newtonian effects become important. Beyond the plastic limit (PL), the sediment–water mixture has to be considered as a soil. In between, the mixture has plastic features, may become fluid when remolded (breaking of interparticle bonds), and is modeled as a thixotropic material. The undrained strength c_u at the LL amounts to about 1–2 kPa, whereas at the PL, $c_u \approx 100$–200 kPa. If the clays in the sediment–water mixture can bind much water, as is the case with smectites, the PL is achieved at fairly low bulk density. For more information, the reader is referred to Lambe and Whitman (1979) (see also **Figure 50**).

Further, we define the plasticity index PI = LL – PL, and the liquidity index LI = (W – PL)/PI, which reflect the actual state of the soil.

Figure 51 shows the so-called plasticity plot. Variations in LL are obtained by variation of the amount of sand to a sediment–water mixture, affecting the plasticity of the mixture. For soils with limited organic content, a fairly unique relation exists between PI and LL, that is, the PI increases more or less proportional to the LL.

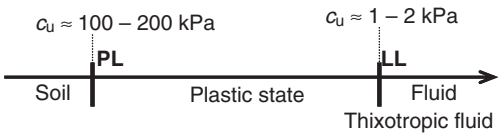

Figure 50 Atterberg limits, relevant for cohesive sediment beds.

A very practical relation is the so-called activity plot, which gives the PI (= PL – LL) as a function of the clay content ξ^{cl} (<2 µm) (**Figure 52**). The slope of this relation yields the activity A, which is unique for a specific clay (mixture). The activity plot provides a simple means to determine ξ_0, the clay content beyond which the mixture exhibits cohesive properties, because ξ_0 is given by the intercept with the ξ^{cl} axis (more accurately, when PI ≈ 7%). This value will be used later in the setup of a sediment stability diagram.

The undrained shear strength c_u is a material property, that is, a mechanical property of the sediment mixture. It can be determined with a vane shear test, and is characterized by the shoulder in the stress–strain curve (see diagram of **Figure 53**). Note that the peak strength is not a material property, as it is dependent on the acceleration of the vane: at small acceleration, the bonds between the flocs can survive longer, drainage may occur, and the peak strength would increase. c_u, on the contrary, is basically independent of the experimental procedure. Note that we expect $\tau_y < c_u < \tau_B$, where τ_B is the Bingham strength of the material.

The large experience on the relation between mechanical properties and Atterberg limits yields a series of useful relations. **Figure 54** shows a fairly unique relation between the undrained shear strength and the Atteberg limits (LI), even though the spread among the data is large.

This graph shows that at the LL, c_u amounts to a few kPa, and at the PL c_u is about 100 kPa.

Figure 55 shows also a fairly unique relation between the relative permeability of the soil (k/ϕ_s), though the spread is even larger (note the axis' log scale) than for c_u. In a consolidating bed, ϕ_s typically amounts to ~0.1. This implies that k attains values of 10^{-9}–10^{-11} m s^{-1}. This implies that only very slow processes induce a drained response in cohesive sediment beds

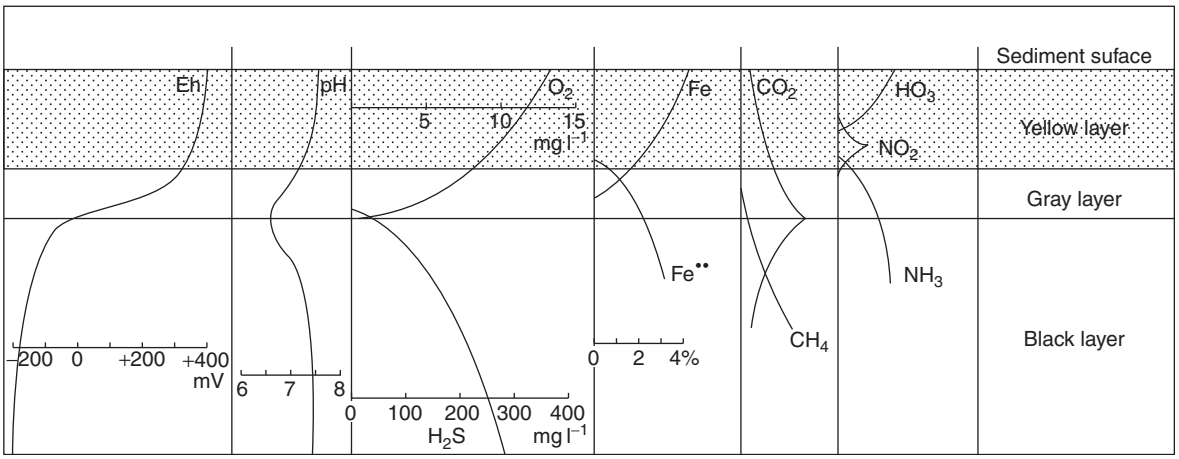

Figure 49 Characteristic profiles of various chemical parameters in the upper part of the bed. (after Fenchel and Riedl, 1970)

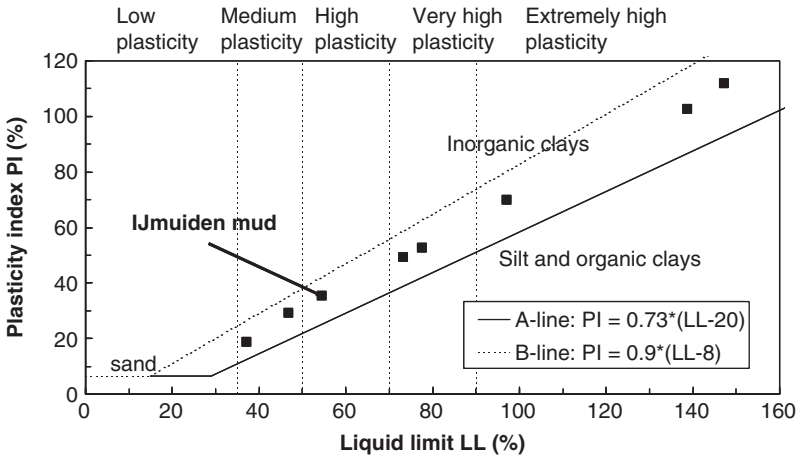

Figure 51 Plasticity plot for sediments with little organic material ($\xi^{org} < 15\%$) and data from IJmuiden, the Netherlands. (from Head, 1986)

(see later): cohesive beds typically depict undrained behavior when deformed.

Another very useful relationship is based on the relative water content, that is, water content normalized with the PI, showing an almost perfect exponential relation with undrained shear strength, for example, **Figure 56**.

The diagrams of **Figures 51–57** show the use of the Atterberg limits in establishing a number of mechanical properties of cohesive sediment beds. Moreover, these explicit relations allow for incorporation in numerical models, enabling assessment of the erosion behavior of these beds, for example, Section 2.15.6 of this chapter.

Next, we classify soil occurrences in nature, determining the mechanical response to external stresses, in particular with respect to erosion.

Sand particles and solid (e.g., strong) flocs can build a skeleton when closely packed. This is sketched in **Figure 57**, showing a most dense packing for spherical particles, a looser packing when the particles just touch each other, and an arrangement where particles are not in contact with each other.

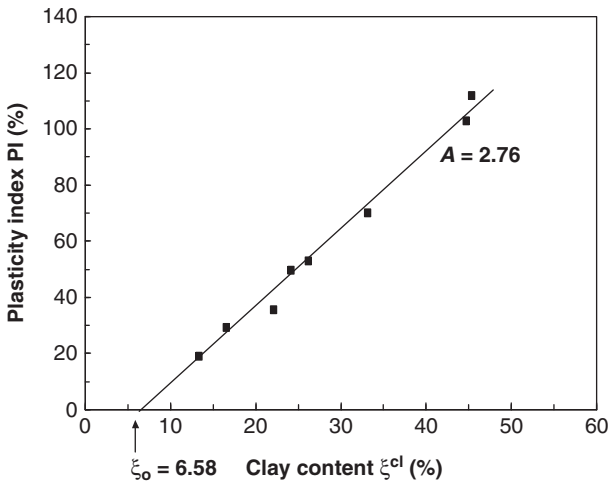

Figure 52 Activity plot for IJmuiden mud; the activity plot includes the effect of organic matter, e.g., organic polymers. (after Winterwerp and Van Kesteren, 2004)

In the first case, mutual particle distances have to increase upon deformation (unless the particles themselves break), as a result of which porosity increases: the soil shows dilatancy – in soil mechanics, this response is referred to as softening. In the second case, deformations may lead to the so-called hardening (porosity decreases). Theoretically, deformations can occur without volume changes – the latter is the critical state referred to further in this section. In the range of $25.6\% < n < 47.6\%$, the spheres still make mutual contact, and a skeleton can exist with a certain strength.

The last state, that is, no granular skeleton, can only occur if the spaces in between the particles ($n > 47.6\%$) are filled with another medium (discussed later in the chapter).

An important parameter determining the response of a soil is the flow of pore water. Upon deformations of the soil, pore-water pressure gradients are induced. If pore water can flow fast enough to compensate these gradients, the soil response is referred to as drained. If this is not the case, pore-water over- and underpressures are maintained for some time, and the soil response is referred to as undrained. This drained/undrained response is measured with the Péclet (or Froude) number, which is the ratio between the rate of deformation and the permeability of the soil. At large Péclet numbers, that is, undrained soil response, deformations result in an apparent cohesion of the soil. For cohesive soils, permeability is so low that the soil response to deformations is

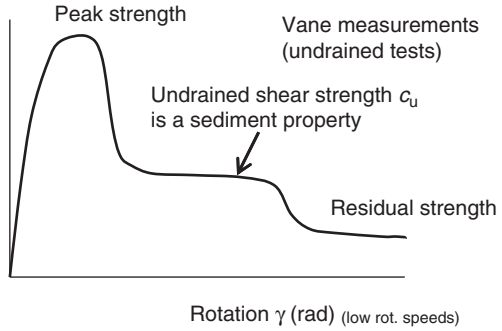

Figure 53 Sketch of stress–strain curve in response to a shear vane measurement.

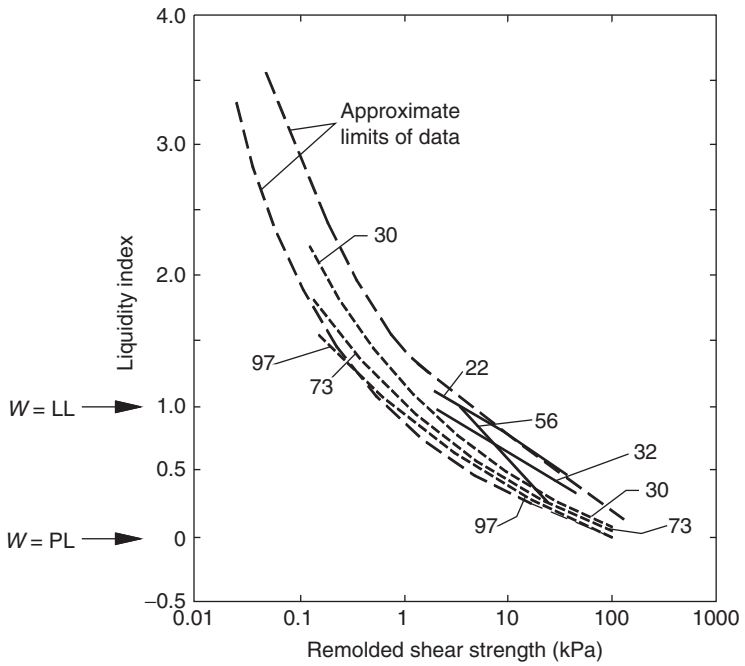

Figure 54 Undrained shear strength as function of LI. (after Mitchel, 1976)

undrained in general, unless deformation rates are very slow. For more information, the reader is referred to Van Ledden et al. (2004) and Winterwerp and Van Kesteren (2004).

However, soils do not exist of spherical, monodispersed particles; the critical porosity depicted in **Figure 57** is therefore not realistic for real soils. **Figure 58** shows minimum and maximum porosities for soils with a sand or with a silt skeleton. Soils with a silt skeleton are rare; sediments in the Yellow River may fall within this category. Best known are mixtures with a noncohesive sand-dominated skeleton, as often found along the shores of wave-dominated coasts, and cohesive beds with a clay skeleton, as encountered in many muddy areas. Also, other phases exist, as explained below.

We have now collected all information to quantify the heuristic diagram of **Figure 44**, the result of which is given in **Figure 59** (Van Ledden et al., 2004). From activity plots, such as **Figure 52**, the onset of cohesion can be determined. We have set this onset at 6% in **Figure 59**. **Figure 58** yields values for the critical porosity beyond which the soil is characterized by a sand or silt skeleton. In **Figure 59**, we have drawn a few demarcation lines; in our discussion we presume network formation at 40% porosity.

In **Figure 59** we distinguish six different soil behaviors, as indicated. For $\xi^{cl} < \xi_0$, the soil behaves as a granular material with a sand or a silt skeleton, and cohesive forces are zero. Note domain 3, noncohesive without granular skeleton – soils within this domain are highly unstable, and sensitive to

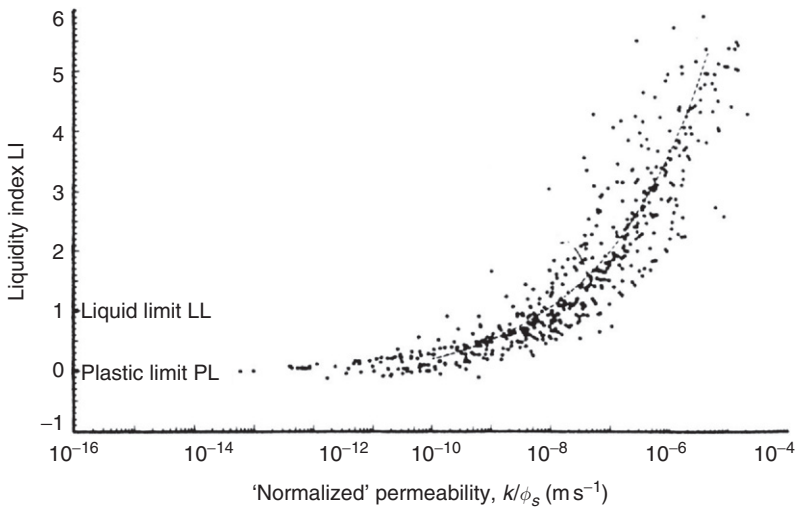

Figure 55 Relative permeability as a function of liquidity index (see Winterwerp and Van Kesteren, 2004).

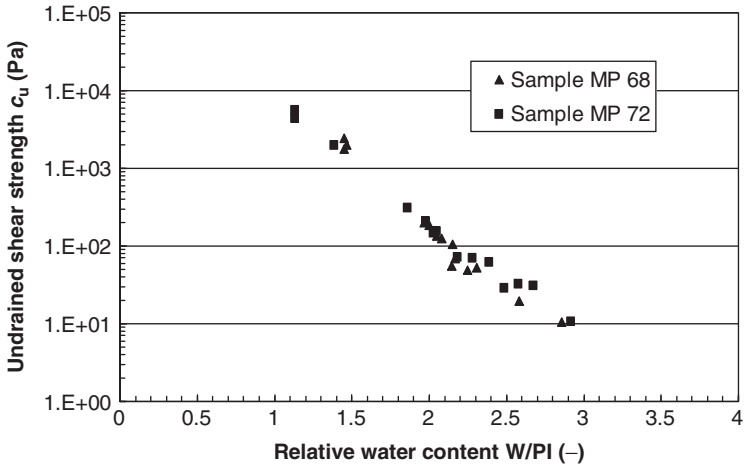

Figure 56 Undrained shear strength as a function of relative water content for IJmuiden sediments (see Winterwerp and Van Kesteren, 2004).

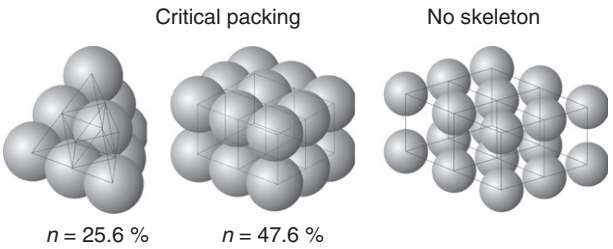

Figure 57 Cartoon of network structures (skeleton) in granular material.

failure/liquefaction. For $\xi^{cl} > \xi_0$, the soil exhibits cohesive response, though granular skeletons are also possible.

In Figure 60 we have also plotted the sediment composition of numerous bed samples from the Western Scheldt (the Netherlands). Although there is some spread in the data, they more or less collapse along one line, indicating a constant ratio of silt and clay content (4:1, in this case). Such a constant ratio was found for sediments from coastal areas and estuaries throughout the world (e.g., Flemming, 2000), but the value itself varies (in the upper part of the Scheldt estuary, the so-called Sea Scheldt, this ratio decreases to 3:1). The constancy of this ratio is very convenient, as then we only need to determine the sand content of a sample to distinguish its mechanical behavior. The sand content of a sediment mixture can be determined quite easily, contrary to the clay content, as discussed in the beginning of this chapter.

Next to the constant ratio between silt and clay content, it is also possible to derive an empirical relation between the dry bed density of a (cohesive) soil and its age, that is, its degree of consolidation. Allersma (1988) developed the empirical relation [34], in which α_c a consolidation coefficient, ranging from $\alpha_c = 0$ for fresh deposits to $\alpha_c = 2.4$ for old deposits, resulting, respectively, in a lower and upper bound for the dry density:

$$\rho_{dry} = 480\alpha_c + (1300 - 280\alpha_c)\xi^{sa0.8} \qquad [34]$$

where ξ^{sa} is the sand content of the soil. With these empirical observations, we can reconstruct the sediment triangle into a more handy diagram, applicable in engineering studies, for example, Figure 60.

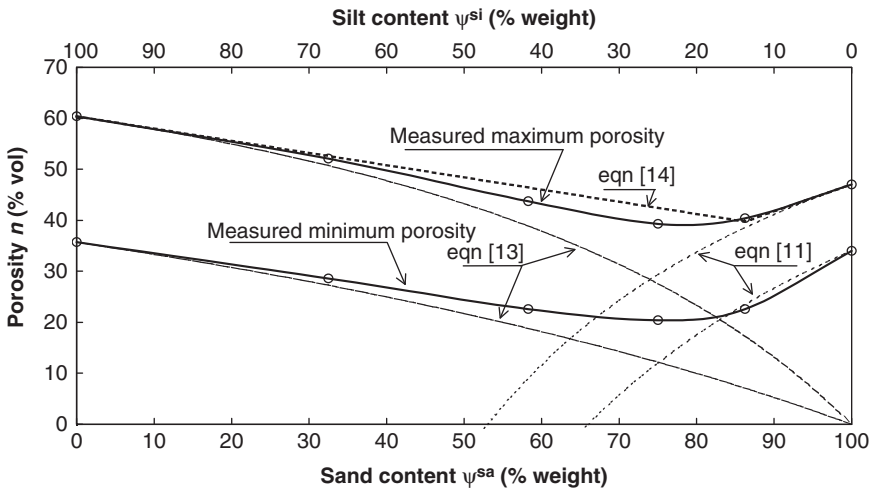

Figure 58 Minimum and maximum porosity for granular sand–silt mixtures (see Winterwerp and Van Kesteren, 2004).

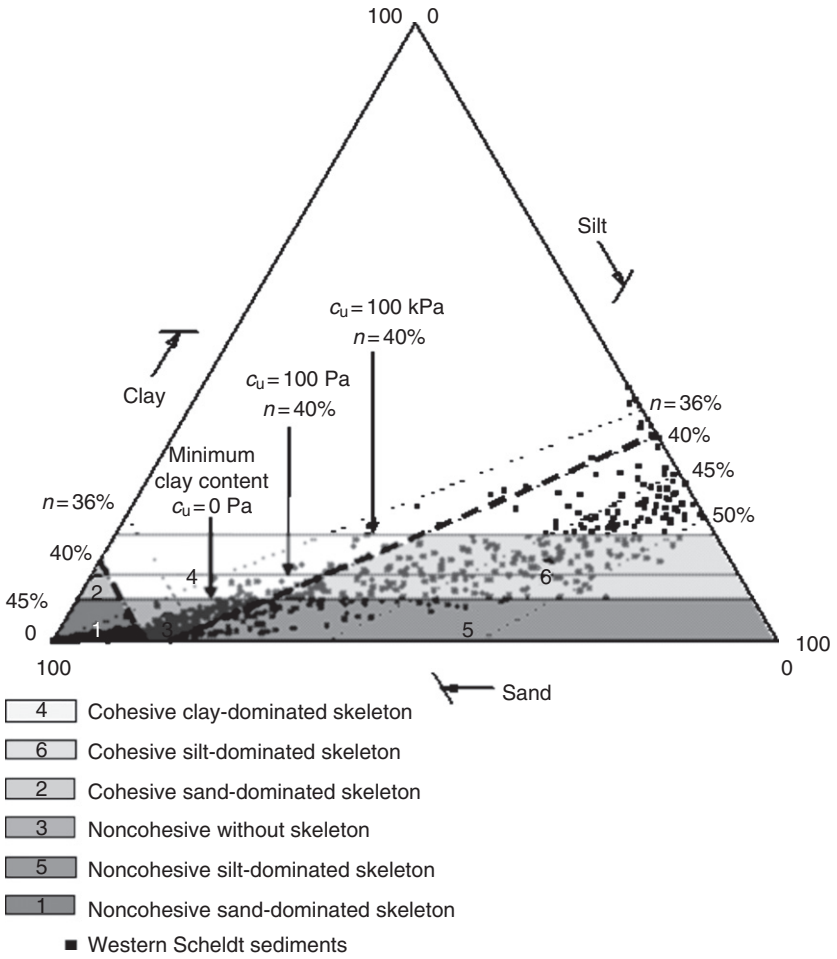

Figure 59 Quantified sand–silt–clay triangle (see Van Ledden, et al., 2004; Winterwerp and Van Kesteren, 2004).

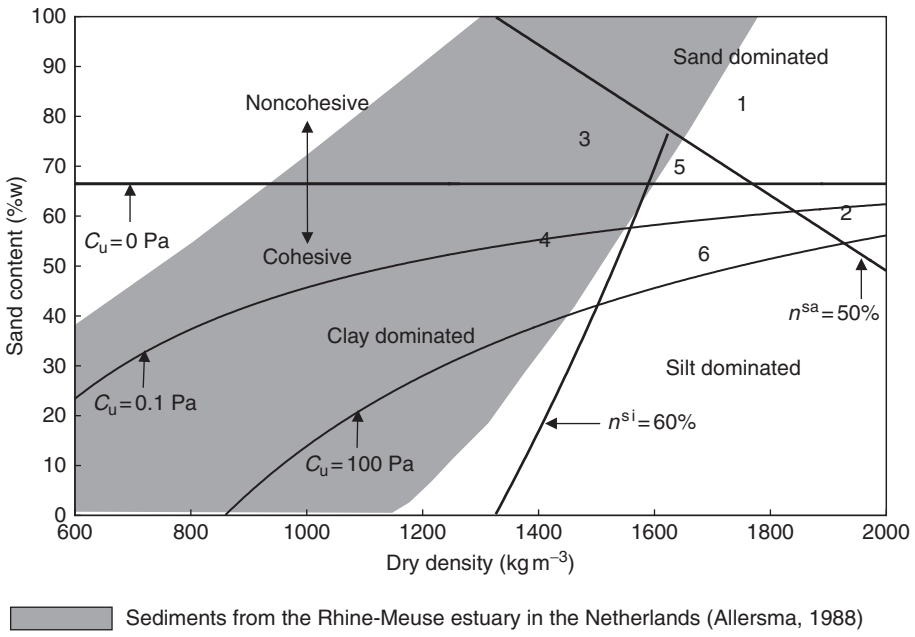

Figure 60 Sediment phase diagram for Western Scheldt sediments, the Netherlands (e.g., Winterwerp and Van Kesteren, 2004).

Figure 60 is referred to as a sediment phase diagram, and this has been erected for Western Scheldt conditions, as an example. We have added a gray band, determined by Allersma's relation, indicating the density–sand combinations expected in the Western Scheldt (natural occurring conditions). On the basis of sand content and dry bed density (solids concentration within the bed), we can construct this phase diagram, in which we can plot data of actual samples. The numbers within this phase diagram correspond to the numbers in Figure 59, indicating expected mechanical behavior.

The dry bed density is directly related to the water content within the bed, from which we can assess the strength of the bed from the c_u – LI plot (Figure 54).

Basically, this diagram can be used directly in numerical sediment-transport models, accounting for at least the sand and mud fractions, and a consolidation module. This would yield strength distributions (and also permeability – see relation k/ϕ_s – LI, Figure 55), which can be used in erosion formulas (Section 2.15.6).

2.15.6 Erosion

Let us analyze the stresses by turbulent flow on a sediment bed at location x_1,y_1. Generally, the strength of a bed varies spatially, in horizontal direction x,y, and also over the depth, z. This horizontal strength variation is depicted by a (Gaussian) probability density function, for example, Figure 61. We represent the bed strength through the critical bed strength for erosion τ_{cr}, a threshold stress value beyond which erosion is possible. Later in this section, we discuss the relation between τ_{cr} and some soil mechanical parameters of the bed. At the location x_1,y_1, the relevant strength of the bed amounts to $\tau_{cr}(x_1,y_1)$. We note that if the τ_{cr} distribution is very wide (variance in τ_{cr} is large), it will be very difficult to predict erosion rates in the real world.

The instantaneous bed shear stress, induced by turbulent flow, varies over space and time. In Figure 61 we also sketch the probability density distribution of the bed shear stress $\tau_b(x_1,y_1,t)$. In this example, the mean (median) bed shear stress $\overline{\tau}_b$ is smaller than the critical bed strength for erosion τ_{cr} at that location. However, during part of the time, $\tau_b > \tau_{cr}(x_1,y_1)$, and flocs are disrupted from the bed surface, as shown in Figure 61. We refer to this condition as floc erosion.

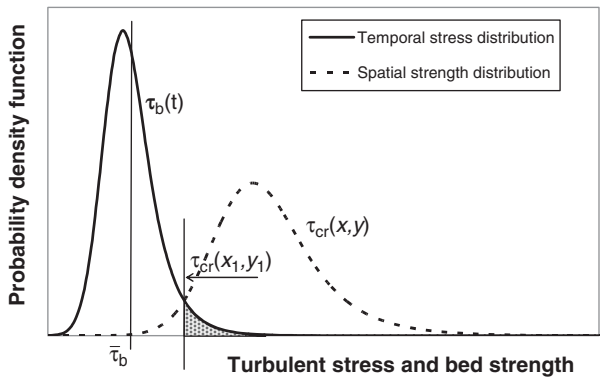

Figure 61 Sketch of spatial distribution in critical shear stress and temporal distribution in bed shear stress at the location x_1,y_1. The shaded area depicts the distribution of erosion events, tearing flocs from the bed, that is, the conditions for floc erosion.

When the flow velocity increases further, surface erosion may occur. In this case, sediment is disrupted from the bed at a rate such that the state of consolidation of the bed can respond to changes in stress levels – of course, floc erosion continues, but is too small to be of significance, and can therefore be ignored.

As it is convenient to quantify the rate of surface erosion with respect to the mean bed shear $\overline{\tau}_b$, we elaborate the shear stress distribution in the followings.

Further to Hofland and Battjes (2006), Van Prooijen and Winterwerp (2010) proposed a formulation for the probability density function $p(T)$ for the turbulent bed shear stress. In this approach, it is assumed that the near-bed velocity is Gaussian and the bed shear stress scales quadratic with the near-bed velocity: $T = \tau_b/\rho_w\sigma_u^2$, where τ_b is the instantaneous flow-induced bed shear stress, ρ_w is the water density, σ_u is a measure for the standard deviation of the shear velocity distribution $u_*^2 = \mu_u^2 + \sigma_u^2$, and μ_u is a measure for the mean value of the shear velocity. For reasons explained by Van Prooijen and Winterwerp (2010), a second parameter is introduced: $T^* = \alpha T - \beta\delta^2$, in which α and β are coefficients to be obtained from calibration, and $\delta = \mu_u/\sigma_u$. Calibration against experimental data by Obi et al. (1996) yields the following values for the three parameters: $\alpha = 1.75$, $\beta = 0.83$, and $\delta = 3.1$, for example, Figure 62.

Next, we elaborate the linear erosions formulation, often referred to as the erosion formula by Partheniades, given in eqn [35]:

$$E = M(\overline{\tau}_b - \tau_c) \text{ for } \overline{\tau}_b > \tau_c \qquad [35]$$

(Note that from a dimensional point of view, the common formulation $E = M(\overline{\tau}_b - \tau_{cr})/\tau_{cr}$ is more attractive. However, assessment of the model parameters from experimental data close to the onset of erosion can be done more accurately with the form proposed in eqn [35], where E is the erosion rate (kg m^{-2} s^{-1}), M an erosion parameter (s m^{-1}), and τ_c the critical shear stress for erosion, discussed above, and elaborated in the following pages. The actual bed shear stress $\overline{\tau}_b$ is the mean bed shear stress, that is, the value used in numerical models and analyses of laboratory data. Substitution of the pdf-distribution of bed shear stress into eqn [35] yields a stochastic erosion formula, which is given in Van Prooijen and Winterwerp (2010). A more practical form, obtained from parametrization is given in eqn [36]. The complete erosion formulation, its parametrization, and eqn [35] are plotted in Figure 63. The linear part of that curve, for example, eqn [35] represents surface erosion, as elaborated below, whereas the curved part at small stresses represents floc erosion rates:

$$\frac{E}{M\tau_{cr}} = \begin{cases} 0 & \text{for } \dfrac{\overline{\tau}_b}{\tau_{cr}} < 0.52 \\ \alpha_1\left(\dfrac{\overline{\tau}_b}{\tau_{cr}}\right)^3 + \alpha_2\left(\dfrac{\overline{\tau}_b}{\tau_{cr}}\right)^2 + \alpha_3\left(\dfrac{\overline{\tau}_b}{\tau_{cr}}\right) + \alpha_4 & \\ \dfrac{\overline{\tau}_b}{\tau_{cr}} - 1 & \text{for } \dfrac{\overline{\tau}_b}{\tau_{cr}} > 1.7 \end{cases} \qquad [36]$$

in which the following parameters have been found: $a_1 = -0.144$; $a_2 = 0.904$; $a_3 = -0.823$; $a_4 = 0.204$ (e.g., Van Prooijen and Winterwerp, 2010). Figure 63 suggests that

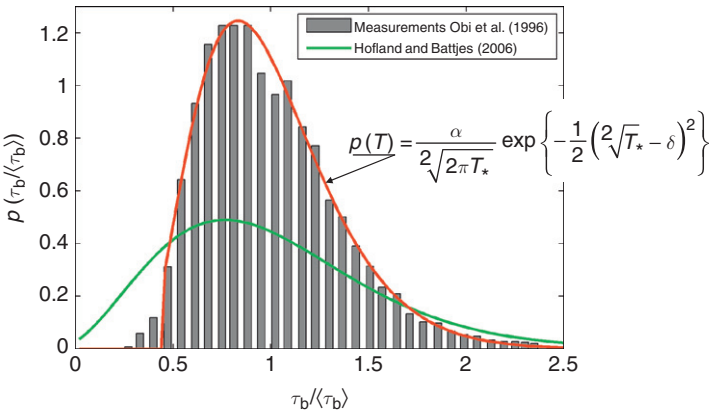

Figure 62 Shear stress distribution $p(T)$ compared with observations by Obi et al. (1996) and the distribution proposed earlier by Hofland and Battjes (2006).

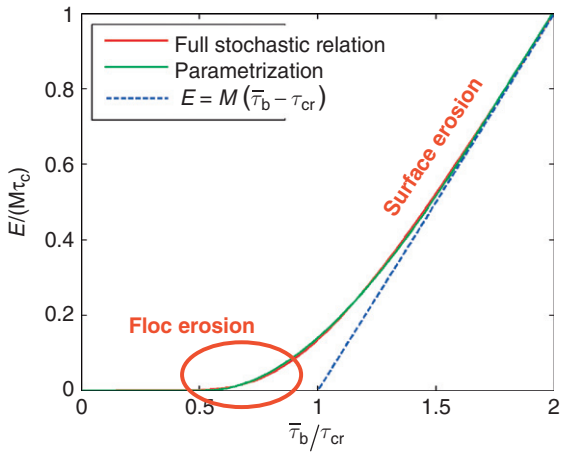

Figure 63 Diagram showing the transition from floc erosion toward surface erosion with increasing bed shear stress. This transition is given by the stochastic erosion formulation and its parametrization; the rate of surface erosion is depicted by the linear part of the diagram (eqn [35]).

considerable amounts of sediment may be eroded when $\overline{\tau}_b < \tau_{cr}$, Moreover, the erosion rate is also much larger around $\overline{\tau}_b \approx \tau_{cr}$ than the linear (surface) erosion formula suggests.

The stochastic erosion model is completed with a layered bed model, consisting of a thin active layer (with thickness Δ, amounting to several 10 μm) on top of a substrate (buffer layer), which can be further divided into sublayers. We assume an initially normal distribution of the strength of the bed (critical shear strength of erosion):

$$r(\tau_{cr}) = \frac{1}{\sigma_{\tau,cr}\sqrt{2\pi}} \exp\left\{-\frac{(\tau_{cr} - \mu_{\tau,cr})^2}{2\sigma_{\tau,cr}^2}\right\} \qquad [37]$$

in which $\mu_{\tau,cr}$ is the mean value of strength distribution and $\sigma_{\tau,cr}$ is its standard deviation. Basically, these strength parameters have to be obtained through calibration, or should follow from soil mechanical analyses, using bulk soil parameters (see later in the chapter). For the time being, the erosion coefficient M is taken constant. The weaker fractions of the sediment bed erode when the bed shear stress exceeds a threshold, and armoring occurs, for example, Van Prooijen and Winterwerp (2010). We can extend this bed model and/or its interpretation by including a vertical gradient in parameters, accounting for the effects of consolidation, or a horizontal distribution, accounting for spatial inhomogeneities.

The stochastic bed description eqn [37] in conjunction with [36] is compared with laboratory and field observations. **Figure 64** shows a comparison of this stochastic erosion model and data collected in an annular flume by Jacobs (2011). The sediment bed consisted of an artificial mixture of 16% clay, 64% silt, and 20% fine sand, at a density of about 1800 kg m^{-3}. The bed was eroded in consecutive steps of 10 min each; at the end of the experiments, 0.75 mm of sediment was eroded from the bed. After calibration, the following values for the model were found: $\Delta = 50$ μm, $M = 0.036$ s m^{-1}, $\mu_{\tau,cr} = 2.4$ Pa, $\sigma_{\tau,cr} = 7.8$ Pa.

Although the model results have been obtained by careful tuning of the model coefficients, it is remarkable that model and observations agree over the entire experimental range. Moreover, we observe a transition from the so-called type II erosion (constant erosion rate in time) to type I (decreasing erosion rate as a result of stratification, e.g., armoring).

Next, the model is calibrated against and compared with the data set obtained by Amos et al. (1992) with a Sea Carrousel operated in the Bay of Fundy. The following coefficients were found: $\Delta = 32$ μm, $M = 0.020$ s m^{-1}, $\mu_{\tau,cr} = 2.35$ Pa, $\sigma_{\tau,cr} = 7.7$ Pa. (Note that the parameter settings obtained from fitting against experimental data are rather sensitive to the bed friction coefficient; for further details the reader is referred to Van Prooijen and Winterwerp (2010).) **Figure 65** shows the applied stresses (flow velocities) and the erosion rate. With these parameter settings, we find a favorable comparison with experiments, again with a transition from type II to type I erosion during the erosion process.

The following describes surface erosion as a soil mechanical process, that is, failure of the bed induced by external stresses. This description continues on the erosion model developed by Van Kesteren, presented for the first time in Winterwerp and Van Kesteren (2004).

The yield of mud samples is often assessed from roto-viscometer measurements (e.g., **Figure 66(a)**); the best

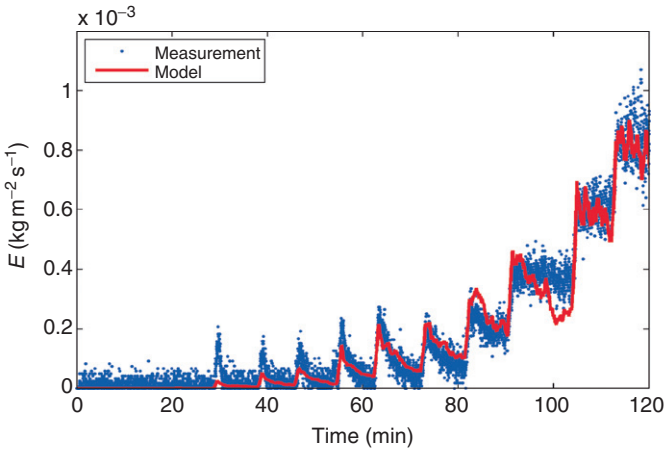

Figure 64 Comparison of stochastic erosion model with observations by Jacobs (2011); the erosion rate varies with time, following 10-min steps in the bed shear stress.

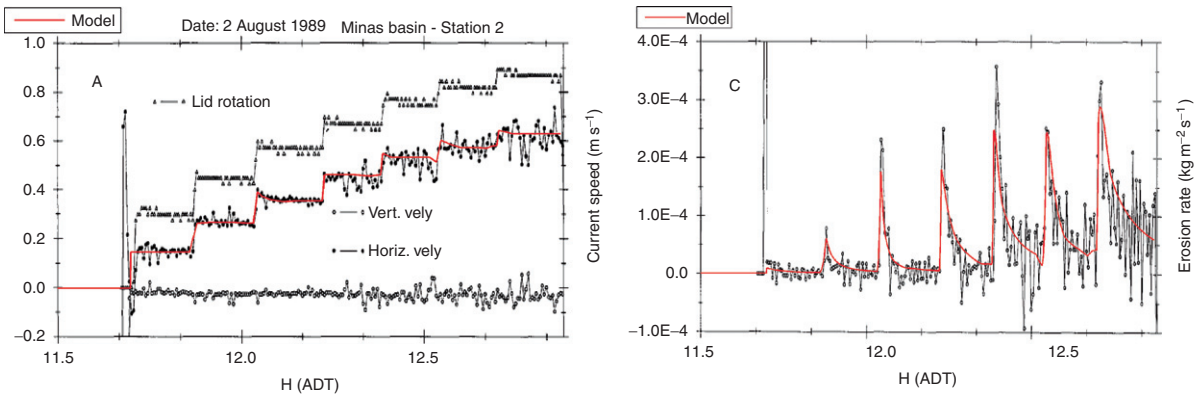

Figure 65 Comparison of stochastic erosion model with observations by Amos et al. (1992); the erosion rate varies with time (right), following 10-min steps in the bed shear stress (left).

results are obtained with the so-called stress-controlled rheometers. However, even in that case the yield strength τ_y is poorly defined and a function of experimental procedures (e.g., acceleration of the cylinder and slip at the wall). More sophisticated experimental procedures with the roto-viscometer (i.e., particular oscillatory forcing) are deployed as well to obtain other properties of the material, assessing its elasticity and loss moduli.

Therefore, we promote the use of simple shear vane measurements, obtaining the remolded shear strength, which equals the undrained shear strength c_u if the shear vane tests are carried out fast enough. This is a material parameter,

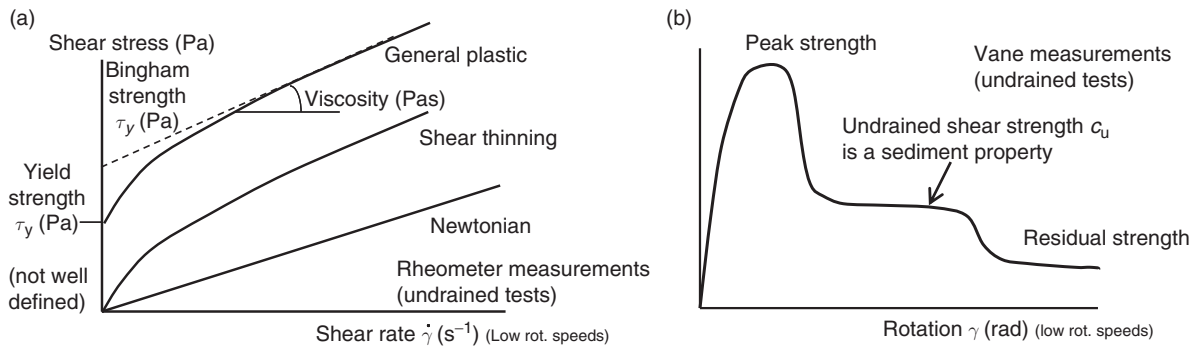

Figure 66 (**a**) Typical flow curves from roto-viscometer measurements – the yield strength τ_y is affected by the experimental procedure, and is not well defined. (**b**) Typical stress curve from shear vane measurements – the undrained shear strength c_u is a material parameter and well defined; generally $\tau_y < c_u < \tau_B$.

independent of the experimental procedure. However, the test should be carried out fast enough to prevent dissipation of the water overpressure or under pressures (i.e., undrained conditions).

Contrarily, the peak strength is a function of the experimental procedure, affected by the geometry of the deformations in the sample, pore-pressure generation, and/or breakup of the sediment flocs.

The drained shear strength c_d is smaller than c_u by orders of magnitude, and is related to the true cohesion of the cohesive sediment, and to the critical shear strength for erosion, as explained below.

We need some simple soil mechanical theories to understand and quantify true cohesion.

We start with Mohr's circle, which is a graphical representation of the stresses on arbitrary planes within the bed. For simplicity, we discuss the stresses in one plane only. Figure 67 presents an example of the stress combinations on planes at various angles in the soil in a shear stress – normal stress diagram, the so-called Mohr diagram. For more background, the reader is referred to one of the many textbooks on soil mechanics, for instance, Lambe and Whitman (1979).

If we would increase the shear on the soil until failure, we can construct the Mohr circle at failure. This can be done at various values of the isotropic stress, obtaining a family of Mohr circles at failure. The envelope of these Mohr circles forms the so-called Mohr–Coulomb failure envelope. Stress combinations beyond this envelope yield unstable conditions: the soil fails. These circles at failure and the Mohr–Coulomb envelope can be established from triaxial tests (e.g., Lambe and Whitman, 1979). Figure 68 presents a sketch of such triaxial tests and the stress diagram with the circles and envelope of failure. As these tests are carried out on untreated samples, the results include the effect of organic matter.

For cohesive sediments, we find a residual shear strength τ_θ at zero normal stress σ_θ, the so-called true cohesion c of the sediment, that is, the drained shear strength c_d. The Mohr–Coulomb failure envelope is often convex toward the σ-axis. For noncohesive material $c = 0$, and the envelope is more or less represented by a straight line.

At the very surface of the bed, the strength of a virgin sediment bed amounts to c_d, as the surface sediments have not experienced any excess loads (only self-weight consolidation). A so-called virgin bed is formed from consolidation of a sediment–water mixture; this bed has not been subject to any

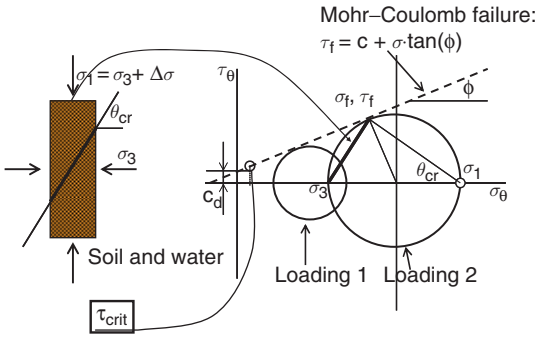

Figure 68 Sketch of triaxial test and subsequent circles of Mohr and Mohr–Coulomb failure envelope. The stress diagram also shows the angle of internal friction, the true cohesion, and the critical shear stress for erosion. Note that the Mohr–Coulomb envelope is often convex for cohesive sediments.

other deformations. When parts of the bed have been eroded, or if the bed experienced some kind of loading otherwise, the strength of the surface sediments deviates from c_d. However, due to swelling, such overconsolidated beds will soften to c_d (or slightly larger than c_d). Because of some effective stress at the sediment bed surface due to self-weight of the flocs themselves and overconsolidation, the normal stress at the bed surface is slightly larger than zero. This explains why the critical shear stress for erosion τ_{cr} is slightly larger than the drained shear strength c_d. By (our) definition, surface erosion is a drained process, that is, the maximum surface erosion rate of the bed is governed by the inflow of water. During erosion, the lower layers of the bed become (slightly) overconsolidated, and have to swell to the critical state conditions to enable failure (i.e., erosion) at zero deformation, for example, Figure 69. The critical shear stress from erosion then follows for the Mohr–Coulomb criterion:

$$\tau_{cr} = c_d + \sigma_s \sin\phi \quad \left(= c_d + \sigma'_{v,s} \sin\phi\right) \qquad [38]$$

where σ_s is the normal stress (or effective stress $\sigma'_{v,s}$) at the bed surface, which is slightly larger than zero for reasons explained above. The relation between the normal stress (or effective stress $\sigma'_{v,s}$) and the void ratio e is determined by the plasticity index PI (= $W_{LL} - W_{PL}$), as shown in Figure 69; void ratio and solid's volume concentration are related through $e = (1-\phi_s)/\phi_s$.

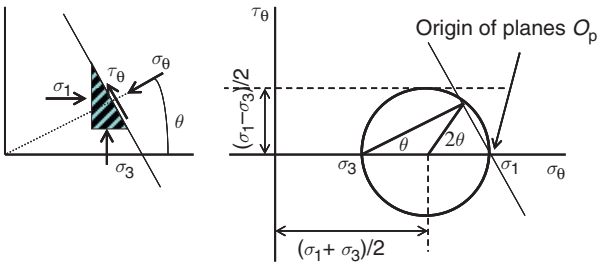

Figure 67 Example of 2D Mohr circle. The stresses on the soil in the left-hand side of the figure are plotted in a normal stress – shear stress diagram (the Mohr circle), showing the soil stresses at various angles θ, and defining the principal stresses σ_1 and σ_3.

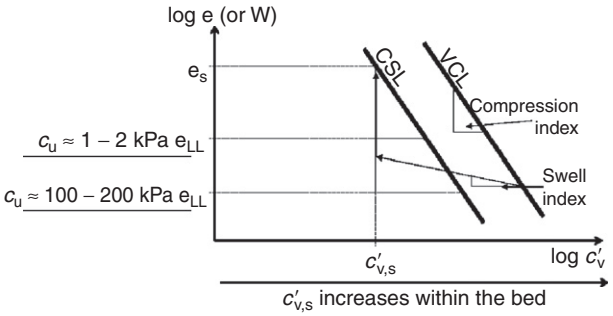

Figure 69 Effective stress for various void ratios (water contents), at the plastic limit e_{PL}, at the liquid limit e_{LL} and the surface e_s. The arrows indicate how the soil swells from the stress level at the virgin compression line to the critical state condition at the bed surface.

Observations reveal a more or less power-law relation, for example, Lambe and Whitman (1979), consistent with the convex shape of the Mohr–Coulomb failure curve. Note that an exponential relation is assumed in the so-called Cam-Clay model. (The Cam-Clay model describes the failure of a soil sample by shear and compression, and the critical state condition at which deformations without volume changes is possible (Roscoe and Schofield, 1963; Winterwerp and Van Kesteren, 2004). Basically, we can obtain the effective stress at the sediment bed surface from this relation, as the void ratio at the bed surface follows from the porosity of the bed-forming flocs. This power-law relation, in conjunction with eqn [38], suggests a power-law relation between the critical bed shear stress for erosion and the plasticity index. Indeed, Smerdon and Beasley (1959) found such a power-law relation:

$$\tau_{cr} = 0.163\ \mathrm{PI}^{0.84} \text{ with PI in \%} \qquad [39]$$

The critical shear stress for erosion τ_{cr} in eqn [39] should be interpreted as the mean value $\mu_{t,cr}$, introduced in eqn [37]. The power-law function of eqn [39] is consistent with the material functions for the consolidation equation, introduced in Section 2.15.4, which follow from a fractal description of the bed structure (e.g., Kranenburg, 1994).

Our experience is that eqn [39] yields too large values for τ_{cr}, which is most likely due to the very stiff clays used in the experiments in Smerdon and Beasley (1959). In that case, swelling does not retrieve the virgin conditions completely, that is, the compaction–swelling cycle is not fully reversible. Dedicated measurements are required to specify the coefficients in eqn [39] for softer sediments, as found in estuaries and coastal areas. Further, we observe that the effective stress increases with depth within the bed, as the bed's bulk density generally increases with depth. The relation between effective stress and bed density follows from consolidation theory, or from the overconsolidation ratio of the bed (Lambe and Whitman, 1979; Winterwerp and Van Kesteren, 2004).

Note that the Atterberg limits implicitly include the effects of sediment composition (sand–mud ratio) and of organic material. In other words, the effects of sediment composition and organic material are implicitly accounted for in eqn [39].

At equilibrium (virgin consolidation), the bed undrained shear strength amounts to c_u. However, the bed strength may be larger because of creep (secondary consolidation) and/or historical loadings.

Due to removal of sediment from the bed during erosion and the fluctuating turbulent stresses on the bed (generating pore-water pressure fluctuations, hence pore-water flows), swelling of the bed is induced. The rate of swelling V_s is given by Terzaghi's (1943) formula, which is given by the diffusion part of the consolidation equation (see Section 2.15.5), in which c_v ($\equiv \Gamma_s$) is the consolidation coefficient, and δ_s a measure of the position of the swelling front, for example, **Figure 70**:

$$\Gamma_c = \frac{2}{3-n_f}\frac{K_k K_p}{g\rho_w} \qquad [40]$$

The maximum erosion rate $V_e = \mathrm{d}\delta_e/\mathrm{d}t$ is governed by the swelling rate, as the undrained shear strength is generally larger than the stresses, which can be induced by a turbulent flow (or by waves). The relation between the erosion depth δ_e and swelling depth δ_s follows from a simple geometric approximation of the strength distribution within the bed, sketched in **Figure 70**:

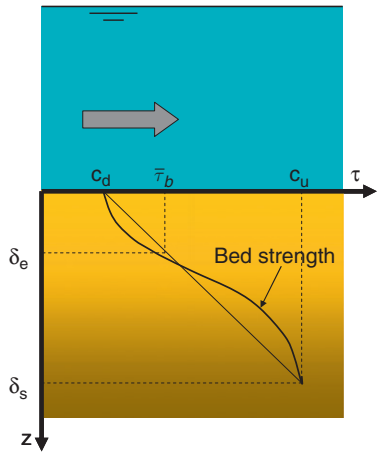

Figure 70 Sketch of swelling of the bed and its strength distribution; δ_e is erosion depth, and δ_s is swelling depth.

$$\frac{\mathrm{d}\delta_e}{\mathrm{d}t} \approx \frac{\mathrm{d}\delta_s}{\mathrm{d}t}\frac{\bar{\tau}_b - c_d}{c_u - c_d} \approx \frac{\mathrm{d}\delta_s}{\mathrm{d}t}\frac{\bar{\tau}_b - c_d}{c_u} \qquad [41]$$

We anticipate that surface erosion mobilizes subsequent layers of flocs; the floc size D_f is therefore a good measure of the typical length scale δ_e for the erosion process. From our treatment of flocs as fractal entities, we derive a formula relating floc size and volumetric concentration in the bed, where $\phi_f = 1$ by definition:

$$\phi_f = \phi_s\left(\frac{D_f}{D_p}\right)^{3-n_f} \text{ and } \delta_e \propto D_f = D_p\phi_s^{1/(3-n_f)} \qquad [42]$$

in which ϕ_s is the solids volume fraction, n_f the fractal dimension, and D_p the size primary particles (i.e., building stones of flocs). Typical values for n_f and D_p in the sediment bed are $2.6 < n_f < 2.8$ (Kranenburg, 1994) and $4 < D_p < 10\,\mu\mathrm{m}$ (i.e., much larger than the size of the clay particles themselves).

The surface erosion rate E_s ($\mathrm{kg\,m^{-2}\,s^{-1}}$) follows from the erosion velocity V_e ($\mathrm{m\,s^{-1}}$) by multiplication with the dry density ρ_{dry}, which also varies over the depth of the sediment bed:

$$E_s = \frac{c_v}{c_u D_p}\frac{\rho_{dry}^{(4-n_f)/(3-n_f)}}{\rho_s^{1/(3-n_f)}}(\bar{\tau}_b - \tau_{cr}) = M(\bar{\tau}_b - \tau_{cr}) \qquad [43]$$

Thus, we have derived a series of consistent formulations describing floc and surface erosion as a function of (a distribution of) soil mechanical properties of the bed, and the stochastic nature of the eroding turbulent flow. The various parameters of these formulations can be obtained from measurements of a number of soil mechanical bulk parameters, that is, Atterberg limits, consolidation coefficient, remolded shear strength, and dry density of the soil. These formulations are also consistent with our formulations for the consolidation of cohesive sediments, as discussed in Section 2.15.5, implicitly, or explicitly assuming a fractal, self-similar structure of the bed. Further to these formulations, we have to integrate explicitly the various formulations, and obtain data for verification – this is subject of ongoing research.

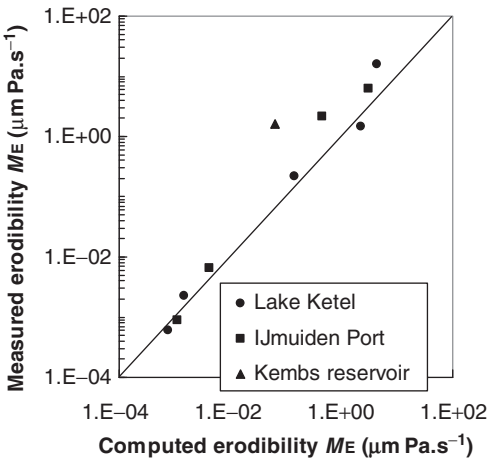

Figure 71 Comparison of erosion model [42] with various data obtained in an erosion flume in the laboratory (data from not-published experiments at Delft Hydraulics).

Figure 71 presents a comparison of the erosion model [43] based on soil mechanical principles and observations in an erosion flume, showing favorable agreement. For further details and parameter settings, the reader is referred to Winterwerp and Van Kesteren (2004).

Another mode of erosion is referred to as mass erosion. Mass erosion is often observed on highly consolidated mud deposits, as encountered on intertidal areas, casu quo mud flats, etc.; an example is shown in Figure 72. The bed attains large strengths as a result of physical (consolidation, drying), biological processes (vegetation, cohesion by polysaccharides, e.g., organic polymers), and sometimes chemical processes (cementing). Stresses induced by shear flow (even the normal stresses) are too small to induce much surface erosion. However, stagnation pressures (scaling with $\frac{1}{2}\phi\rho v^2$), in particular induced by (breaking) waves, can generate stresses large enough to erode very strong beds, as occurring, for example, on uneven bed surfaces, cliffs, etc. Experiments by Van Kesteren (2004) suggest that mass erosion occurs when

$$\tau_b = f_w \sigma_{stag} = \frac{1}{2} f_w \rho v^2 > (2\text{–}5) c_u \qquad [44]$$

Here, the stagnation stresses have been translated into bed shear stresses through a friction coefficient f_w to compare with other erosion modes.

We can summarize our analysis in the erosion diagram of Figure 73. The transition between floc and surface erosion is gradual – floc erosion also occurs during surface erosion conditions, its rate, though, is negligible. Figure 73 is summarized below (see also Jacobs, 2011):

$\overline{\tau}_b < 0.5\tau_{cr}$: stable bed
$0.5\tau_{cr} < \overline{\tau}_b < \tau_{cr}$: floc erosion
$\tau_{cr} < \overline{\tau}_b < 1.7\tau_{cr}$: floc and surface erosion
$\overline{\tau}_b > 1.7\tau_{cr}$: surface erosion
$\overline{\tau}_b > (2\text{–}5)c_u$: mass erosion (entrainment)

where $\overline{\tau}_b$ is the mean bed shear stress induced by the turbulent water movement.

We believe that the erosion formulas described above have a sound physical basis, and allow assessment of the coefficients required from bulk soil mechanical parameters, though more verification is necessary. However, for long-term modeling and/or in situations where the seabed is predominantly sandy and/or the amount of fines is limited, zero-order formulas are not appropriate. In these cases, we have to account for the history of the bed, keeping track of the amount of erodible fines in the bed. A two-layer approach is a simple method to account for this history.

Figure 74 presents a sketch of this two-layer approach, which was developed to simulate the long-term dispersion of fines in the sandy North Sea environment (Van Kessel et al., 2010). The basic idea is that during calm weather conditions, fines are deposited on the sandy North Sea bed, part of which is entrained into the sandy seabed by ripple migration, bioturbation, or otherwise. The fines on the seabed, that is, in the upper layer of the schematization, respond to regular variations in tidal flow induced bed shear stresses, whereas the buried fines are remobilized during storm events only.

The formulations for the waterbed exchange processes are then given by

$$\text{layer 1: } D_1 = (1-\alpha) W_s c, \; E_1 = m_1 M_1 (\tau_b - \tau_{cr,1}) \qquad [45]$$

$$\text{layer 2: } D_2 = \alpha W_s c, \qquad E_2 = p_2 M_2 (\tau_b - \tau_{cr,2})^{1.5} \qquad [46]$$

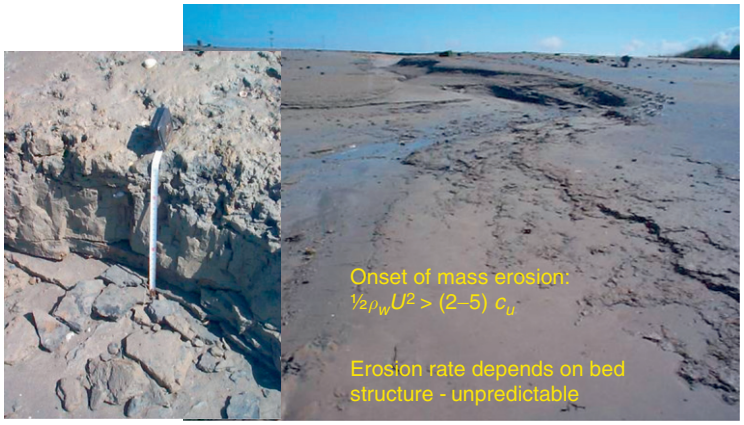

Figure 72 Photographs of mass erosion on intertidal mud flats.

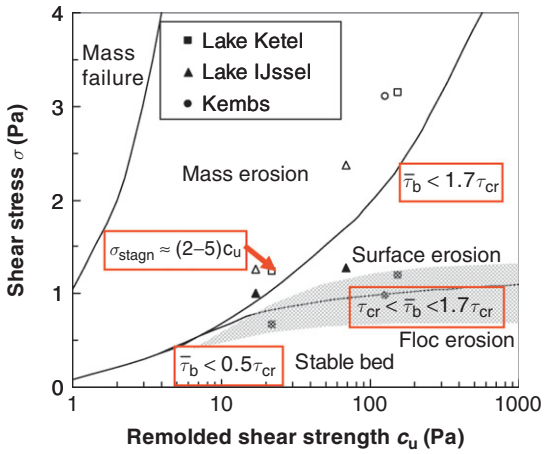

Figure 73 Erosion diagram showing the various modes of erosion as a function of bed strength and eroding stresses; $\bar{\tau}_b$ is the peak bed shear stress.

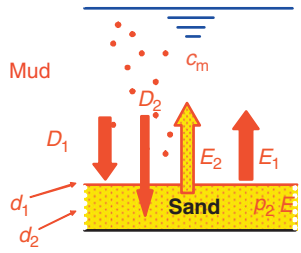

Figure 74 Cartoon of two-layer bed model to account for sand-mud beds and long-term monitoring.

where α is the entrainment (bed mixing) coefficient, m_1 the mass of fines in layer 1 (i.e., on the sandy seabed, or in the bed, near the bed surface), and p_2 the fraction of fines in layer 2 (i.e., deeper into the sandy seabed). We have added the exponent 1.5 to the erosion formula [46] to account for the erosion of the sandy substrate of the bed (pick-up function by Van Rijn (1993)). The erosion parameters for the sandy substrate, M_2 and $\tau_{cr,2}$ cannot be established from this chapter, and have to be found from literature on noncohesive sediment transport.

This first-order formulation was calibrated against observations at Noordwijk 10, an anchor station 10 km off the Dutch coast in the North Sea. The results presented in **Figure 75** show a favorable agreement with the observations. In particular, the peaks in suspended particulate matter (SPM) are reproduced quite well, which is impossible with the classical zero-order formulation.

Next, this first-order model is applied to the entire southern North Sea, simulating the entire year 2000 (i.e., prescribing the 2000 tidal boundary conditions and wave and wind forcing). The results are shown in **Figure 76**, distinguishing between summer and winter conditions (winter is quite stormy in the North Sea); for comparison, the results obtained with the classical zero-order approach are included as well. Moreover, **Figures 76(c)** and **76(d)** show favorable agreement with observations in the North Sea, for example, **Figure 77**. For further details, the reader is referred to Van Kessel et al. (2010).

A final note in this section on erosion of cohesive sediment beds should be addressed to the effects of waves. Through their orbital motion, waves induce considerable bed shear stresses, often greatly exceeding normal flow-induced bed shear stresses. As such, waves can contribute substantially to the erosion of sedimentary beds. Furthermore, waves induce considerable normal stresses within the bed, which must affect the stability of the bed as well. However, the impact of normal stresses is not well understood (this also holds for the effects of normal stresses induced by turbulent flow) and are therefore

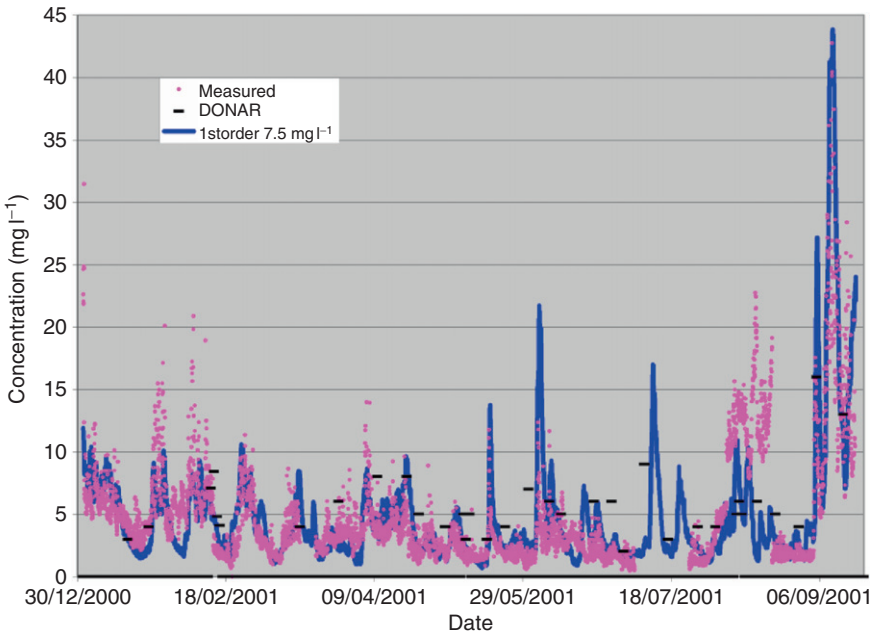

Figure 75 Calibration result against CEFAS data Noordwijk 10 in the year 2001.

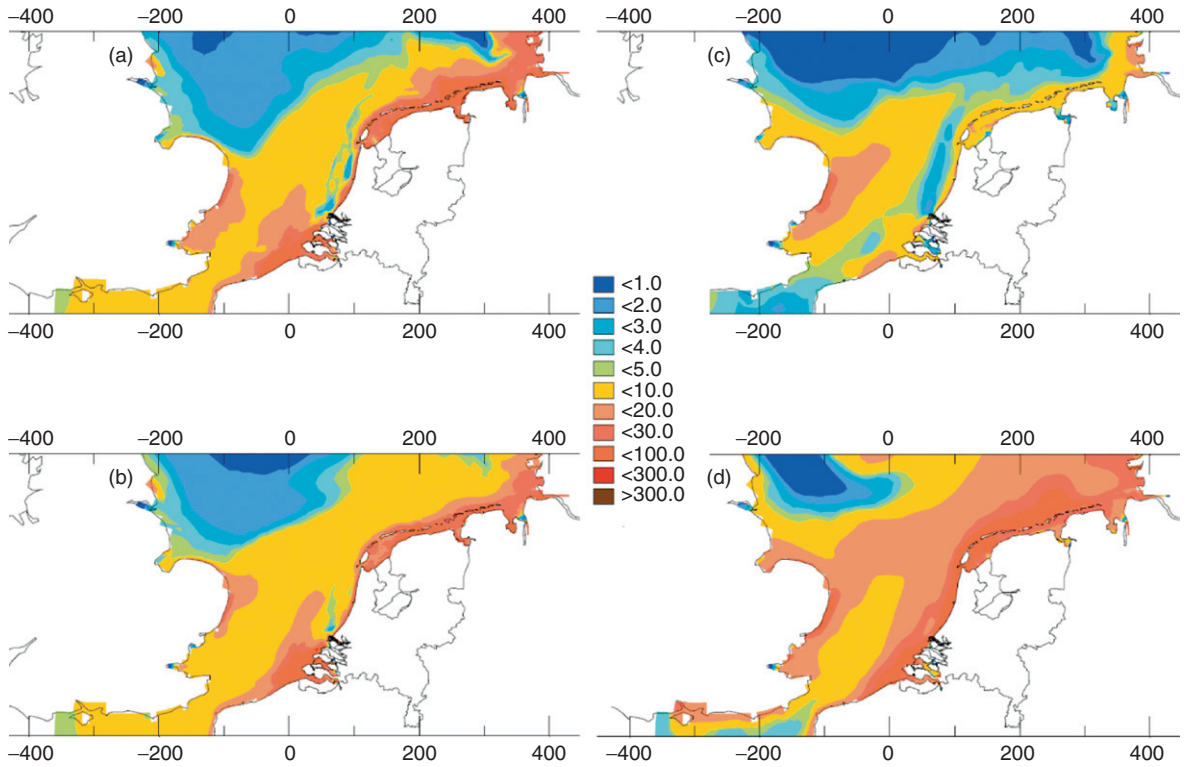

Figure 76 Computed SPM concentration (in mg l^{-1}) is summer (a, c) and winter (b, d) 2000. (a, b) Without sediment buffering in seabed; (c, d)with sediment buffering in seabed (two-layer approach).

commonly ignored. (Note that the stress gradients induced by waves may liquefy a cohesive sediment bed – gradients in the normal stresses play an important role in this. We discuss liquefaction further in the next section of this chapter.) Of course, their effect is implicitly accounted for in the empirical parameters derived from erosion experiments.

The turbulent boundary layer induced by nonbreaking waves is very thin (a few millimeters, up to the order of a centimeter),

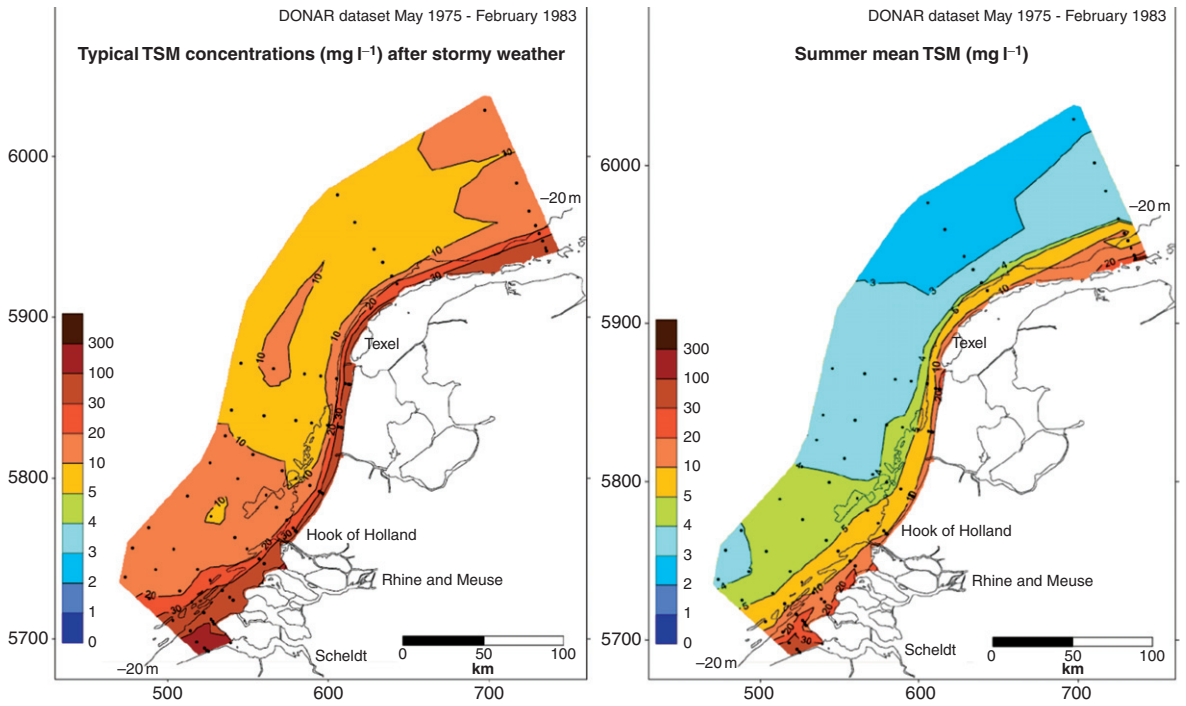

Figure 77 Observed SPM concentration after stormy weather (left) and summer mean level (right). From silt atlas Suijlen and Duin (2001).

and waves induce little vertical mixing by themselves. However, in combination with (tidal) flow, waves do have an effect by augmenting the apparent roughness of the flow boundary layer, thereby increasing vertical mixing in the coastal zone. The literature contains a number of models describing flow–wave interaction; we refer to Grant and Madsen (1979) for a complete and not too complicated model, describing the effects of wave–current interaction on the bed shear stress and vertical mixing.

Currently, we recommend to synthesize the bed shear stresses induced by currents and waves, following, for instance, Soulsby et al. (1993), in the various erosion formulas found in the literature. Chapter **2.10** discusses the effects of wave–current interaction in more detail. Note that breaking waves have a large impact on the sediment dynamics in coastal areas, but the conditions in the breaker zone are so dynamic, that fine sediments cannot settle in general, and wave breaking is of minor importance with respect to these fine sediments, apart from the wave's role in coastal erosion, and the subsequent mobilization of fine sediments (Holderness cliffs).

2.15.7 Fluid Mud Behavior

In this section, we treat the formation and behavior of fluid mud. Theoretically, fluid mud may be formed from rapid deposition, liquefaction, and/or fluidization of the sediment bed. Although fluid mud formation by liquefaction has been frequently observed in the laboratory, liquefaction under real-world conditions is likely to be rare, or maybe even impossible (e.g., Winterwerp et al., 2011). Fluid mud can also be formed from fluidization, when water is injected into the bed. Fluidization can be induced mechanically, for instance, by water injection dredging, a dredging technique aimed at generating fluid mud flows cleansing harbor basins, etc.

Note that we distinguish:

liquefaction – failure of the bed at undrained conditions (density remains constant) and

fluidization – failure of the bed at drained conditions by adding water (density decreases).

In this section, we focus on fluid mud formed from (rapid) deposition. We should realize that fluid mud is in a so-called transient state, as it consists of a consolidating water–mud mixture. Even if the fluid mud were mobile, no turbulence is generated to keep the particles in suspension. If such a mobile fluid mud layer were accelerated, becoming turbulent, we would then refer to it as a turbidity current.

However, fluid mud can be kept from complete consolidation by externally induced shear stresses (possibly also by internally generated shear stresses), generated by strong currents and/or wave action. In the mouth of the Amazon, for instance, flow-induced shear keeps the fluid mud layers mobile (Vinzon and Mehta, 2003). The reader is also referred to McAnally (2007a, 2007b)

The literature mentions a large variety of values for fluid mud concentration/density, which can be explained from two observations:

1. When fluid mud is formed from rapid deposition, the initial sedimentary structure (gelling concentration) depends on the structure and density of the depositing flocs. We have shown that c_{gel} varies with D_f, D_p, and n_f; in particular the structure of the mud layer described through n_f is important.
2. Fluid mud is in a transient state – it cannot be stable, as there is no turbulence to keep the particles in suspension. Hence, the sediment–water mixture is expected to consolidate, unless external energy is supplied to the mixture.

Figure 78 presents the reflections of a dual frequency echo sounding in the Ems River, along the border of the Netherlands and Germany. The high-frequency 210-kHz signal reflects on fairly weak density gradients (acoustic impedance), whereas the lower-frequency 33-kHz signal penetrates further into the mud prior to reflection. Commonly, the 210-kHz reflection is interpreted as the top of the fluid mud layer, whereas the 33-kHz reflection would indicate the 1200 $kg\,m^{-3}$ isobath, though this value may change with location.

Figure 78 would yield a fluid mud thickness of around 1.5–2 m. As ships may sail through fluid mud, the concept of navigable depth is often related to the response of these dual frequency echo sounders.

Intuitively, we can presume that fluid mud occurrences from deposition are formed when the deposition rate exceeds the consolidation rate (largely). As the consolidation time scales with the mud layer thickness squared (e.g., Section 2.15.4), we anticipate that layers of fluid mud are fairly thick in general.

We argued in Section 2.15.4 that hindered settling in suspensions of cohesive sediment occurs at relatively low mass concentrations (few $g\,l^{-1}$), as a result of the large water content of the flocs. This implies that interfaces, that is, lutoclines, may easily develop at such small mass concentrations, which has a profound effect on the behavior of suspensions of cohesive sediment.

The interfaces/lutoclines in cohesive sediment suspensions induce fairly large gradients in bulk density of the mixture. These density gradients damp vertical turbulent mixing, as work has to be done to overcome these density gradients.

The interaction between lutocline formation and turbulence damping (e.g., **Figure 79**) may induce positive feedback processes that have profound implications for the transport capacity of sediment-laden flow.

In most open water systems (apart from lakes where the hydrodynamics are governed by wind stresses), most of the turbulence is generated at/near the bed, where velocity gradients are large. This would result in situations where the lower, high-density suspension is turbulent, and the water column above the lutocline becomes less turbulent with time, as the density gradients over the lutocline increase.

Note that with increasing density, the lower high-density suspension builds up strength and enhanced viscosity. Then, this layer becomes stagnant, and the consolidation rate increases substantially.

The literature contains a large number of formulations describing this buoyancy-induced turbulence damping. In this chapter, we apply a damping term in the k–ε turbulence model, in conjunction with the equation of state, relating fluid density to suspended sediment concentration (Winterwerp, 2002).

The positive feedback between vertical suspended sediment concentration gradients and vertical mixing (turbulence)

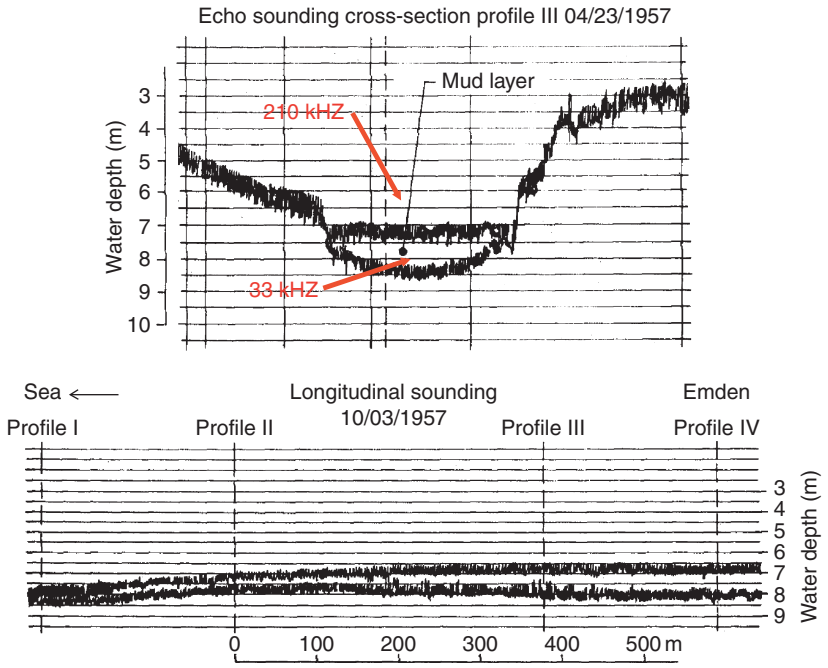

Figure 78 Typical reflections from a dual frequency echo sounder – data from the Ems River, the Netherlands/Germany. The difference between the two reflections is an indication for the thickness of the fluid mud layer, amounting to almost 2 m.

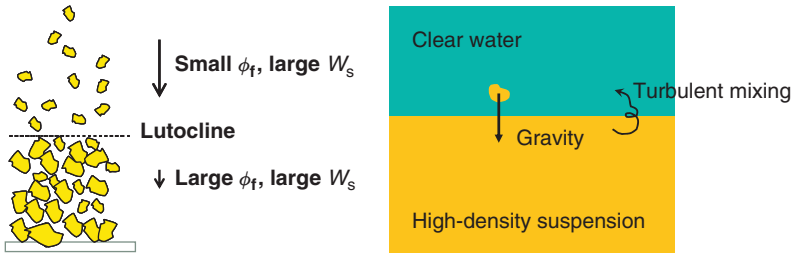

Figure 79 Cartoon of the formation of lutoclines induced by hindered settling and the subsequent damping of vertical turbulent mixing.

mentioned above may lead to a condition referred to as saturation. A necessary condition for saturation is an unlimited availability of sediment (in/on the bed).

Let us analyze the conditions in a hypothetical open channel flow, where the vertical profile of suspended sediment is at equilibrium with the flow conditions. This situation is addressed in all textbooks on (noncohesive) sediment transport, referred to as equilibrium transport or capacity conditions. Assume that, starting from equilibrium, the flow velocity suddenly decreases, for instance, in case of channel divergence and/or over a depression or channel in the seabed. In the case of noncohesive sediment (e.g., sand), a new equilibrium, Rousian concentration profile is formed almost immediately, but at a smaller sediment load; the surplus of sediment from the suspension settles, forming a rigid bed immediately. This behavior is sketched in Figure 80.

For cohesive sediment another picture emerges. Upon settling, in reaction to the smaller flow velocities, the mud flocs form a layer of fluid mud owing to their large water content, inducing pronounced gradients in density in the water column, resulting in a pronounced damping of vertical mixing. As a result, less sediment particles can be kept in suspension. These particles settle as well, increasing the sediment-induced density gradients further, hence a further decrease in turbulence, hence mixing capacity. Thus, a snowball effect is initiated (positive feedback) and a complete collapse of the turbulent field and the concentration profile is the result. Note that the major difference between cohesive and noncohesive sediments consists of the water content of the flocs of the

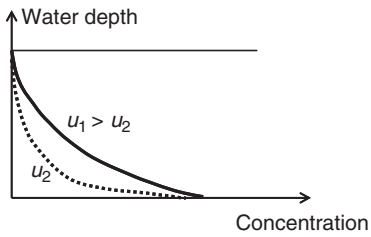

Figure 80 Adaptation of vertical sediment concentration profile in decelerating flow – noncohesives.

cohesive sediment: settling basically forms a dense fluid on the bed (fluid mud!). It has been found that such a collapse always starts near the water surface, where turbulence levels are relatively low (e.g., Soulsby and Wainwright, 1987).

Figure 81 shows the results of a simulation with a 1DV point model. This is a full 3D model (in fact Delft3D, e.g., Winterwerp, 2001) in which all horizontal gradients have been stripped, except for the horizontal pressure gradient. We simulate an open channel flow with a depth of 16 m and a flow velocity of 0.2 m s^{-1}. At $t = 0$, we distribute an amount of fine cohesive sediment at a concentration $c = c_0 = 23$ mg l^{-1} homogeneously over the water column. Then we run the model, and after some time a more or less Rousian profile develops. Close inspection of the eddy viscosity profile shows small deviations from the neutral parabolic profile though, because of buoyancy effects (e.g., Winterwerp, 2001).

Next, we repeat this simulation, but increase the initial concentration to 24 mg l^{-1}. Now we observe an entirely different behavior: a complete collapse of the concentration profile (and of the turbulence profile – not shown here, e.g., Winterwerp, 2001). This behavior is referred to as saturation; the depth-averaged concentration C_s just prior to saturation is called the saturation concentration, which is a measure for the transport capacity of the sediment-laden flow (Figure 82).

This saturation behavior can be analyzed with classical stratified flow theory through an elaboration of the flux Richardson number $\mathbf{Ri}_f$, which can be considered as an efficiency parameter for vertical mixing, and is defined as

$$\mathbf{Ri}_f = -\frac{g\overline{w'p'}}{\rho\overline{u'w'}\partial u/\partial z} = -\frac{\Delta g\overline{w'c'}}{\rho\overline{u'w'}\partial u/\partial z} \qquad [47]$$

where a prime denotes turbulent fluctuating quantities. There is empirical evidence (Turner, 1973) that a turbulent shear flow collapses when $\mathbf{Ri}_f > 0.15$. In a zero-order approximation, the vertical velocity profile is logarithmic; hence, the eddy viscosity profile is parabolic. Intuitively, we presume that at saturation, $\mathbf{Ri}_f$ is critical over the entire water depth. Then, eqn [47] becomes

$$C_s \equiv \frac{1}{h}\int_0^h c_s \mathrm{d}z = K_s \frac{\rho}{\Delta g}\frac{u_*^3}{hW_s} \qquad [48]$$

At concentrations around C_s, the flow is still fully turbulent (and the suspension fully Newtonian in the left branch of the sediment stability diagram, e.g., Figure 83). The large sensitivity to the flow velocity (u_*) explains the large variations in C_s, with values as low as a few 10 mg l^{-1} – see also Figure 81. Note that this saturation concept is similar to Bagnold's auto-suspension criterion (Bagnold, 1966), which yields conditions for the self-preserving of turbidity currents:

$$C < \frac{\rho}{\mathrm{D}g}\frac{U_t u_*^2}{\delta W_s} \qquad [49]$$

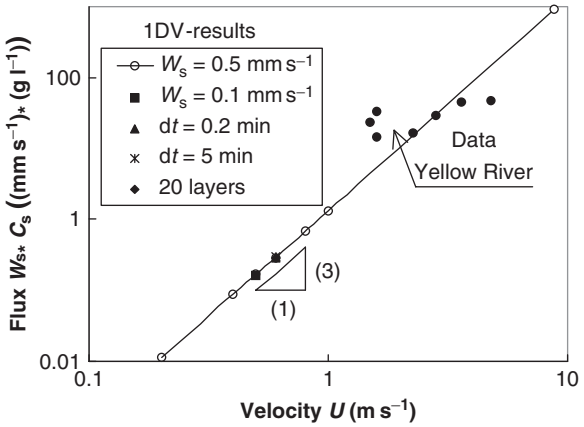

Figure 82 Saturation concentrations as a function of depth-mean flow velocity, results from 1DV-simulations.

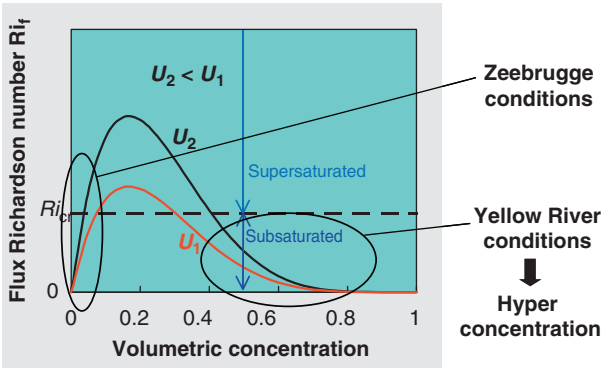

Figure 83 Stability diagram for sediment-laden flow. The regime for $\mathbf{Ri}_f > \mathbf{Ri}_{f,cr}$ is a forbidden zone – turbulence conditions cannot be maintained, and the concentration profile collapses.

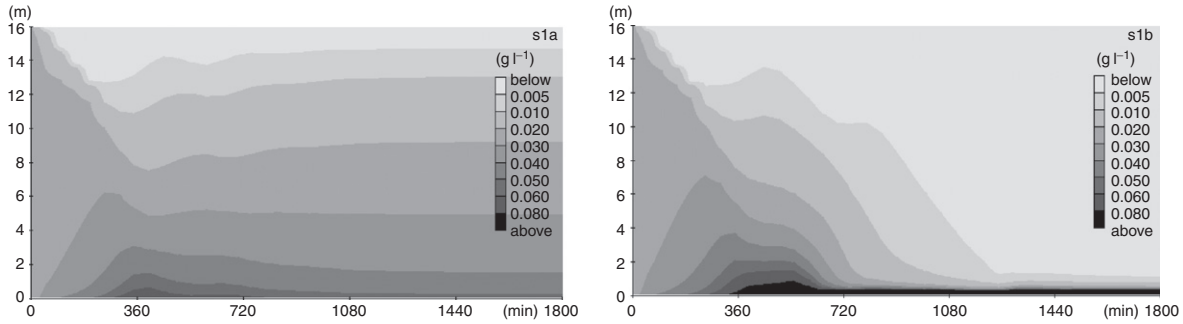

Figure 81 1DV simulations for steady flow in a hypothetical channel $h = 16$ m depth, mean flow velocity $U = 0.2$ m, and settling velocity $W_s = 0.5$ mm s^{-1}; (left panel) initial sediment concentration $c_0 = 23$ mg l^{-1}; (right panel) $c_0 = 24$ mg l^{-1}; simulations without waterbed exchange (all sediment remain within computational domain).

where U is mean turbidity current velocity, u_* its shear velocity, and δ its thickness. Bagnold derived at eqn [49] from energy considerations. We have carried out numerous numerical experiments, and, in all cases, such a rapid collapse was observed. We have collected a few of our many 1DV simulations in Figure 82, showing a variation of C_s with U^3, as follows from our analytical approach. Moreover, we have plotted a few data from the Yellow River, which agree more or less with our relation (see also later in the chapter).

Figure 84 presents data by Chinese researchers (Xu, 2003) for the Yellow River and its tributaries and a number of irrigation channels, covering almost four orders of magnitude in suspended sediment concentration, hence fine sediment load. We have plotted relation [48] for the saturation equation C_s here as well, where K_s follows from simulations with the 1DV point model with standard settings. We note that these simulations overpredict the observations slightly, though the observational trend is captured.

Therefore, we rerun the 1DV model with a larger Prandtl–Schmidt number, that is, $\sigma_T = 2$ (instead of the standard value of 0.7), as follows from laboratory experiments by Cellino and Graf (1999) (see also Winterwerp, 2001; Winterwerp et al., 2009). With this value, the data are well reproduced over the entire concentration range. The need for a larger σ_T is explained by the stratification of the water column caused by the suspended sediment. The buoyancy-induced damping of vertical mixing is larger for the turbulent transport of matter than of momentum, as internal waves can transfer momentum, but not mass.

It is remarkable that this simple approach, based on stratified flow theory, can reproduce these data so well over such a large range, which gives confidence in the concept of saturation. For more information, the reader is referred to Winterwerp (2001) and Winterwerp et al. (2009).

If we incorporate the effects of hindered settling, the saturation criterion yields an important stability diagram for the behavior of sediment-laden flows. This diagram is sketched in Figure 83. Let us again analyze the behavior of a sediment-laden flow in an open channel with flow velocity U_1. We start left in the diagram at $\phi \approx 0$. Upon increasing the suspended sediment concentration ϕ (for instance, due to erosion of the bed), the flux Richardson number $\mathbf{Ri}_f$ increases, possibly up to $\mathbf{Ri}_{f,cr}$. A further increase in ϕ can no longer be accommodated by the flow, and sediment concentration profile and turbulence field collapse, as discussed before. C_s reflects the capacity conditions of the flow.

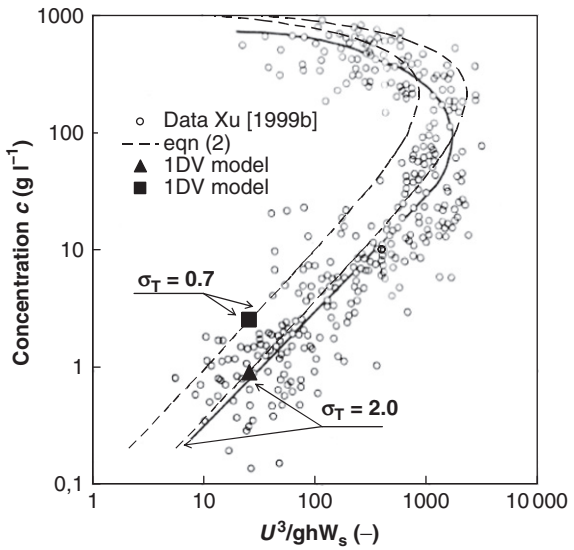

Figure 84 Comparison of eqn [48] with data from Chinese researchers. K_s in [48] has been obtained with the 1DV model, with $\sigma_T = 0.7$ and 2.0 – see text for explanation.

Beyond this forbidden regime (right-hand-side branch of the curve, supersaturated conditions) an increase in ϕ would yield a decrease in $\mathbf{Ri}_f$, as the effective settling velocity of the particles decreases by hindered settling. This implies that the flow likes to erode the bed, not only because it takes less energy to carry the sediments, but also because its excessive mass, propelling the turbidity current, increases. This explains why turbidity currents (hyperconcentrated flows) can be so persistent.

Let us next extend our analysis by introducing a second curve for a smaller flow velocity U_2. If for some reason (channel divergence or channel deepening), the flow velocity decreases from U_1 to U_2, $\mathbf{Ri}_f$ increases fast because of its third power dependency. Rapidly we enter the forbidden regime, as shown earlier. The same occurs at high concentrations. However, in this case, the sediment load is so large that massive deposition occurs and turbulence freezes. This occurs, for instance, in clogging pipelines transporting sand–water mixtures, or in the Yellow River – the latter case may initiate catastrophic events as the discharge capacity of the river decimates.

Also for oscillating flow (tidal conditions), saturation is found as well within a very small range of suspended sediment concentrations, as can be seen in Figure 85. Again, we start with an initially homogeneous suspended sediment concentration ($C_0 = 280\ \mathrm{mg\,l^{-1}}$) in an open channel of 8-m depth and a tidal flow ($T = 12.5$ h) with $0.5\ \mathrm{m\,s^{-1}}$ velocity amplitude. Under equilibrium conditions, we observe settling around slack water, forming a layer of fluid mud, followed by almost full mixing over the water column, attaining a Rouse-like concentration profile.

If we increase the initial concentration slightly, we observe a full collapse again, and a layer of fluid mud is formed. Winterwerp (2002) showed that for tidal flows a relation for C_s, somewhat different from eqn [48], can be derived. The reason for this difference is that collapse and remixing are not symmetrical because turbulence is almost fully damped in the case of fluid mud formation. Therefore, re-entrainment of the sediments within the fluid mud layer plays a role as well in establishing saturation conditions. We will not further elaborate on this here.

The saturation concept can also explain autosaturation under waves. Let us examine the response to eroding waves over a muddy seabed and an initially empty water column. Waves can erode fine sediments easily from the seabed, which are mixed over the water column by the turbulent flow. We have implemented the flow–wave interaction formulation by Grant and Madsen (1979) in the 1DV point model.

In this 1DV simulation, we study the effect of waves with a significant wave height of 1.8 m at a period of 5 s, a water depth of 16 m, and a tidal flow with amplitude $U_m = 0.5\ \mathrm{m\,s^{-1}}$. The results in Figure 86 show an increase in suspended sediment concentration in the water column during the first hour of the numerical experiment. Then, saturation conditions are met,

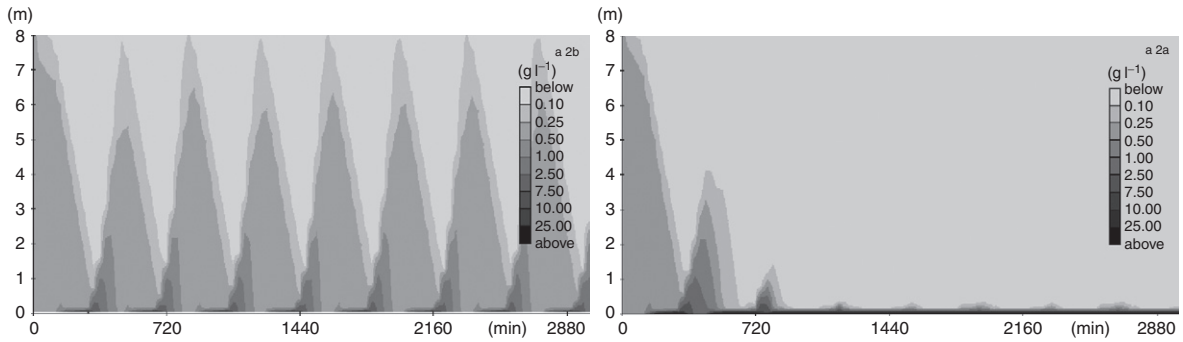

Figure 85 1DV simulations for tidal flow conditions in a hypothetical channel $h = 8$ m depth, mean flow velocity amplitude $U_m = 0.5$ m, and settling velocity $W_s = 0.5$ mm s^{-1}; (left panel) initial sediment concentration $c_0 = 280$ mg l^{-1}; (right panel) $c_0 = 290$ mg l^{-1}; simulations without waterbed exchange (all sediment remains within computational domain).

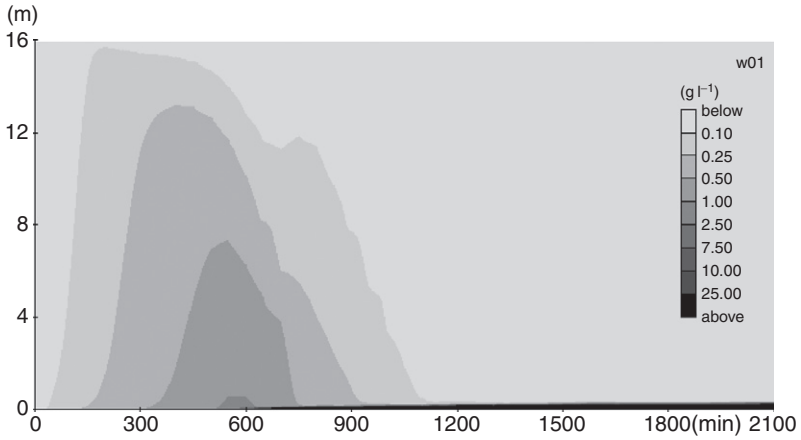

Figure 86 1DV simulations tidal flow with waves in hypothetical channel $h = 8$ m depth, mean flow velocity amplitude $U = 0.5$ m s^{-1}, wave height $H_s = 1.8$ m, and settling velocity $W_s = 0.5$ mm s^{-1}; initial concentration $c_0 = 0$; simulations with erosion from the seabed, but no sedimentation.

and the concentration profile and turbulence collapse, and a layer of fluid mud is formed. We refer to this behavior as autosaturation, and we anticipate that this mechanism plays a role in the behavior of the mud banks off Kerala coast (India) and other places in the world. For more information, see Winterwerp (2001).

Next, we show how the interaction between turbulence and suspended sediment affects floc forming, inducing a second, important positive feedback in high-concentrated mud suspensions. For this purpose, we examine how flocculation, hindered settling, and buoyancy destruction affect the sediment dynamics in the River Ems, the Netherlands/Germany. Data have been collected by Van Leussen (1994), for example, **Figure 87**. The river flow during the measurements was very low (~10 m^3 s^{-1}), and salinity-induced stratification and horizontal gradients in salinity and suspended sediment concentration do not play a role; a 1DV approach is feasible.

We use the full 1DV point model, that is, with sediment-induced buoyancy destruction in the k–ε turbulence model, the hindered settling formula by Winterwerp (2002), and a Eulerian flocculation model. Consolidation is not accounted for and all sediment is kept within the computational domain (no waterbed exchange processes). We prescribe the measured variations in water level, flow rate (not velocity!), and sediment load (not suspended sediment concentration). Parameters for the flocculation model were obtained from settling column measurements by Van Leussen (1994). For more information, the reader is referred to Winterwerp (2002).

First, we discuss the results of a prognostic simulation of fluid mud formation at measuring station 3 around slack water. In these simulations, we prescribe the flow rate and sediment flux, and keep all sediment in the computational domain (i.e., no waterbed exchange). We present vertical profiles of the sediment concentration at 3 times around slack water conditions, when a fluid mud layer is formed from settling. **Figure 88** shows that the 1DV model gives a fair representation of the evolution of the fluid mud layer, with respect to both its thickness and its concentrations.

Figure 89 shows the measured isolutals at station 2 (i.e., lines of constant suspended sediment concentration). Around $t = 960$ min, a sudden increase in suspended sediment concentration is observed. This is due to slope instability, as a result of which a large amount of mud slides into the measuring domain. The picture of **Figure 89** is characterized by a rapid settling prior to high water and the formation of a highly stratified sediment concentration profile during ebb, whereas the sediment is fairly well mixed during flood. In the following, we analyze these features further.

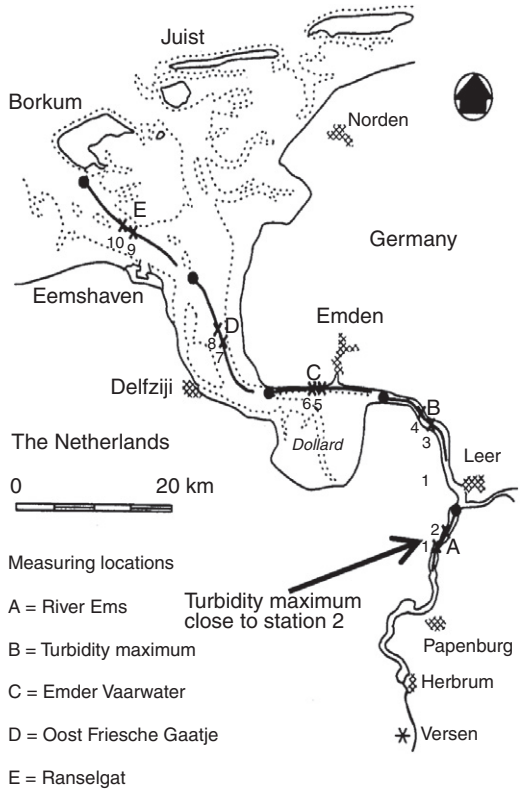

Figure 87 Plan of Ems River with measuring stations (Van Leussen, 1996) and location of turbidity maximum.

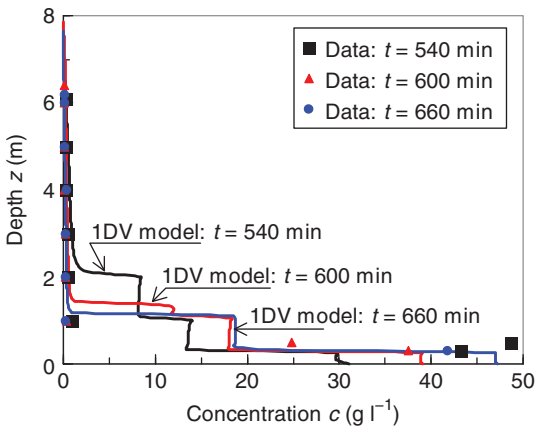

Figure 88 Predictions of fluid mud formations in the Ems River with the 1DV model and comparison with data.

In **Figure 90** we show that the full 1DV model (e.g., Winterwerp, 2002), that is, including the Eulerian flocculation model and sediment-induced buoyancy destruction in the turbulence model, represents the characteristic features of the sediment concentration patterns fairly well: rapid settling around high water and sediment stratification during ebb. Hence, **Figures 89** and **90** are qualitatively similar. Further details are given in **Figure 91**, comparing measured vertical suspended sediment concentrations with the 1DV model at a few times, showing again a fair reproduction of the characteristic features of the concentration profiles.

To emphasize the importance of the various processes, we have rerun the 1DV model without the flocculation module (e.g., a constant settling velocity, **Figure 92(a)**) and without sediment-induced buoyancy effects (e.g., a constant water density – no sediment effects on vertical mixing, **Figure 92(b)**). **Figures 92(a)** and **92(b)** show that we are not able to reproduce the two profound features of the observations of **Figure 89**, that is, rapid settling around high water and strong stratification during ebb.

For a further understanding, we analyze the computed variation in floc size, shown in **Figure 93**. Comparison with **Figure 94** shows that the computed values are in the proper range, though the 1DV model predicts larger variations.

The floc size shows a pronounced variation over the tidal cycle, with maximum values around slack water and pronounced gradients in D_f over the water depth. This behavior can be explained from the sensitivity of the floc size to the turbulent shear and the suspended sediment concentration ($D_f \propto c/\sqrt{G}$, e.g., Section 2.15.3). Moreover, the floc size responds rapidly to changes in hydrodynamic conditions, as the flocculation time T_f, which scales with $(cG)^{-1}$ (Section 2.15.3), is short because c is large. Around slack water, G is small, thus D_f and hence W_s become large. This explains the rapid deposition prior to high water in **Figures 89** and **90**.

The 1DV model predicts an unstable floc size distribution during flood and a stable distribution during ebb: during flood, the larger flocs are found near the water surface, whereas during ebb, the larger flocs are found near the bed. Apparently, during flood the effect of turbulence (G) wins, whereas during ebb the effects of the suspended sediment (c) win (this asymmetry itself is owed to the asymmetry in the tide, e.g., Winterwerp, 2002). The unstable flood conditions imply that the larger, near-surface flocs settle, break up near the bed, and are remixed. During ebb, the larger flocs are situated near the bed, and this stable situation explains the stratification observed in **Figures 89** and **90** (note that salinity effects do not play any role during this period). These arguments also explain why we need the full 1DV model to reproduce the observations and why the settings of **Figure 92** fail to capture the characteristic features of the Ems River.

The positive feedback, discussed above, is further illustrated in **Figure 95**, showing the computed vertical eddy viscosity profiles during flood and ebb. During flood, the eddy viscosity profile is only slightly affected by the suspended sediment. However, during ebb, the eddy viscosity is almost entirely damped by the suspended sediment, being one order of magnitude smaller than for neutral conditions.

Next, we discuss two features of fluid mud, that is, its motion and its interaction with waves. First, we discuss the movement of fluid mud, appreciating that all turbulence has damped and therefore this motion can only be laminar. (Note that fluid mud may become turbulent as well, Le Hir (1997) and Bruens et al. (2011).) Such movements may be induced by tide-induced pressure gradients (e.g., Le Hir, 1997), flow-induced drag forces (as these are small in general, this is not a common feature), wave-induced radiation stresses, and by gravity, when the fluid mud has been formed on a slope.

Let us analyze the conditions under which fluid mud may become mobile. For larger times, the consolidation equation evolves into a diffusion equation (e.g., Terzaghi's equation, see

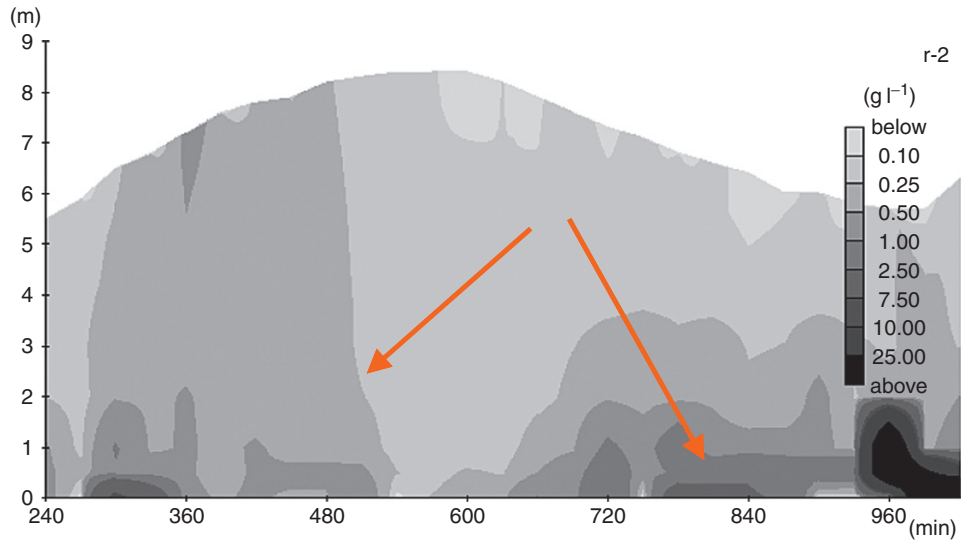

Figure 89 Measured isolutals in the Ems River – note rapid settling around high water and large stratification during ebb.

Winterwerp and Van Kesteren, 2004). The density distribution $\rho_b(z)$ within the soil then attains a logarithmic profile:

$$\rho_b \propto \ln\{z\} \quad [50]$$

The bed strength (yield strength) τ_y scales with the porosity of the bed and its structure (e.g., Kranenburg, 1994; Winterwerp and Van Kesteren, 2004):

$$\tau_y \propto \phi_s^{2/(3-n_f)} \quad [51]$$

$$\tau_y \propto \phi_s^{2/(3-n_f)}$$

Hence, we expect increasing strength with depth. If the bed experiences a hydrodynamic stress τ_h, induced by, for instance, currents (hydraulic drag) or waves (radiation sresses), a shear plane (plane of failure) will develop at the level where $\tau_h = \tau_y$. All sediments above this shear plane will become mobile, most likely in the form of plug flow, as sketched in Figure 96. Radiation stresses are further discussed in Chapter 2.10.

A similar stress balance can be drawn for fluid mud deposits on a sloping bed. When the fluid mud attains a certain thickness (and if the slope is large enough and the bed is not too strong), a shear plane develops where the along-bed component of the mud's mass exceeds the mud's strength. The mobile fluid mud may accelerate moving downhill, eventually becoming turbulent. Then, the mobile fluid mud layer evolves into a turbidity current.

Coussot (1997) presented an excellent overview of unstable fluid mud deposits, shear planes and accompanying plug flow, and turbidity currents, using various rheological models, relating mud strength to its density.

Let us finally discuss the interaction of waves with fluid mud. Many muddy coastlines depict significant damping of wave energy (Thailand, Guyana coast, south Brazil, Louisiana

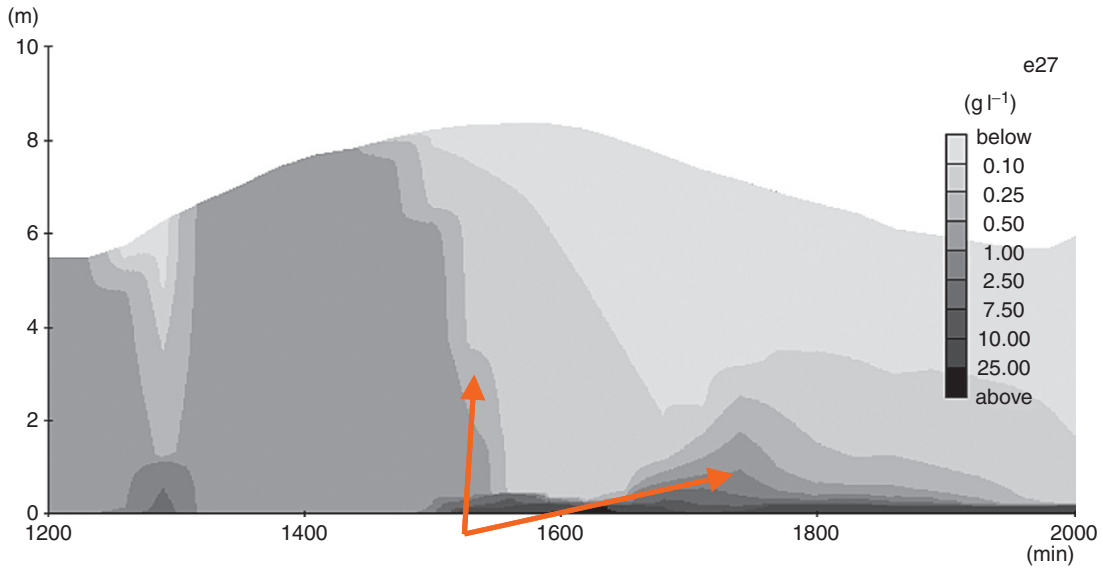

Figure 90 Computed isolutals in the Ems River reveal same rapid settling and stratification features as Figure 89.

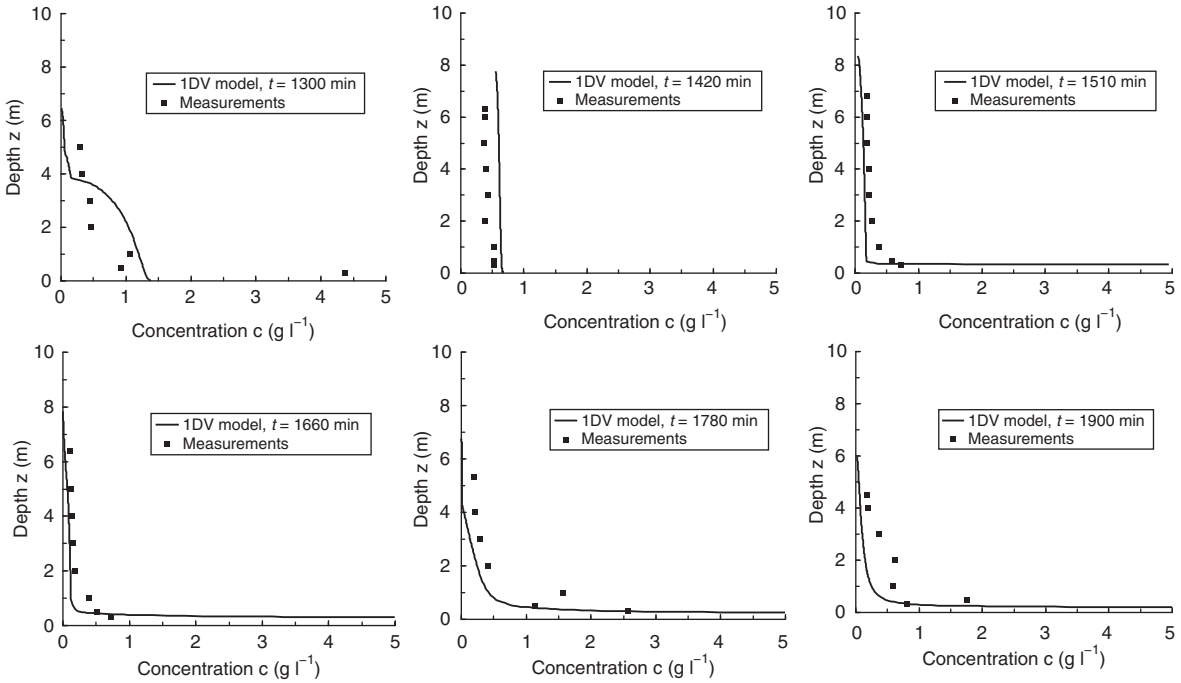

Figure 91 Comparison of measured and computed vertical profiles in suspended sediment concentration, the Ems River, the Netherlands/Germany.

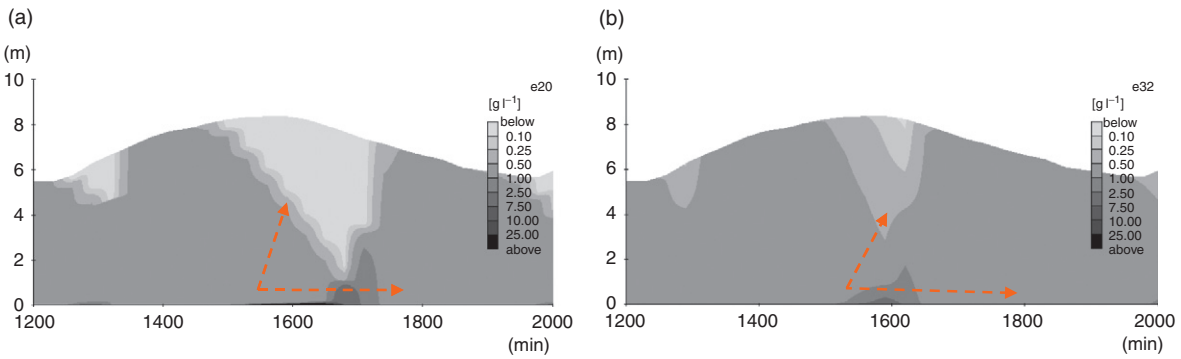

Figure 92 (**a**) 1DV simulations with constant W_s, otherwise **Figure 90** conditions. (**b**) 1DV simulations without buoyancy, otherwise **Figure 90** conditions.

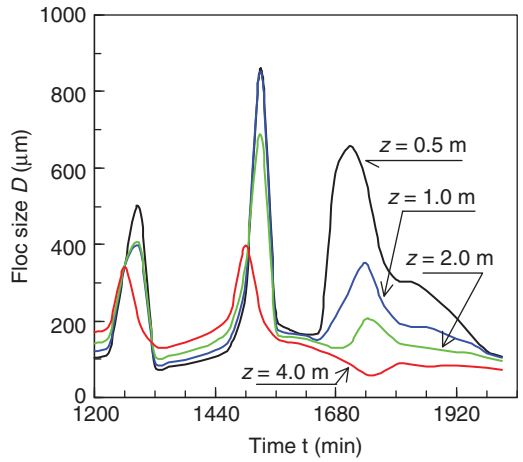

Figure 93 Computed variation in floc size D_f; $z = 0$ = bed level.

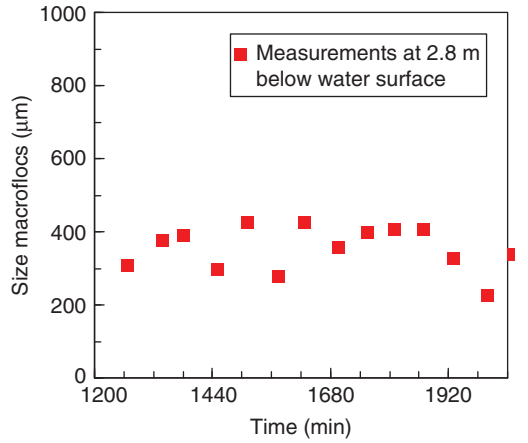

Figure 94 Measured variation in floc size (Van Leussen, 1994).

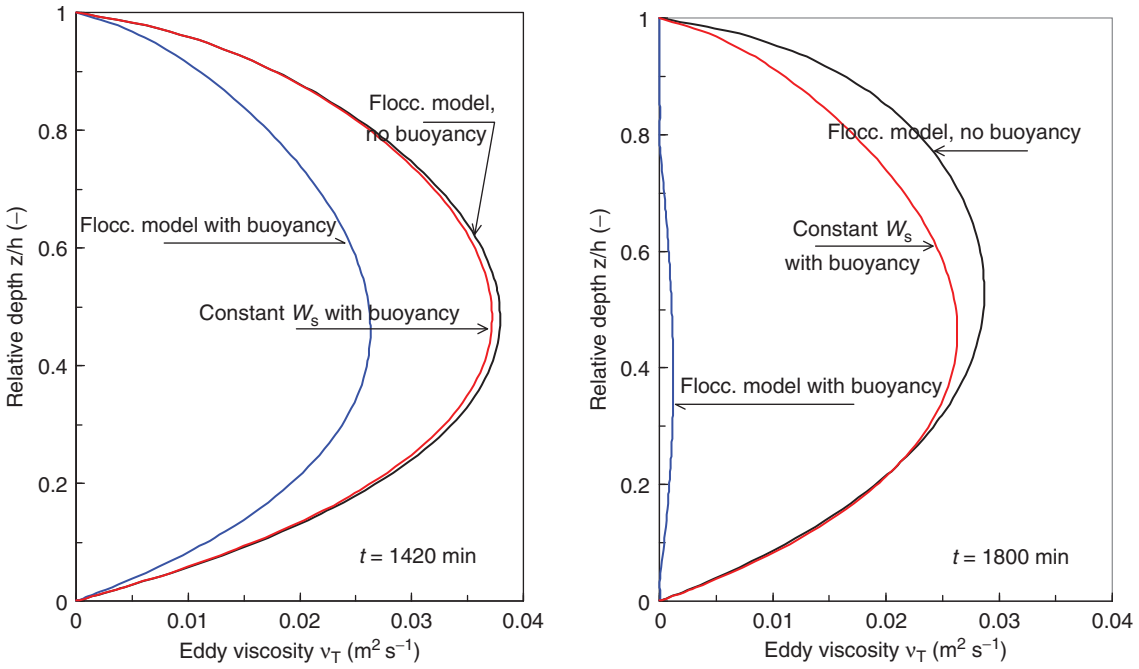

Figure 95 Computed eddy viscosity profiles during flood (left panel) and ebb (right panel).

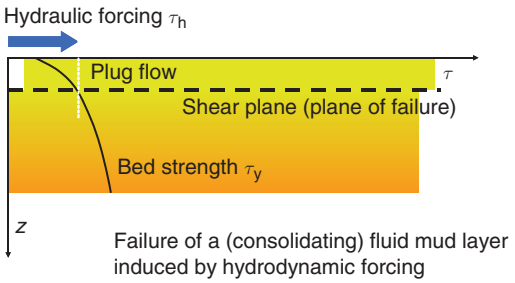

Figure 96 Sketch of drag-induced plug flow in fluid mud; above the shear plane, where $\tau_h = \tau_y$, plug flow develops.

(USA), etc.), which has been attributed to viscous dissipation of wave energy in the fluid mud layer. In this last part of this chapter, we discuss a formulation based on viscous dissipation of the waves in the fluid mud. This formulation has been implemented in SWAN (a state-of-the-art phase-integrating wave forecasting model), and we present some results.

Apart from the fluid mud's viscosity, wave energy can be lost by plastic deformations. We have reasoned that it is unlikely that fluid mud can be formed through liquefaction of a consolidated (consolidating) mud bed under natural conditions (Kranenburg et al., 2011; liquefaction though may play a role in the laboratory). Energy losses due to plastic deformations are therefore not to be expected, and even if they would, for a brief time only (after which the soil becomes a liquid).

Elastic effects do not dissipate energy, but may be important in establishing fluid motion induced by waves. The literature contains a number of viscoelastic and viscoplastic rheological models describing mud-induced wave damping and wave-induced mud transport. We discuss viscous effects only.

Figure 97 presents observations on wave damping along the north coast of South America. The aerial photograph shows wave damping along the coast of British Guyana, whereas further west (right side of the photo) foam patches indicate wave breaking. The drawing depicts the results of wave measurements in the coastal waters of Suriname, with almost full wave damping over a 10-km trajectory (redrawn from Wells (1983)).

Commonly, wave dissipation over fluid mud is modeled through a two-layer schematization, in which the lower layer reflects the fluid mud, and the upper layer a low-concentrated water column. Various schematizations have been used in literature: both layer shallow water schematization, only lower layer shallow water schematization, etc. – see Kranenburg et al. (2011) for a summary.

Here, we describe Gade's (1958) dispersion relation; this is a simple, explicit relation, which, however, contains the most important features of all other dispersion relations found in the literature. Gade assumes full shallow water conditions, and a viscous fluid mud layer. A complex wave number k is introduced: $k = k_r + ik_i$, and Gade solves the following continuity and momentum equations for the upper (subscript 1) and lower (subscript 2) layers:

$$\frac{\partial h_1}{\partial t} + h\frac{\partial u_1}{\partial x} = 0 \text{ and } \frac{\partial u_1}{\partial t} + \frac{1}{\rho_1}\frac{\partial p_1}{\partial x} = 0 \qquad [52]$$

$$\frac{\partial u_2}{\partial x} + \frac{\partial w_2}{\partial z} = 0 \text{ and } \frac{\partial u_2}{\partial t} + \frac{1}{\rho_2}\frac{\partial p_2}{\partial z} - \nu_2\frac{\partial^2 u_2}{\partial z^2} = -g \qquad [53]$$

which yields Gade's (1958) dispersion equation:

$$k = \pm\omega\left(\frac{(1+\Gamma(h_{m0}/h_{w0})) \pm \sqrt{(1+\Gamma(h_{m0}/h_{w0}))^2 - 4\gamma\Gamma(h_{m0}/h_{w0})}}{2\gamma g\Gamma h_{m0}}\right)^{1/2} \qquad [54]$$

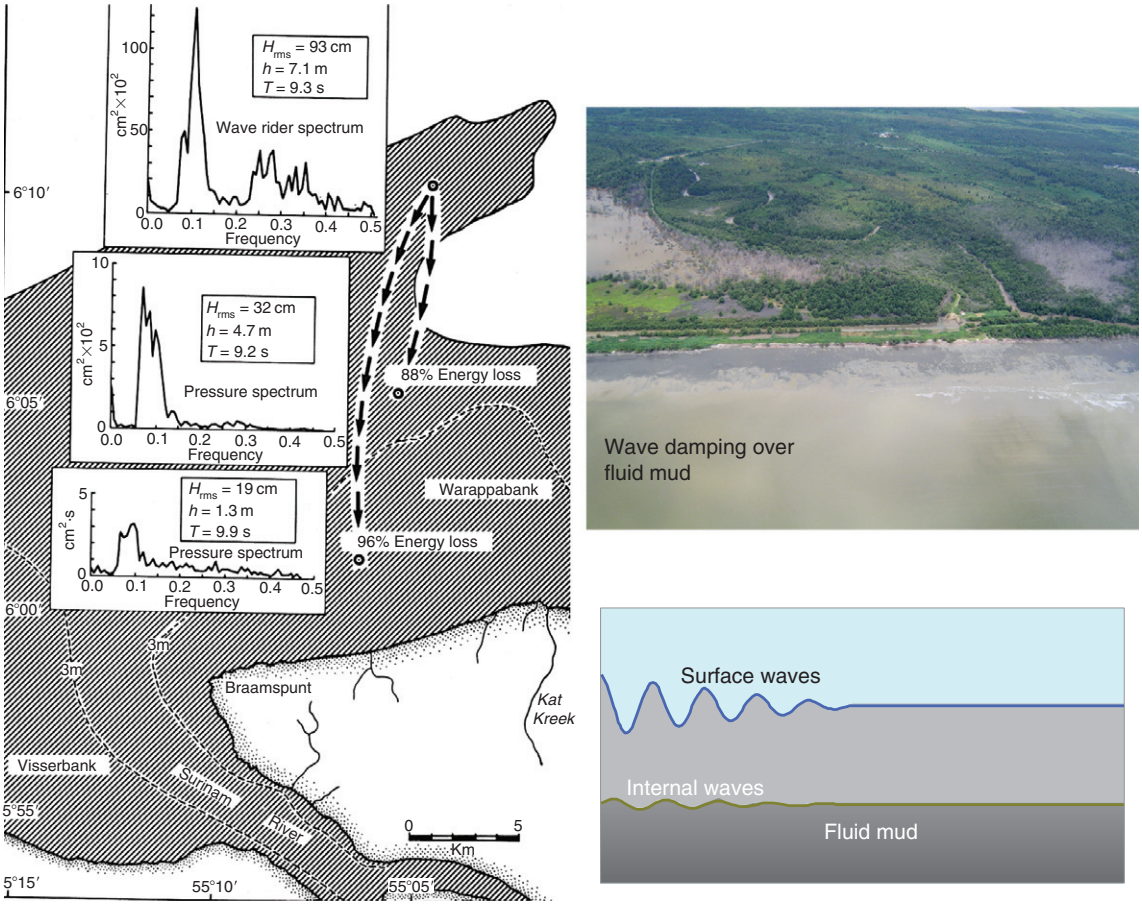

Figure 97 (Left panel) Observations of wave damping off Suriname coast; (right-upper panel) photograph of Guyana coastal zone with wave damping to the left; and (right lower panel) cartoon of wave damping over fluid mud layer, the generation of internal waves and their subsequent damping. (Left panel) (after Wells, 1983)

assuming a harmonic solution, and defining

$$\Gamma = 1 - \frac{\tan h(mh_{m0})}{mh_{m0}} \text{ and } m = (1-i)\sqrt{\frac{\omega}{2\nu_m}} \qquad [55]$$

One feature of the dispersion relation [54] is that its solution yields multiple branches in parameter space, which may be a source of misinterpretation of the damping behavior of fluid mud layers.

Further to Gade's model, a new dispersion relation was derived, accounting for a nonhydrostatic, nonviscous upper layer and a hydrostatic, viscous lower fluid mud layer, in conjunction with a dissipation term. For more details, the reader is referred to Kranenburg et al. (2011). For shallow water conditions, these new relations collapse on the Gade's solution. This dispersion relation and subsequent dissipation term have been implemented in the state-of-the-art wave-forecasting model SWAN. This wave–mud model was calibrated against wave dissipation data from laboratory experiments carried out by De Wit and Kranenburg (1996), for example, **Figure 98**.

Next, we study the wave evolution along a cross section perpendicular to the coast, over a sloping bed. Two-dimensional effects, such as refraction and directional spreading, do not play a role now. However, because of the bed slope, shoaling does.

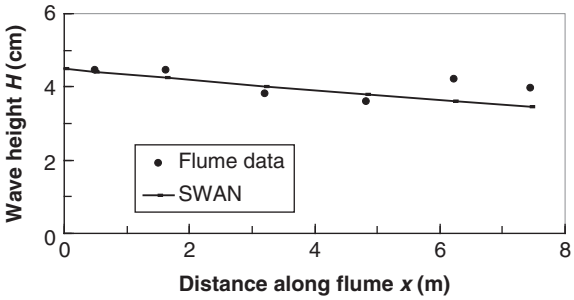

Figure 98 Comparison of computed wave damping with laboratory observations by De Wit and Kranenburg (1996).

This configuration is based on the work of Elgar and Raubenheimer (2008) and their measurements on Louisiana coast. As no values for the mud viscosity were given, we carried out a sensitivity analysis, varying the mud viscosity from 0.002 to 0.2 $m^2 s^{-1}$. The results are shown in **Figure 99**. The upper panel presents the computed evolution in significant wave height along the transect, comparing with a no-mud case. We predict wave damping for all viscosities, but maximal damping for viscosities with intermediate values, that is, 0.02 and 0.05 $m^2 s^{-1}$. The line

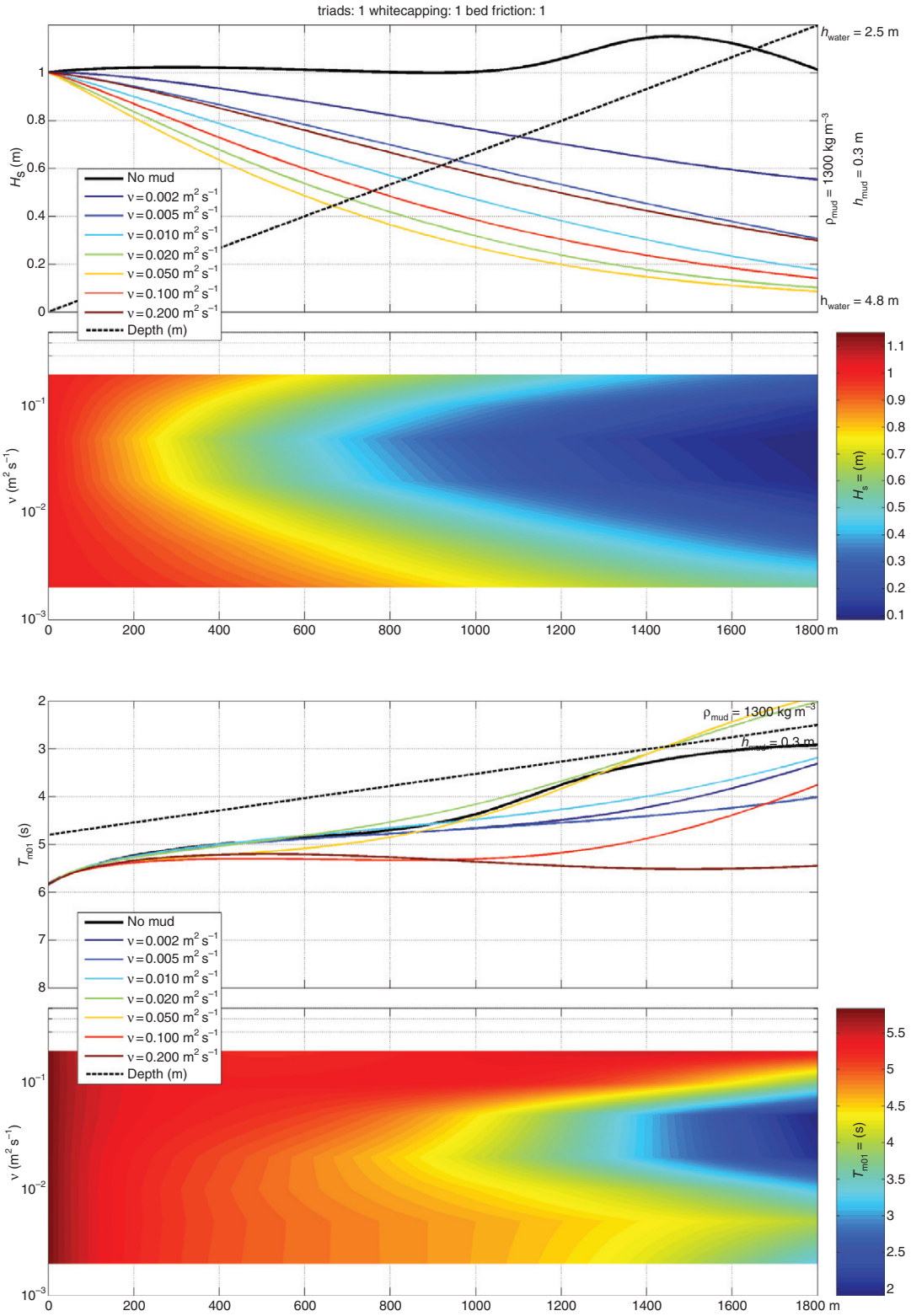

Figure 99 Wave damping over a sloping seabed; configuration after Elgar and Raubenheimer (2008); we show damping of significant wave height and changes in peak period.

plot in this upper panel is represented in 2D form in the second panel, showing the (pronounced) bimodal response in significant wave height discussed above. The peak wave period shows an even more erratic behavior (**Figure 99**, third panel), which can be explained from the trimodal response of the peak period with viscosity (lower panel). For further analysis of this case, the reader is referred to Kranenburg et al. (2011).

Note that the maximum wave damping predicted yields a 90% wave damping over about 1800 m, similar to the damping observed by Wells (1983), for example, **Figure 97**. Finally, it is interesting to realize that for the densities and viscosities commonly met in nature, maximum viscous damping of incoming waves is expected to occur when the thickness of the fluid mud layers measures a few decimeters.

References

Allersma, E., 1988. Morphological studies for the Rhine–Meuse estuary – morphological modelling part IV: composition and density of sediment. Delft Hydraulics, Report Z71-03 (in Dutch).

Amos, C.L., Daborn, G.R., Christian, H.A., Atkinson, A., Robertson, A., 1992. *In situ* erosion measurements on fine-grained sediments from the Bay of Fundy. Marine Geology 108, 175–196.

Ariathurai, C.R., Arulanandan, K., 1978. Erosion rates of cohesive soils. ASCE, Journal of the Hydraulics Division 104 (2), 279–282.

Bagnold, R.A., 1966. An approach to the sediment transport problem from general physics. Physiographic and hydraulic studies of rivers. Geological Survey Professional Paper 422-I. US Government Printing Office, Washington, DC.

Been, K., Sills, G.C., 1981. Self-weight consolidation of soft soils: an experimental and theoretical study. Géotechnique 31 (4), 519–535.

Benson, T., French, J.R., 2007. InSiPID: a new low-cost instrument for *in situ* particle size measurements in estuarine and coastal waters. Journal of Sea Research 58 (3), 167–188.

Bruens, A.W., Winterwerp, J.C., Kranenburg, C., 2011. Physical and numerical modeling of the entrainment by a high-concentrated mud suspension. ASCE, Journal of Hydraulic Engineering (submitted).

Chassagne, C., Mietta, F., Winterwerp, J.C., 2009. Electrokinetic study of kaolinite suspensions. Journal of Colloid and Interface Science 336 (1), 352–359.

Cellino, M., Graf, W.H., 1999. Sediment-laden flow in open channels under non-capacity and capacity conditions. ASCE, Journal of Hydraulic Engineering 125 (5), 456–462.

Coussot, P., 1997. Mudflow Rheology and Dynamics. IAHR Monograph Series. Balkema, Rotterdam.

De Wit, P.J., Kranenburg, C., 1996. On the effects of a liquefied mud bed on wave and flow characteristics. Journal of Hydraulic Research 34 (1), 3–18.

Dankers, P.J.T., Winterwerp, J.C., 2007. Hindered settling of mud flocs: theory and validation. Continental Shelf Research 27, 1893–1907.

Droppo, I.G., Leppard, G.G., Liss, S.N., Milligan, T.G., 2005. Flocculation in Natural and Engineered Environmental Systems. CRC Press, Boca Raton, FL.

Dyer, K.R., 1989. Sediment processes in estuaries: future research requirements. Journal of Geophysical Research 94 (C10), 14327–14339.

Einstein, H.A., 1950. The bed-load function of sediment transportation in open channel flows. Technical Bulletin No. 1026. US Department of Agriculture, Soil Conservation Service, Washington, DC.

Elgar, S., Raubenheimer, B., 2008. Wave dissipation by muddy seafloors. Journal of Geophysical Research 35 (L07611), 1–5.

Fenchel, T.M., Riedl, R.J., 1970. The sulphide system: a new biogenic community underneath the oxidised layer of marine sand bottoms. Marine Biology 7, 255–268.

Flemming, B.W., 2000. A revised textural classification of gravel-free muddy sediments on the basis of ternary diagrams. Continental Shelf Research 20, 1125–1137.

Gade, H.G., 1958. Effects of a non-rigid, impermeable bottom on plane surface waves in shallow water. Journal of Marine Research 16 (2), 61–82.

Gibson, R.E., England, G.L., Hussey, M.J.L., 1967. The theory of one-dimensional consolidation of saturated clays. Géotechnique 17, 261–273.

Grant, W.D., Madsen, O.S., 1979. Combined wave and current interaction with a rough bottom. Journal of Geophysical Research 84 (C4), 1797–1808.

Head, K.H., 1986, Manual of Soil Laboratory Testing. Pentech, London, vols. 1, 2 and 3.

Hofland, B., Battjes, J.A., 2006. Probability density function of instantaneous drag forces and shear stresses on a bed. Journal of Hydraulic Engineering 132 (11), 1169–1175.

Jacobs, W., 2011. Surface Erosion of Mixed Sediments. Ph.D. Thesis, Delft University of Technology.

Kaihatu, J.M., Sheremet, A., Holland, K.T., 2007. A model for the propagation of nonlinear surface waves over viscous muds. Coastal Engineering 54, 752–764.

Kranenburg, C., 1992. Hindered settling and consolidation of mud – analytical results. Delft University of Technology, Department of Civil Engineering, Hydromechanics Section, Report 11-92.

Kranenburg, C., 1994. An entrainment model for fluid mud, communications on hydraulic and geotechnical engineering. Faculty of Civil Engineering, Delft University of Technology, Report 94-10.

Kranenburg, W.M., Winterwerp, J.C., de Boer, G.J., Cornelisse J.M., Zijlema, M., 2011. SWAN-mud, an engineering model for mud-induced wave-damping. ASCE, Journal of Hydraulic Engineering (in press).

Krone, R.B., 1962. Flume studies of the transport of sediment in estuarial shoaling processes. Final Report Hydraulic Engineering Laboratory and Sanitary Engineering Research Laboratory, University of California, Berkeley, USA.

Krone, R.B., 1993. Sedimentation revisited. In: Mehta, A.J. (Ed.), Nearshore and Estuarine Cohesive Sediment Transport. Coastal and Estuarine Studies. American Geophysical Union, Washington, DC, pp. 108–125.

Kynch, G.J., 1952. A theory of sedimentation. Transactions of the Faraday Society 58, 166–176.

Lambe, T.W., Whitman, R.V., 1979. Soil Mechanics, SI Version. Wiley, New York, NY.

Le Hir, P., 1997. Fluid and sediment "integrated" modeling application to fluid mud flows in estuaries. In: Burt, N., Parker, R., Watts, J. (Eds.), Cohesive Sediments. Wiley, Chichester, pp. 417–428.

Le Hir, P., Monbet, Y., Orvain, F., 2007. Sediment erodability in sediment transport modelling: can we account for biota effects? Continental Shelf Research 27, 1116–1142.

Levich, V.G., 1962. Physicochemical Hydrodynamics. Prentice Hall, Englewood Cliffs, NJ.

Maggi, F., Mietta F., Winterwerp, J.C., 2007. Effect of variable fractal dimension on the floc size distribution of suspended cohesive sediment. Journal of Hydrology 343, 43–55.

Manning, A.J., Dyer, K.R., 2002. The use of optics for the *in-situ* determination of flocculated mud characteristics. Journal of Optics A: Pure and Applied Optics, Institute of Physics Publishing 4, S71–S81.

Manning, A.J., Dyer, K.R., Lafite, R., Mikes, D., 2004. Flocculation measured by video based instruments in the Gironde Estuary during the European Commission SWAMIEE project. Journal of Coastal Research 41 (Special Issue SI), 58–69.

McAnally, W.H., Friedrichs, C., Hamilton, D., Hayter, E., Shrestha, P., Rodriguez, H., Sheremet, A., Teeter, A., 2007a. Management of fluid mud in estuaries, bays, and lakes. I: present state of understanding on character and behavior. Journal of Hydraulic Engineering 133 (1), 9–22.

McAnally, W.H., Teeter, A., Schoellhamer, D., Friedrichs, C., Hamilton, D., Hayter, E., Shrestha, P., Rodriguez, H., Sheremet, A., Kirby, R., 2007b. Management of fluid mud in estuaries, bays, and lakes. II: measurement, modeling, and management. Journal of Hydraulic Engineering 133 (1), 23–38.

McCave, I.N., 1984. Size spectra and aggregation of suspended particles in the deep ocean. Deep Sea Research 31 (4), 329–352.

Merckelbach, L.M., 2000. Consolidation and Strength Evolution of Soft Mud Layers. Ph.D. Thesis, Delft University of Technology; also: Delft University of Technology, Faculty of Civil Engineering and Geosciences, Communications on Hydraulic and Geotechnical Engineering, Report 00-2, ISSN 0169-6548.

Mietta, F., Chassagne, C., Winterwerp, J.C., 2009. Shear-induced flocculation of a suspension of kaolinite as function of pH and salt concentration. Journal of Colloid and Interface Science 336 (1), 134–141.

Mitchell, J.K., 1976. Fundamentals of Soil Behaviour. Wiley, New York, NY.

Obi, S., Inoue, K., Furukawa, T., Masuda, S., 1996. Experimental study on the statistics of wall shear stress in turbulent channel flows. International Journal of Heat and Fluid Flow 17 (3), 187–192.

Partheniades, E., 1986. A fundamental framework for cohesive sediment dynamics. In: Mehta, A.J. (Ed.), Estuarine Cohesive Sediment Dynamics. Lecture Notes on Coastal and Estuarine Studies, 14. Springer, Berlin, ch. XII, pp. 219–250.

Partheniades, E., 2010. Cohesive Sediments in Open Channels. Elsevier, Butterworth-Heinemann.

Paterson, D.M., 1997. Biological mediation of sediment erodibility: ecology and physical dynamics. In: Burt, N., Parker, R., Watts, J. (Eds.), Cohesive Sediments. Wiley, Chichester, pp. 215–229.

Raudkivi, A.J., 1976. Loose Boundary Hydraulics, Second ed. Pergamon, Oxford.

Raudkivi, A.J., 1990. Loose Boundary Hydraulics, Third ed. Pergamon Press, Oxford.

Richardson, J.F., Zaki, W.N., 1954. Sedimentation and fluidization, part I. Transactions of the Institution of Chemical Engineers 32, 35–53.

Roscoe, K.H., Schofield, A.N., 1963. Mechanics behaviour of a 'wet' clay. Proceedings of the European Conference on Soil Mechanics and Foundation Engineering. Deutsche Gesellshaft fur Erd- und Grundbau e. V., Wiesbaden, Germany, vol. 1, pp. 47–54.

Sanford, L.P., Halka, J.P., 1993. Assessing the paradigm of mutually exclusive erosion and deposition of mud, with examples from upper Chesapeake Bay. Marine Geology 114, 37–57.

Sanford, L.P., Maa, J.P.-Y., 2001. A unified erosion formulation for fine sediments. Marine Geology 179, 9–23.

Smerdon, E.T., Beasley, R.P., 1959. The tractive force applied to stability of open channels in cohesive soils. University of Missouri, Research Bulletin 715.

Smoluchowski, M., 1917. Versuch einer Mathematischen Theorie der Koagulations-kinetik Kolloid Lösungen. Zeitschrift für Physikalische Chemie, Leipzig 92, 129–168 (in German).

Soulsby, R.L., Hamm, L., Klopman, G., Myrhaug, D., Simons R.R., Thomas, G.P., 1993. Wave–current interaction within and outside the bottom boundary layer. Coastal Engineering 21, 41–69.

Soulsby, R.L., Wainwright, B.L.S.A., 1987. A criterion for the effect of suspended sediment on near-bottom velocity profiles. IAHR, Journal of Hydraulic Research 25 (3), 341–356.

Stolzenbach, K.D., Elimelich, M., 1994. The effect of density on collisions between sinking particles: implications for particle aggregation in the ocean. Journal of Deep Sea Research I 41 (3), 469–483.

Suijlen, J.M., Duin, R.N.M., 2001. Variability of near-surface total suspended matter concentrations in the Dutch coastal zone of the North Sea. Climatological study on the suspended matter concentration in the North Sea. Report RIKZ/OS/2001.150X.

Terzaghi, K., 1943, Theoretical Soil Mechanics. Wiley, New York, NY.

Toorman, E.A., Berlamont, J.E., 1991. A hindered settling model for the prediction of settling and consolidation of cohesive sediment. Geo-Marine Letter 11, 179–183.

Turner, J.S., 1973. Buoyancy Effects in Fluids. Cambridge University Press, Cambridge.

Van Kessel, T., Winterwerp, J.C., van Proojen, B., et al. 2010. Modelling the seasonal dynamics of SPM with a simple algorithm for the buffering of fines in a sandy seabed. Continental Shelf Research doi:10.1016/j.csr.2010.04.008.

Van Ledden, M., van Kesteren, W.G.M., Winterwerp, J.C., 2004. A classification for erosion behaviour of sand–mud mixtures. Continental Shelf Research 24, 1–11.

Van Leussen, W., 1994. Estuarine Macroflocs and Their Role in Fine-Grained Sediment Transport. Ph.D. Thesis, University of Utrecht, The Netherlands.

Van Prooijen, B.C., Winterwerp, J.C., 2010. A stochastic formulation for erosion of cohesive sediments. Journal of Geophysical Research 115, C01005. doi:10.1029/2008JC005189.

Van Rijn, L.C., 1993. Principles of Sediment Transport in Rivers, Estuaries and Coastal Seas. AQUA Publications, Amsterdam.

Verwey, E.J.W., Overbeek, J.T.G., 1948. Theory of the Stability of Lyophobic Colloids. Elsevier, Amsterdam.

Vicsek, T., 1992. Fractal Growth Phenomena, World Scientific, Singapore.

Vinzon, S.B., Mehta, A.J., 2003. Lutoclines in high concentration estuaries: some observations at the mouth of the Amazon. Journal of Coastal Research 19 (2), 243–253.

Weaver, C.E., 1989. Clays, Muds and Shales. Developments in Sedimentology. Elsevier, Amsterdam, vol. 44.

Wells, J.T., 1983. Dynamics of coastal fluid muds in low-, moderate, and high-tide-range environments. Canadian Journal of Fisheries and Aquatic Science 40 (supplement 1), 130–142.

Winterwerp, J.C., 1998. A simple model for turbulence induced flocculation of cohesive sediment. IAHR, Journal of Hydraulic Engineering 36 (3), 309–326.

Winterwerp, J.C., 2001. Stratification of mud suspensions by buoyancy and flocculation effects. Journal of Geophysical Research 106 (10), 22 559–22 574.

Winterwerp, J.C., 2002. On the flocculation and settling velocity of estuarine mud. Continental Shelf Research 22, 1339–1360.

Winterwerp, J.C., 2007. On the deposition flux of cohesive sediment. In: Maa, J., Sanford L., Shoelhamer, D. (Eds.), Proceedings in Marine Science, Vol. 8, Estuarine and Fine Sediment Dynamics. Proceedings of the 8th International Conference on Nearshore and Estuarine Cohesive Sediment Transport Processes, INTERCOH-2003. Gloucester Point, VA, USA. Elsevier, Amsterdam, pp. 209–226.

Winterwerp, J.C., de Boer, G.J., Greeuw, G., van Maren, D.S., 2011. Mud-induced wave damping and wave-induced liquefaction. Coastal Engineering (submitted).

Winterwerp, J.C., Lely, M., He, Q., 2009. Sediment-induced buoyancy destruction and drag reduction in estuaries. Ocean Dynamics 59 (5), 781–791.

Winterwerp, J.C., Manning, A.J., Martens, C., de Mulder T., Vanlede, J., 2006. A heuristic formula for turbulence-induced flocculation of cohesive sediment. Estuarine, Coastal and Shelf Science 68, 195–207.

Winterwerp, J.C., van Kesteren, W.G.M., 2004. Introduction to the Physics of Cohesive Sediments in the Marine Environment. Developments in Sedimentology. Elsevier, Amsterdam, vol. 56.

Xu, J., 2003. Sedimentation rates in the Lower Yellow River over the past 2300 years as influenced by human activities and climate change. Hydrological Processes 17, 3359–3371.